

The Application of Doppler LIDAR Technology for Rail Inspection and Track Geometry Assessment

Masood Taheri Andani

Dissertation submitted to the Faculty of the Virginia Polytechnic Institute and State University
in partial fulfillment of the requirements for the degree of

Doctor of Philosophy
in
Mechanical Engineering

Mehdi Ahmadian, Chair

Tomonari Furukawa

Dong S. Ha

Steve C. Southward

Alfred L. Wicks

April 5, 2016

Blacksburg, Virginia

Keywords: Doppler LIDAR, Track Geometry, Railway Health Monitoring, Rail Deterioration

Copyright© 2015, Masood Taheri Andani

The Application of Doppler LIDAR Technology for Rail Inspection and Track Geometry Assessment

Masood Taheri Andani

Abstract

The ability of a Doppler LIDAR (Light Detection and Ranging) system to measure the speed of a moving rail vehicle in a non-contacting manner is extended to capture the lateral and vertical irregularities of the track itself and to evaluate the rail track quality. Using two pairs of lenses to capture speed signals from both rails individually, the track speed, curvature, and lateral and vertical geometry variations on each side are determined. LIDAR lenses are installed with a slight forward angle to generate velocity signals that contain two components: 1) the left and right track speeds, and 2) any lateral and/or vertical speed caused by track motion and/or spatial irregularities. The LIDAR system collects and outputs the track information in time domain. Separating each speed component (forward, vertical, and lateral) is possible due to the inherent separation of each phenomenon with respect to its spatial/temporal frequencies and related bandwidths. For the measurements to be beneficial in practice, the LIDAR data must be spatially located along the track. A data-mapping algorithm is then simultaneously developed to spatially match the LIDAR track geometry measurements with reference spatial data, accurately locating the measurements along the track and eliminating the need for a Global Positioning System (GPS).

A laboratory-grade LIDAR system with four Doppler channels, developed at the Railway Technologies Laboratory (RTL) of Virginia Tech, is body-mounted and tested onboard a geometry measurement railcar. The test results indicate a close match between the LIDAR measurements and those made with existing sensors onboard the railcar. The field-testing conducted during this study indicates that LIDAR sensors could provide a reliable, non-contact track-monitoring instrument for field use, in various weather and track conditions, potentially in a semi-autonomous or autonomous manner.

A length-based track quality index (TQI) is established to quantify the track geometry condition based on the geometry data collected by the LIDAR sensors. A phenomenological rail deterioration model is developed to predict the future degradation of geometry quality over the short track segments. The introduced LIDAR's TQI is considered as the condition-parameter, and an internal variable is assumed to govern the rail geometry degradation through a deterioration rule. The method includes the historical data, current track conditions collected by the LIDAR system, and traffic data to calculate the track deterioration condition and identify the geometry defects.

In addition to rail geometry inspection, a LIDAR system can potentially be used to monitor the rail surface structure and integrity. This is possible due to the fact that the Doppler shift imposed on the laser radiation reflected from a moving surface has the Doppler bandwidth broadened in proportion to the height and width of the surface features. Two LIDAR-based rail surface measures are introduced based on LIDAR measurements to identify different rail surface conditions and materials.

Acknowledgments

I owe my profound gratitude to my advisor, Professor Mehdi Ahmadian, for his continuous guidance, advice, and support during my research at the Center for Vehicle Systems and Safety (CVeSS). I am extremely grateful to him for giving me this invaluable opportunity to be a part of CVeSS and learn from him. I would also like to thank Dr. Steve Southward, Dr. Dong Ha, Dr. Tomonari Furukawa, and Dr. Alfred Wicks for serving on my doctoral advisory committee.

My sincere thanks goes to Mr. Carvel Holton for his precious guidance and generous support throughout my research endeavors. I would also like to thank my fellow graduate research assistant, Dr. Josh Munoz, for his assistance throughout the LIDAR project. I am also thankful to Dr. Andrew Peterson, CVeSS research scientist and lab manager, for his friendship and help.

I acknowledge and appreciate the financial and technical support provided by the Federal Railroad Administration (FRA), Association of American Railroads (AAR), and Norfolk Southern's Research and Tests Department. In particular, I am grateful to Mr. Brad Kerchof and Mr. Scott Hailey for their tremendous support during rail geometry inspection car testing.

I thank my fellow labmates at CVeSS for all the nights and days we were working together before deadlines, and for all the fun we have had in the last three years. Also I thank my wonderful friends in Blacksburg.

Last, but not least, I would like to thank my lovely family: my parents, brother, sister, and sister-in-law for supporting me.

Contents

Abstract.....	ii
Acknowledgments.....	iii
Contents	iv
List of Figures	vii
List of Tables	xiv
Chapter 1: Introduction	1
1.1 Motivation.....	1
1.2 Objectives	2
1.3 Approach.....	3
1.4 Contributions.....	5
1.5 Outline.....	6
Chapter 2 : Literature Review and Background	7
2.1 Track Geometry Irregularities.....	7
2.1.1 Alignment	8
2.1.2 Gage	8
2.1.3 Profile.....	9
2.1.4 Cross level.....	10
2.2 Track Irregularity Measurement and Evaluation	10
2.3 Track Class.....	12
2.4 Track-induced Vibration.....	12
2.5 Track Quality Index	12
2.6 Track Geometry Deterioration	13
2.7 Rail Surface Defects	13
2.7.1 Rail surface monitoring.....	14
2.8 Rail Lubrication and Friction Modification	15
2.8.1 Rail Lubrication Monitoring	15
2.9 Track Speed and Curvature Detection	16
2.10 Doppler LIDAR Technology	18
2.10.1 Doppler laser measurements	20

2.10.2 Virginia Tech’s LIDAR system	23
Chapter 3: Rail Geometry Inspection Car Testing	29
3.1 System Setup.....	29
3.2 Ground-truth Calibration	32
3.3 Test Routes.....	36
3.4 LIDAR Lens Orientation and Coordinate System	36
Chapter 4: Lateral Track Geometry Measurements	40
4.1 LIDAR Sensing and Processing.....	41
4.1.1 Configuration of LIDAR lenses.....	42
4.1.2 LIDAR data processing technique	44
4.2 Experimental Results and Evaluation	46
4.2.1 Time domain analysis	47
4.2.2 Spatial domain analysis.....	49
4.3 Statistical Probability Distributions: Evaluation of Alignment and Gage	56
4.4 Universality of Track Geometry Measurements.....	61
Chapter 5: Vertical Track Geometry Monitoring.....	66
5.1 LIDAR Sensing and Processing.....	66
5.1.1 Track geometry estimation	68
5.2 Experimental Results and Evaluation	71
5.3 Probability Analysis.....	75
Chapter 6: Bi-directional Speed Measurement Using LIDAR	80
6.1 Bi-directional Speed Measurement.....	80
6.2 Experimental Set-up.....	82
6.2.1 Instrumental equipment	82
6.2.2 Data acquisition and processing set-up.....	84
6.3 Results and Discussion	85
6.3.1 Vibration detection.....	85
6.3.2 Oscillation shape characterization	86
6.3.3 Frequency spectrum characterization	88
6.3.4 Intricate mechanical vibration series	89
6.3.5 Velocity linearity and accuracy assessment.....	91

6.3.6 Surface figure effect.....	92
6.3.7 LIDAR velocity self-normalizing and infrastructure detection.....	93
Chapter 7: Track Quality Evaluation and Prediction using LIDAR technology	96
7.1 Track Segmentation	96
7.2 LIDAR's Track Quality Index	98
7.3 Degradation Modeling	100
7.4 Results and Discussion	103
7.4.1 LIDAR data correlation	103
7.4.2 TQI results	104
7.4.3 Numerical example of model application	108
Chapter 8: Application of LIDAR Technology for Rail Surface and Structural Integrity	
Monitoring	112
8.1 LIDAR-based Rail Surface Feature Aspect Ratio	112
8.2 LIDAR Intensity Ratio.....	113
8.3 Preliminary Testing and Technology Demonstration.....	115
8.4 Data Processing and Results.....	117
Chapter 9: Development of a Bipolar LIDAR System for Track Curvature Measurements	130
9.1 Single Channel Bipolar LIDAR System.....	131
9.1.1 Description of the concept	131
9.1.2 Prototype development and testing.....	134
Chapter 10: Summary and Recommendations	138
10.1 Summary.....	138
10.2 Recommendations for Future Studies.....	139
References.....	142
Appendix A.: Specifications of the Inertial Measurement Unit (IMU) used on the research car	147
Appendix B: H/D Ratio for Rail Surface Assessment	148

List of Figures

Figure 2-1. Track alignment deviation.....	8
Figure 2-2. Track gage variation.....	9
Figure 2-3. Track profile variation.....	9
Figure 2-4. Track elevation variation.....	10
Figure 2-5. Measurement Configuration I; when a fixed laser strikes perpendicular to a moving target, the measured velocity is proportional to the difference between the transmitted wavelength and the returned wavelength.....	21
Figure 2-6. Measurement Configuration II; when a moving laser strikes perpendicular to a fixed target, the measured velocity is proportional to the difference between the transmitted wavelength and the returned wavelength.....	21
Figure 2-7. Measurement Configuration III: when a fixed laser strikes oblique to a moving target, the velocity in direction of the incidence (V_x) is proportional to the difference between the transmitted wavelength and the returned wavelength. Measurement at oblique incidence is possible only if the target surface has diffuse reflection.....	22
Figure 2-8. Measurement Configuration IV: when a moving laser strikes oblique to a fixed target, the measured velocity in direction of the incidence (V_x) is proportional to the difference between the transmitted wavelength and the returned wavelength. Measurement at oblique incidence is possible only if the target surface has diffuse reflection.....	23
Figure 2-9. Simple schematic of LIDAR lens orientation with respect to the rail. The lenses serve as both light emitters and receivers.	24
Figure 2-10. Block diagram of Virginia Tech’s multi-functional LIDAR system for track speed and rail geometry measurements	26
Figure 3-1. LIDAR body-mounted setup; (a) NS38 research car, (b) LIDAR mounting frame. LIDAR sensors are installed in blue housings to protect the lenses from dust and debris.	30
Figure 3-2. Close-up view of lens arrangement. The top lens is installed in a blue housing and captures rail speed. The lower lens captures rail alignment variation from the opposite rail.....	31
Figure 3-3. LIDAR computer electronics are located in the cab of the research car.....	31
Figure 3-4. 4 feet long fiducial boards were used for LIDAR distance calibration. Boards are painted in black at two ends and white at the middle to provide a good fiducial signal.	32
Figure 3-5. Fiducial boards were drilled to the ties.	32
Figure 3-6. Marked sections were also measured by a measuring wheel.....	33
Figure 3-7. Fiduciary sensor was installed inside a cylindrical enclosure and mounted under the body.....	33
Figure 3-8. Speed profile of the calibration run as recorded by the encoder and LIDAR system. There is high correlation between the speed signals, however, the wheel encoder shows significantly higher instantaneous variation across the entire test run due to mechanical effects.	35
Figure 3-9. Calculated distance traveled by the encoder and LIDAR system. There is high correlation in distance measurement, as confirmed by the data provided in Table 3-2.....	35
Figure 3-10. Using the information gathered from the calibration run, the appropriate gain in the LIDAR data is applied to match real conditions. The plot above shows the speed result after ground-truth calibration.	36

Figure 3-11. The laser coordinate system (X_L - Y_L - Z_L) is oriented with respect to the rail coordinate system (X_R - Y_R - Z_R). the lens coordinate is selected so that the laser beam strikes the rail along the Z_L axis.	37
Figure 3-12. LIDAR system coordinate system transformation: (a) rotation of the laser coordinate system about the rail lateral axis to capture forward track speed, (b) rotation of the laser about the rail longitudinal axis to accommodate lens installation and/or capturing lateral track speed.	38
Figure 4-1. Lateral LIDAR optics used for lateral geometry measurements; (a) beams target the gage face of the rails, (b) left and right track speeds are measured, (c) rates of left and right lateral geometry are observed by the lateral lenses.	42
Figure 4-2. The ideal LIDAR lens orientation for lateral track geometry measurements is achieved when the laser strikes perpendicular to the gage face with no elevation. With this orientation, the rail forward velocity is not captured by the LIDAR sensor. This orientation was not possible during filed testing due to installation limitations	43
Figure 4-3. The proposed LIDAR lens orientation for lateral track geometry measurements onboard the metrology car; (a) 3-D isometric view of the embodiment for the right rail, (b) top view of the embodiment for the right rail, (c) front view of the LIDAR embodiment for the right rail.	44
Figure 4-4. Post-processing algorithm implemented to derive train speed, track curvature, and lateral track irregularities using LIDAR measurements.	47
Figure 4-5. LIDAR left and right forward bias speeds in time domain.	48
Figure 4-6. LIDAR centerline speed in comparison with encoder reading.	49
Figure 4-7. Computed left and right lateral velocities for 20 seconds of the travel.	50
Figure 4-8. Left rail alignment profile measured by the LIDAR system and IMU, showing good correlation on a larger scale. The boxed sections are examined more closely in the following figures	51
Figure 4-9. A closer look at the left rail alignment deviations before, along, and after the right-hand curve boxed in Figure 4-8. The variation profiles do not show high correlation, however, the magnitude of the variations are similar, signifying a detection of variation by the LIDAR system.	52
Figure 4-10. Left rail alignment deviations along the boxed left-hand curve in Figure 4-8. Similar to the profile along the right-hand curve, the magnitude of alignment deviations matches closely with that of the IMU's detection of alignment.	52
Figure 4-11. Right rail alignment profile measured by the LIDAR system and IMU, showing good correlation on a larger scale.	53
Figure 4-12. A close-up view of the right rail alignment along the right-hand curve boxed Figure 4-11. The same observations made for the left rail apply to the right rail. Some correlation is found between the LIDAR and IMU signals, however, the magnitude of alignment variation is the primary similarity between the two.	53
Figure 4-13. Right rail alignment variation profile along the left-hand curve boxed in Figure 4-11.	54
Figure 4-14. LIDAR gage calculation compared with the gage sensor onboard the geometry car without curvature subtraction and appropriate filtering.	55
Figure 4-15. Gage variation measured by the LIDAR system and gage sensor onboard the geometry car in the boxed right hand curve of Figure 4-14. The primary correlation lies in the magnitude of gage change detected along both the curved and tangent sections.	55

Figure 4-16. Gage variation detected along the boxed left-hand curve of Figure 4-14.....	56
Figure 4-17. Probability distributions of LIDAR and IMU left alignment measurements; (a) left alignment probability density function (PDF), (b) left alignment cumulative density function (CDF).....	58
Figure 4-18. Probability distributions of LIDAR and IMU right alignment measurements; (a) right alignment probability density function (PDF), (b) right alignment cumulative density function (CDF).....	59
Figure 4-19. Probability distributions of LIDAR and onboard gage sensor measurements; (a) local gage variation probability density function (PDF), (b) local gage variation cumulative density function (CDF) .	60
Figure 4-20. 95th percentile amplitude distribution for gage and alignment measurements.....	61
Figure 4-21. Left rail alignment comparison between LIDAR and IMU measurements in the spatial domain.	62
Figure 4-22. Variation of left rail alignment from the boxed section in Figure 4-21.....	63
Figure 4-23. Right rail alignment comparison between LIDAR and IMU measurements in the spatial domain.	63
Figure 4-24. Variation of right rail alignment from the boxed section in Figure 4-23.....	64
Figure 4-25. Overall gage variation comparison of LIDAR and onboard gage sensor measurements in the spatial domain.	65
Figure 4-26. Gage variation in the boxed section in Figure 4-25.	65
Figure 5-1. The ideal LIDAR lens orientation for vertical track geometry measurements overlays the rail coordinate system with the laser coordinate system. With this orientation, however, the rail forward velocity is not recorded. This orientation was not possible during field testing due to installation limitations.....	67
Figure 5-2. Vertical LIDAR optics used for vertical geometry measurements; (a) beams target the gage corner of the rails, (b) left and right track speeds are measured, (c) rates of left and right vertical geometry are observed by the lateral lenses.	68
Figure 5-3. Velocity measurement of the right LIDAR sensor; 3-D isometric view of the embodiment and right rail, (b) top view of the embodiment and right rail, (c) front view of the embodiment and right rail.....	69
Figure 5-4. Calculation procedure applied to LIDAR measurements to extract vertical track irregularities.....	71
Figure 5-5. Forward left and right rail speeds determined from the bias forward angle of the lenses.....	72
Figure 5-6. The computed centerline speed from the left and right speed signals compared with the encoder signal. A good correlation exists between the two instruments' estimation of speed.	72
Figure 5-7. Comparison of LIDAR and IMU track elevation measurements in spatial domain; (a) total track elevation, (b) track elevation variation in the specified segment	74
Figure 5-8. Comparison of LIDAR and IMU right profile in spatial domain for 1 mile of the track.....	75
Figure 5-9. Comparison of LIDAR and IMU left profile in spatial domain for 1 mile of the track	75
Figure 5-10. Probability distributions of LIDAR and IMU right profile measurements; (a) right profile variation probability density function (PDF), (b) right profile variation cumulative density function (CDF).....	76

Figure 5-11. Probability distributions of LIDAR and IMU left profile measurements; (a) left profile variation probability density function (PDF), (b) left profile variation cumulative density function (CDF)..... 77

Figure 5-12. Probability distributions of LIDAR and IMU track elevation measurements; (a) track elevation variation probability density function (PDF), (b) track elevation variation cumulative density function (CDF) 78

Figure 5-13. 95th percentile amplitude distribution elevation measurements 79

Figure 6-1. LIDAR speed measurement contains information about both translational speed (x-direction) and oscillating velocity (y-direction) when the lens is oriented and laser strikes the moving target with a bias angle. 81

Figure 6-2. LIDAR-Roehrig set-up; rotary disk replicates vehicle speed and Roehrig electromagnetic actuator simulates track dynamics by vertically vibrating the disk. LIDAR beam strikes the disk face with a slight bias angle to allow for 2-D speed measurements. 83

Figure 6-3. Rotary disk is mounted on the Roehrig in two configurations: a) LIDAR beam targets the disk face. This configuration allows for a wide range of bias angles and off-set speeds. (b) LIDAR strikes the wall. This embodiment allows for larger vertical motions to be simulated while keeping the constant linear motion. 84

Figure 6-4. A National Instrument PXI computer is employed to perform FFT analysis and compute target speed from Doppler frequency shift..... 85

Figure 6-5. LIDAR speed measurements with the presence of vibration; rotary disk starts to rotate and generates the off-set speed required to detect the sinusoidal oscillation applied by the Roehrig actuator..... 86

Figure 6-6. LIDAR speed measurement for a sinusoidal displacement excitation with amplitude of $A=0.5$ in and frequency of $f=1$ Hz is compared with the Roehrig velocity reading for 1 cycle. 87

Figure 6-7. LIDAR speed measurement for a triangular displacement excitation with amplitude of $A=0.5$ in and frequency of $f=1$ Hz is compared with the Roehrig velocity reading. 87

Figure 6-8. FFT response of LIDAR velocity measurement for sinusoidal excitations with 1 in/sec maximum vertical velocity. 88

Figure 6-9. STFT (Short-time Fourier transform) of LIDAR velocity measurements for a series of large amplitude vertical vibrations. The specifications of the six simulated waveforms are listed in the table on the right..... 89

Figure 6-10. FFT response of LIDAR velocity measurement for the large amplitude vibrations depicted in Figure 6-9. 90

Figure 6-11. Displacement trajectories derived from LIDAR speed measurements are compared with four large amplitude excitation waveforms (as depicted in Figure 6-9) applied by the Roehrig actuator..... 91

Figure 6-12. Oscillatory speed measurement for a sinusoidal displacement excitation with amplitude of $A=0.1$ in and frequency of $f=5$ Hz with the purpose of correlation analysis. Correlation coefficient is 0.993..... 92

Figure 6-13. Roehrig speed recording vs. LIDAR speed measurement for the sinusoidal excitation shown in Figure 28. The slope of linear regression is expected to be 1. 92

Figure 6-14. Effect of surface figure on the LIDAR speed measurement is investigated for a sinusoidal displacement excitation with amplitude of $A=0.2$ in and frequency of $f=5$ Hz. The rotary disk is polished as it is and a stick-on 60-grit sandpaper is used to create a coarse surface figure. 93

Figure 6-15. The displacement profile simulated by the Roehrig actuator as an example of infrastructure spatial signature.....	94
Figure 6-16. Normalized LIDAR speed plots for four different driving speeds, while a displacement signature waveform (Figure 6-15) is applied to the rotary disk.	95
Figure 6-17. Peak values of the normalized speeds (Figure 6-16) as a function of off-set driving speeds. Linear regression shows that the simulated signature can be detected by a peak index of 1.1.....	95
Figure 7-1. LIDAR data aligning algorithm; LIDAR spatial data is divided into segments of signature data to be aligned with a set of reference data.	97
Figure 7-2. Schematic description of the length-based TQI measured by the LIDAR system for: (a) lateral irregularities, (b) vertical irregularities.....	98
Figure 7-3. Calculation procedure of track quality alignment indices using LIDAR system.....	99
Figure 7-4. Spatial sampling resolution as a function of forward velocity for three given sampling rates.	100
Figure 7-5. Track deterioration and restoration in terms of the Track Quality Index (TQI)	101
Figure 7-6. LIDAR spatial segments of various lengths and different number of curves.	103
Figure 7-7. Alignment of LIDAR curvature segments with IMU reference data.....	104
Figure 7-8. Left alignment measurements made by LIDAR system and IMU for 0.5 mi section of the track.....	105
Figure 7-9. Right alignment measurements made by LIDAR system and IMU for 0.5 mi section of the track.	105
Figure 7-10. Standard deviation distribution of LIDAR and IMU left alignment measurements calculated over 1000 ft segments.	106
Figure 7-11. Standard deviation distribution of LIDAR and IMU right alignment measurements calculated over 1000 ft segments.....	106
Figure 7-12. LIDAR's track quality left alignment index calculated over 1000 ft segments.....	107
Figure 7-13. LIDAR's track quality right alignment index calculated over 1000 ft segments ..	107
Figure 7-14. LIDAR's track quality left alignment index calculated over 1000 ft segments. Curved and tangent segments are decoupled.....	108
Figure 7-15. Prediction of TQI for a segment with the critical quality of $Q_{cr} = 35$ and 5 maintenance operations.....	109
Figure 7-16. Prediction of degradation fraction (d) for a segment with the critical quality of $Q_{cr} = 35$ and 5 maintenance operations.	110
Figure 7-17. Prediction of reduction in the maintenance period as a function of maintenance operation number.	110
Figure 7-18. Prediction of TQI for 3000 ft of track with 100ft long sections (critical quality, $Q_{cr} = 35$).....	111
Figure 8-1. Doppler shift spectrum determines center Doppler velocity (V_c), collected LIDAR frequency bandwidth (FWHM), and maximum laser spectral intensity (I_m).....	113
Figure 8-2. RTL rail panel is divided into two sections of 5ft for lab testing. The reflective tape separates the two sections for easier detection of the sections upon data processing.....	115
Figure 8-3. LIDAR sensors are mounted to the RTL rail trolley for rail surface feature lab testing. The cart is driven by a remotely controlled DC motor for a constant speed and consistent data collection.	115

Figure 8-4. LIDAR laser beam targets top of the rail. Section A is coated with different materials and Section B is kept dry.	116
Figure 8-5. LIDAR FWHM measurements collected over bare rail in Test 1. A moving average with a window size of 15 data points is applied to the raw FWHM data.	117
Figure 8-6. LIDAR track speed measurements during Test 1. The average speed of the cart during test was 1.5 mph ($V_r=1.5$ mph).....	118
Figure 8-7. RSF measurements for bare rail in Test 1. The average RSF ratio for the dry bare rail is 0.08.....	119
Figure 8-8. LIDAR spectral intensity measurements for bare rail in Test 1. Sections A and B are both dry. The average intensity for Sections A and B are 0.15 and 0.1, respectively.	119
Figure 8-9. LIR measurements for bare rail in Test 1. The reference intensity (RI) is calculated from the ratio of the average bare rail intensity (Figure 8-8) to the average velocity (Figure 8-6) to be $R_I=0.057$ w/ft. The reflective tape has a very large LIR value (>50).	120
Figure 8-10. A water-based ToR friction modifier is applied on Section A for Test 2.....	121
Figure 8-11. LIDAR FWHM measurements collected over the lubricated Section A and bare Section B in Test 2. A moving average with a window size of 15 data points is applied to the raw FWHM data.	121
Figure 8-12 LIDAR track speed measurements during Test 2. A moving average is applied to the raw speed data to remove the high frequency variations.	122
Figure 8-13. RSF measurements for the lubricated Section A and bare Section B in Test 2. There is a 53% variation between the average RSF ratios for these two coating conditions.....	122
Figure 8-14. LIR results for Test 2 ($R_I=0.057$ w/ft). The average LIR for Section A with friction modifier is 9.2 times greater than the average LIR for bare Section B.	123
Figure 8-15. Sawdust is applied on Section A to simulate leaf residues on the rail for Test 3. .	123
Figure 8-16. RSF measurements for Section A with sawdust coating and bare Section B in Test 3. There is a 45% variation between the average RSF ratios for these two coating conditions.	124
Figure 8-17. LIR results for Test 3 ($R_I=0.057$ w/ft). The average LIR for Section A with sawdust is 9 times greater than the average LIR for bare Section B.	124
Figure 8-18. Top of the rail in Section A is covered by 40-grit sandpaper to simulate a coarse rail surface (Test 4).	125
Figure 8-19. RSF measurements for Section A with sandpaper coating and bare Section B in Test 4. There is an 80% variation between the average RSF ratios for these two coating conditions.	125
Figure 8-20. LIR results for Test 4 ($R_I=0.057$ w/ft). The average LIR for Section A with sandpaper is 5.4 times greater than the average LIR for bare Section B.	126
Figure 8-21. RSF measurements for Section A with sandpaper coating and bare Section B in Test 5.....	126
Figure 8-22. LIR results for Test 5 ($R_I=0.057$ w/ft). The average LIR for Section A with sandpaper is 4.7 times greater than the average LIR for bare Section B.	127
Figure 8-23. Comparison of RSF ratio measurements made for different rail surface conditions over Section A.....	127
Figure 8-24. Comparison of LIR measurements made for different rail surface conditions over Section A.....	128
Figure 9-1. Proposed setup of a single-channel optic LIDAR system and bipolar switching mechanism; The LIDAR system measures the left rail speed when the switch is in mode I, and it surveys the right rail when shifted to mode II.	131

Figure 9-2. Different scanning configurations are possible for the bipolar LIDAR setup. In the 2-points embodiment each rail is surveyed at one point, while the 4-points system provides 2 scanning points for each rail.	132
Figure 9-3. Illustration of left and right track speed variation over a track panel that consists of a left curve, a tangent segment, and a right curve.	133
Figure 9-4. Track degree of curvature is calculated based on the left and right track forward speeds difference.....	134
Figure 9-5. The testing setup configured to collect preliminary data for proof of concept of the bipolar LIDAR scanning system.....	135
Figure 9-6. Speed measurement results for two switching cycles; R represents the scanning duration of the right rail, and L shows the surveying duration of the left rail. The scanning frequency is 0.25 Hz and 40% of the survey is allocated to each rail.	136
Figure 9-7. The bipolar LIDAR system speed measurements are used to calculate the left and right track speeds. The velocity on each rail is assumed unchanged once the LIDAR laser is directed to the other rail.	136
Figure 9-8. A close-up view of the speed measurements for one scanning cycle. A 3 rd order low-pass filter is applied to the raw speed. The left and right track speed variation determines the track curvature.	137
Figure A-1. Details of the IMU system used on the research car.....	147
Figure B-1. Surface feature aspect ratio measurements for bare rail in Test 1. The average H/D ratios for Sections A and B are 0.26 and 0.31, respectively.	148
Figure B-2. Surface feature aspect ratio measurements for bare rail and rail with ToR friction modifier (Test 2). The average H/D ratios for Sections A and B are 0.061 and 0.326, respectively.	149
Figure B-3. Surface feature aspect ratio measurements for bare rail and rail with sawdust (Test 3).	149
Figure B-4. Surface feature aspect ratio measurements for bare rail and rail covered by coarse sandpapers (Test 4).	150
Figure B-5. Surface feature aspect ratio measurements are compared in order to assess the repeatability of the rail surface monitoring system measurements. (Tests 4 and 5).....	150
Figure B-6. Comparison of LIDAR speed measurements during Tests 4 and 5.	151
Figure B-7. Comparison of H/D measurements made for the tested coatings: friction modifier, sawdust, and sandpaper.....	151

List of Tables

Table 3-1. Total Distance measured by the encoder and LIDAR system compared with the ground-truth distance obtained with a measuring wheel.....	34
Table 3-2. Segmented distances measured with ground-truth equipment as well as the encoder and LIDAR system.	34
Table 4-1-Numerical values used in the processing of LIDAR data for calculation of lateral track geometry parameters.....	46
Table 5-1. Numerical values used in the processing of LIDAR data for calculation of vertical track geometry parameters.....	70
Table 7-1-Model parameters used for the numerical evaluation of the proposed degradation model.....	109
Table 8-1. The testing protocol designed to evaluate the LIDAR system application for rail surface monitoring.....	116
Table 8-2. A summary of the surface ratio calculations for Section A with various rail surface conditions.	128
Table B-1. A summary of the H/D calculations for various rail surface conditions.....	151

Chapter 1 Introduction

1.1 Motivation

Monitoring and assessing rail track geometry condition plays an important role in railway safety control and track maintenance [1]. Excessive track geometry variations, if not repaired, can lead to large wheel and axle forces, resulting in derailment, excessive body acceleration, rail deterioration, and damage to the track infrastructure. Today, almost all rail administrators make use of autonomous track geometry inspection systems or metrology cars [2] to routinely collect the geometry data and identify weak locations along the track. Rail geometry maintenance by the use of inspection cars is, however, very costly since these cars are expensive and require operators [2]. Rail administrators are also expected to monitor and keep the track-induced noise and disturbance below certain destructive levels. Vibration and structure-born noise are typically measured in a stationary manner at the foundation of buildings near the track lines by the use of accelerometers [3]. A portable, non-contact, onboard track vibration monitoring tool is, however, very desirable to the railroads since it facilitates the measurements and enables them to make certain inspections on any location of the track whenever it's required. In addition to rail irregularities and dynamics monitoring, accurate train speed and location detection are crucial to rail transportation planning and safety. Conventional track speed sensors, including tachometers, radars, and GPS, individually or in combination, all have failure modes at low speeds and inaccuracies proportional with increased speed. The accuracy of the wheel-mounted encoders are significantly affected by the wheel slippage and/or slide, as well as wheel wear over time. Moreover, radars do not operate below a few miles per hour, and GPS units do not receive signals underground or in tunnels.

Rail surface (top of the rail) monitoring is critical for risk management and rail failure prevention. Rails are systematically inspected for severe surface defects that could result in large wear rates and potentially catastrophic rail failures. The rail surface inspections are usually performed visually by trained railway personnel. Top of the rail (ToR) lubricity condition is also periodically inspected by the track administrators. The ToR data are further evaluated and used

for track and maintenance planning, lubricator adjustment, lubricant effectiveness evaluation, and train speed settings.

A multi-functional LIDAR (Light Detection And Ranging) system is studied for the non-contact, simultaneous measurement and detection of track speed, rail lateral and vertical profiles, track-induced dynamics, and rail surface conditions. LIDAR, as used for speed sensing, is an accurate, non-contact speed measurement technique that uses the Doppler frequency shift imposed on laser radiation reflected from a moving object. Based on the Doppler frequency shift, the speed of a moving object is determined. Doppler LIDAR optics are used to measure the vehicle speed and vertical and lateral profiles of the left and right rails at the same time. A continuous track-induced vibration monitoring is also possible using the Doppler LIDAR optics. Additionally, the Doppler shift spectrum characteristics of the laser radiation reflected from the rails can be used for rail surface roughness and lubricity monitoring.

1.2 Objectives

The primary objectives of this study are to:

- Determine what aspects of track geometry can be measured with the Doppler LIDAR velocity sensing system.
- Demonstrate the applicability of the LIDAR system for the simultaneous measurement of track speed, distance, track curvature, and track irregularity variations.
- Determine if the Doppler LIDAR system can be used to replace the conventional track geometry inspection systems, such as inertial measurement units (IMUs).
- Evaluate the accuracy of the LIDAR sensors in measuring track irregularities as compared with other established rail inspection techniques.
- Study the applicability of the Doppler LIDAR technology for capturing the track-induced dynamics and vibrations.
- Install the prototype system onboard a metrology car with the appropriate, rigid fixtures that can survive the demanding railroad environments.

- Perform comprehensive field tests and collect real-time track geometry data from the Virginia Tech's LIDAR system and the geometry car equipment for the purpose of performance evaluation and comparison.
- Investigate the applicability of the Doppler LIDAR technology for rail surface monitoring.
- Evaluate the possibility of reducing the number of optics required for track speed and curvature measurements.

1.3 Approach

The following approach is used to address the issues presented in this study:

- The ability of LIDAR to measure the speed of a moving rail vehicle in a non-contacting manner is extended to capture the lateral and vertical irregularities of the track itself.
- Processing algorithms are developed to separate the speed components caused by the track motion and/or spatial irregularities from the left and right track speed components. This separation is possible due to the inherent separation of each phenomenon with respect to its spatial/temporal frequencies and related bandwidths.
- A laboratory-grade LIDAR system, available at the Railway Technologies Laboratory (RTL) of Virginia Tech (VT), is body-mounted to the Norfolk Southern research car.
- Four slightly-tilted LIDAR optics are used to measure the vehicle speed and vertical and lateral profiles of the left and right rails at the same time. Two gage face lenses are used to monitor the lateral geometry parameters, and two other lenses are pointed to the gage corner lenses in order to monitor vertical geometry parameters
- A 1000-ft tangent section of track near the Roanoke area is measured manually to obtain a ground-truth test section for calibration of the LIDAR system. White-painted markers are placed at designated intervals along this section to generate a signal from an optical sensor onboard a Norfolk Southern research car. When the geometry car travels over the test section, flags are produced by the fiduciary sensor and are correlated with the speed and processor clock to obtain a distance estimate between the markers. The ground-truth

distance measured between markers is used to calibrate the LIDAR data by adjusting the system's estimation of distance traveled.

- The data accumulated during the tests are processed using different signal processing techniques to obtain the measurements of interest: track speed, distance, curvature, left and right alignments, gage variations, and left and right profiles. Comparisons are made between the LIDAR measurements and the encoder, IMU, and the gage sensor data to establish the relative accuracy of the system.
- The results of the tests are used to provide an assessment of the LIDAR system's functionality in a rail environment.
- A data aligning method is used to spatially correlate the LIDAR geometry track data with a reference spatial data. This algorithm eliminates the need for GPS data, and it also allows for local correction of the measured data.
- The universality of the measurements is investigated by analyzing the data for the different sections of the track.
- Probability analyses are performed for the LIDAR, IMU, and gage sensor data. The results showed a good agreement between LIDAR measurements and other established inspection methods.
- A length-based track quality index (TQI) is developed to numerically assess the geometry measurements made by the LIDAR sensors.
- A phenomenological modelling approach is adopted to capture the degradation of geometry quality over short track segments. The method includes the historical data, current track conditions collected by the LIDAR system, and traffic data to calculate the track deterioration condition and identify the geometry defects.
- Two rail surface measures are introduced based on the Doppler shift spectrum characteristics of the laser radiation reflected from the rails. These two indices provide relative indications of the rail surface condition.
- Laboratory tests are carried out to evaluate the application of the LIDAR system to detect different rail surface materials and conditions, including roughness, rail lubrication, ToR friction modifiers, and leaf residues.
- A bipolar switching mechanism is introduced to develop cost-effective, single-channel LIDAR systems for railroad track speed and curvature measurements.

- A single-channel LIDAR system is prototyped to prove the proposed rail scanning concept.

1.4 Contributions

The potential contributions of the research presented in this study to LIDAR technology and railroad geometry inspection technology are:

- Development of an innovative multi-functional system for railroad health monitoring.
- Provision of accurate records of rail monitoring parameters such as track forward speed, distance traveled, track curvature, alignment, gage variations, track elevation, and vertical profiles.
- Extension of LIDAR applicability and further development of LIDAR technology in the demanding railroad environment.
- Introduction of a method of railroad monitoring that is versatile in physical configuration, allowing more focus on a particular target parameter if desired.
- Provision of an alternative to a wheel-mounted, rotary encoder, inertial measurement units, and rail geometry inspection equipment with a single optical system.
- Establishment of a length-based track quality index to evaluate the overall track geometry condition and identify the track geometry defects based on the speed measurements.
- Development of a track deterioration model to describe the changes in the LIDAR-based track quality index and to predict the future quality of the railway tracks monitored by the LIDAR system.
- Development of LIDAR-based rail surface ratios for quantifying rail surface materials and rail structural integrity.
- Introduction of a scanning concept in order to develop cost-effective, single-channel LIDAR systems for railroad track speed and curvature measurements.

1.5 Outline

- Chapter 1 introduces the study and provides the objectives, approach, potential contributions from the research, and an outline of the dissertation.
- Chapter 2 provides the technical background for the study. The primary track geometry parameters, track quality indexing, track speed and curvature detection, rail monitoring techniques, and Doppler-based LIDAR speed measurements are presented. Virginia Tech's use of the LIDAR technology for the railroad applications is also introduced.
- Chapter 3 details the LIDAR system installation onboard a metrology car, as well as the system calibration.
- Chapter 4 discusses the application of the LIDAR system for the lateral track irregularity measurements.
- Chapter 5 presents the processing technique developed for the vertical track geometry variations detected by the use of LIDAR optics. The testing results are also presented.
- Chapter 6 introduces the application of Virginia Tech's LIDAR for speed detection in the presence of track-induced dynamics and vibrations.
- Chapter 7 presents the track quality indexing and rail degradation modeling based on the speed measurements made by the Doppler LIDAR optics.
- Chapter 8 investigates the application of LIDAR technology for rail surface monitoring. Lab testing results are provided to support the proposed rail surface assessment measures.
- Chapter 9 introduces a scanning concept to develop single-channel LIDAR systems for track curvature measurements.
- Chapter 10 provides a summary of the work and a direction for further investigation into LIDAR applications for rail monitoring.

Chapter 2 Literature Review and Background

This chapter provides the technical background necessary for understanding the principles underlying the research performed in this study. An overview of track geometry characteristics is presented, along with a brief introduction of the available railroad inspection techniques. Next, a background of rail track quality indexing is presented, followed by an introduction to rail quality deterioration modelling. Rail surface monitoring is detailed as a common practice to prevent catastrophic rail failure events. The chapter is concluded with introducing LIDAR technology as a reliable tool for various rail monitoring applications.

2.1 Track Geometry Irregularities

Rails are laid and installed along a nominal centreline, which is the ideal path of the track. However, no track is placed perfectly, and there will always be small deviations from the nominal path. The irregularities that occur laterally are described by left and right alignment and gage, while the vertical irregularities are described by the left and right surface profile, and cross level.

Excessive track geometry variations can lead to large wheel and axle forces, resulting in derailment, excessive body acceleration, and damage to the track structure. Local track geometry defects enhance contact stresses by dynamic effects and can therefore cause fatigue cracks at particular locations along the track [4]. Rolling contact fatigue (RCF) studies in the UK Network Rail system [5] indicated that the probability of rail contact fatigue clusters formed due to geometry variations is high over curved tracks. On freight railroads, track geometry errors such as tight gage and cross level errors introduce localized RCF defects [6]. Such errors are associated with increased contact stresses due to the increases in dynamic wheel loads.

In the following section, the primary track geometry parameters that can be measured by the LIDAR system are introduced and briefly discussed.

2.1.1 Alignment

Track alignment is defined in terms of variation in the lateral positions of the left and right rails from a mean trajectory over a specific length of the track. Alignment deviations for the left and right rails are illustrated in Figure 2-1. Alignment can be measured manually using chord-based approaches, where the lateral offset of the rail from the center of a string stretched between two ends touching the rail side is obtained at multiple locations [7]. A positive deviation in the alignment denotes a lateral deviation of the track to the left, while a negative deviation in the alignment corresponds to a lateral deviation of the track to the right.

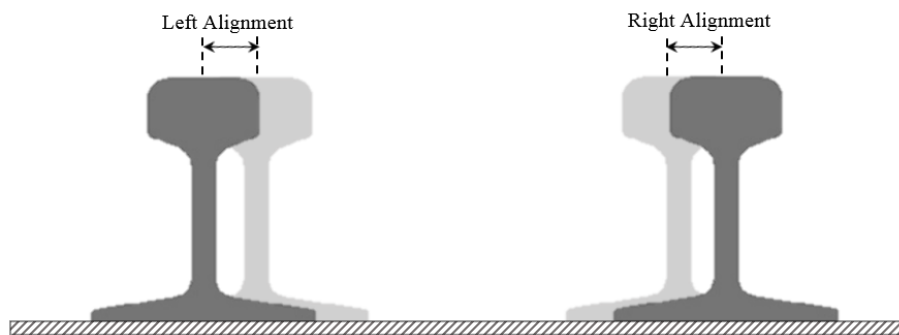


Figure 2-1. Track alignment deviation

2.1.2 Gage

Gage is defined as the distance between the two rails measured $\frac{5}{8}$ inches below the top of each rail. Gage can be measured manually using a gage measuring stick [7]. Gage can also be defined as the lateral deviation of the track from its nominal gage, which is 56.5 inches on the U.S. railroads, as shown in Figure 2-2. Gage variation is commonly used when discussing the track geometry. Positive gage variation represents the widening of the gage, while a negative variation corresponds to a narrowing of the gage. Gage can be measured manually using a gage measuring stick [7].

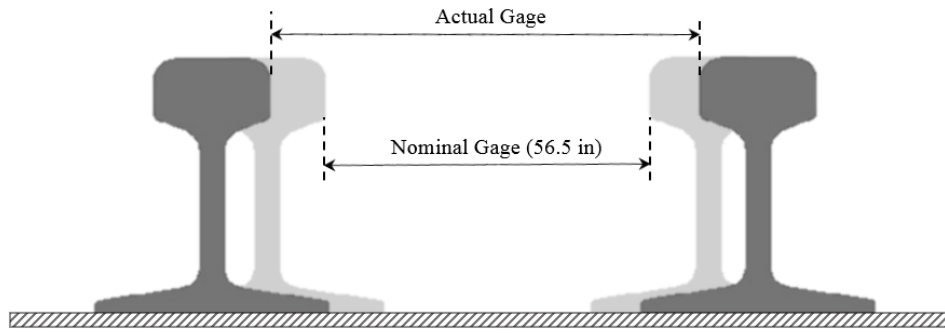


Figure 2-2. Track gage variation

2.1.3 Profile

Track profile (or surface) is defined as the vertical deviation of the midpoint of the two rails from the nominal (ideal) elevation, as shown in Figure 2-3. A positive profile variation corresponds to an upward vertical deviation of the track, while a negative variation refers to a downward vertical deviation of the track.



Figure 2-3. Track profile variation

2.1.4 Cross level

Cross level is defined as the vertical difference between the left and right rail from the nominal distance, as depicted in Figure 2-4. The intended distance refers to the amount of superelevation. For example, if superelevation is zero, then any difference between the elevations of the left and right rail is the cross level or track elevation variation. A positive cross level represents a situation when the left rail is placed above the right rail, while a negative cross level refers to a case when the left rail is laid below the right rail.

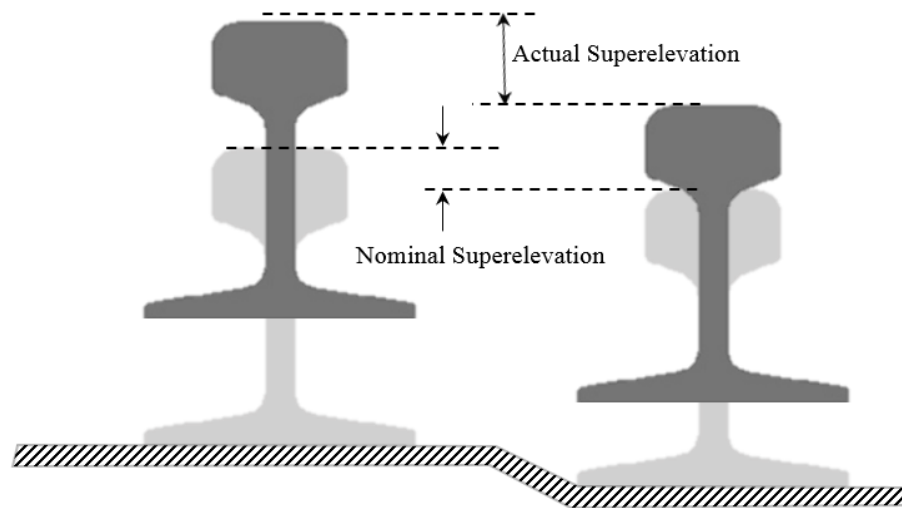


Figure 2-4. Track elevation variation

2.2 Track Irregularity Measurement and Evaluation

Monitoring and assessing track geometry condition plays an important role in railway safety control and track maintenance [1]. Today, almost all rail administrators make use of autonomous track geometry inspection systems [2], [8] to routinely collect the geometry data and identify weak locations along the track. These cars are equipped with different monitoring units and sensors. However, railway maintenance by using inspection cars is costly because these vehicles themselves are expensive and still require operators [1], [2], [9].

Estimation of railway irregularities by measuring and evaluating the acceleration is a well-established track monitoring approach. Vertical and lateral track geometry irregularities have been estimated from left and right vertical and lateral body accelerations above a bogie using an inverse dynamic model in reference [10]. Westeon et al. [11] demonstrated the track irregularity monitoring using bogie-mounted sensors. Alfi et al. [12] presented a technique for estimating long wavelength track irregularities with the use of onboard measurements. In their work, track irregularity was decomposed into harmonic components in frequency domain. In a recent work, Tsunashima [13] demonstrated a track geometry technique using car-body vibration. In an inverse problem to estimate track irregularity from car-body motions, a Kalman Filter was applied to solve the problem. Results showed that track irregularity estimation in the vertical direction is possible with acceptable accuracy. An advantage of the car-body acceleration measurement devices is their simple structure, which make it easier to carry out maintenance. However, the car-body acceleration waveform is considerably different from track geometry, and the amplitude greatly depends on the vehicle speed.

Vertical parameters are conventionally measured by the use of an inertial measurement unit (IMU) [14]. IMU works based on a simple rule where double integration of the acceleration identifies a position. For example, the vertical position of a wheel can be computed by the double integration of the axle-box acceleration. Despite their simple structure, IMUs commonly cannot be relied on at speeds below 10 mph. Train-track interaction simulation methods have also been developed, by which the vertical response of tracks subjected to a moving car can be studied. Zakeri et al. [15] assumed the rail to behave like a Raleigh-Timoshenko beam, and the wheel/rail contact to behave as non-linear spring elements. Their model was able to simulate the vertical dynamic interaction between track and train, and permit calculation of vertical deflections and forces. Similar research has been conducted by Berggren et al. [16] by the use of wavelength spectra analysis of rail data, which allows for frequency domain studies in addition to time-domain analysis. Although modelling techniques provide low-cost estimation of track quality, their accuracy has always been questionable due to their sophisticated parameter calibration procedures and simplification assumptions.

2.3 Track Class

The Federal Railroad Administration (FRA) divides track into six classes commonly used by Class I freight railroads. The higher the FRA class, the higher the maximum permissible speed. FRA track class designation is determined by the deviations from the ideal track, and they are used to regulate the safe operating speed for different types of traffic.

2.4 Track-induced Vibration

From the point of view of those who live alongside the railway lines, track-induced noise and vibrations are very irritating and disruptive. Therefore, rail administrators are expected to keep this disturbance below certain destructive levels. Track vibrations are mainly caused by large fluctuating forces between rails and wheels when a train travels on the rails. The fluctuation in forces originate from wheel roughness and/or track irregularities. Track vibrations predominantly occur at lower frequencies below 50 Hz [9].

Vibration transmission and structure-born noise are commonly measured and investigated in a stationary manner at the foundation of buildings near the track lines using accelerometers [3]. These studies determine the severity and magnitude of the transmitted track-induced vibrations. Vibration measurement is not, however, confined to stationary in-site acceleration measurements, as track vibrations can be directly monitored. Continuous vibration monitoring is possible using LIDAR technology [17], [18].

2.5 Track Quality Index

Track quality indices (TQIs) are traditionally used to quantify the track geometry condition. TQI is a numerical indication of the ability of track to perform its design function, or more precisely, to support the train movements required of it [19].

There are various numerical methods to compute TQIs according to required regulations and available measuring systems. Amtrak developed a track roughness index, which is calculated by

dividing the summation of the squares of deviations over the 20m mid-chord offsets by the number of measured points [20]. A five-parameter track defectiveness calculation method is being used in Austria to evaluate the track quality from the data obtained from geometry recording cars [21]. Chinese Railway uses the standard deviation of geometry measurements made over 200/500m unit track lengths [22]. In an FRA-funded project, length-based TQIs were developed to complement the federal track safety standards. In this method, a set of TQIs, each for profile, alignment, cross level, and gage are calculated from the ratio of traced space curve length to the track segment [23].

2.6 Track Geometry Deterioration

Track geometry deteriorates over time as a result of dynamic loads. Predicting the future quality of the railway tracks is of vital importance in maintenance planning. Normally, a track deterioration model is applied to describe how a particular TQI changes in a section of track within a specified time period [24]. A track quality degradation model must be able to include the influence of maintenance activities on the evolution of track degradation. In 2002, FRA applied a fractal analysis technique and developed numerical indices for track condition assessment [25]. Kawasaki et al. [10] developed a degradation model based on standard deviations of track geometry measurements to predict standard deviations of track alignment over 100m track sections.

2.7 Rail Surface Defects

A rail is defined as having failed once the accumulated damage exceeds an acceptable threshold such that it is no longer operational. Some of the most common rail surface defects are corrugation, squats, and head checks. Corrugation is a periodic top-of-rail surface irregularity with a wide wavelength range of (25-300) mm. Rail corrugation results in noise and high frequency vibration of the rail vehicle. Depending on the severity and characteristics of the corrugation, grinding operations are performed to restore the rail surface. Squats are single, isolated defects that usually occur at corrugations or welds. Squats create surface cracks that, if not preserved, could potentially result in rail failure. Head checks are continuous series of rail

cracks that typically occur on high rail in curves due to large cornering forces. Most of the head checks appear in gage corner, and they could result in large wear rates and potentially catastrophic rail failures.

Rails are commonly grinded or milled out to remove surface defects. However, there is a limit whereby the cost of the treatment exceeds the expected life extension (remaining wear life of the rail) [6]. Severe surface defects such as crushed heads or squats must be detected and removed in a timely manner because of their potential for initiating a broken rail. A rail failure event, while obviously a derailment risk, is also an expensive occurrence since it results in unplanned maintenance operations and traffic disruptions. For the heavy haul U.S. railways, the standard practice is to remove a length of rail once a rate of 1–2 defects/km/year is reached [26]. All railways have specific instructions for maintenance operations and remedial actions when a rail defect is detected. These treatments are usually based on the type, severity, and size of the defect.

2.7.1 Rail surface monitoring

Non-destructive testing of rails is critical for risk management and rail failure prevention. Rails must be systematically inspected for surface defects that might appear benign to the naked eye, but can be measured to be progressing internally to a dangerous state. The surface condition of rail is currently assessed visually by trained railway personnel [6], often from a Hy-Rail vehicle. This information, along with track data collected by the inspection cars, determines some of the rail maintenance operations, including rail relay program, defect removal through rail plugging, and rail grinding.

Different non-destructive inspection techniques have been evaluated for rail surface measurements. Accelerometers, typically mounted on the axle box, have been used to detect short wavelength defects such as squats [27]. Ultrasonic systems can effectively inspect the rail for internal defects, but they showed poor performance at detecting surface defects [28]. Eddy current systems provide faster inspections and are able to detect surface defects [29]. Magnetic particle inspection methods make use of an externally applied magnetic field or electric current through the rail to detect flow distortion caused by surface defects [30]. Vision systems also exist for scanning and recording various track features, but they cannot yet provide a quantitative

assessment of the defects. Rail radiography, longitudinal guided waves, electromagnetic acoustic transmission, and acoustic emission has also been tested for rail surface inspection applications [28]. According to [6], at present no commercially available RCF crack detection system is in service in North America. The application of LIDAR speed sensing technology for rail surface measurements is investigated in Chapter 8.

2.8 Rail Lubrication and Friction Modification

Rails and wheels are lubricated for various reasons. Lubrication of the rail gage face/wheel flange can significantly reduce the gage face/flange wear [31]. Lubrication can also contribute to reductions in RCF defects by reducing traction. Although on clean (healthy) rail, the reduced traction delays the crack formation [32], oil contamination of existing surface cracks further increases the RCF crack propagation [33].

Top-of-rail (ToR) friction modifiers are periodically applied on the rails to decrease the friction coefficient in the rail wheel interface [34]. Stock et al. [35] conducted a full-scale test rig study to demonstrate the application of friction modifiers in reducing the rates of RCF formation. ToR friction modifiers are beneficial for noise reduction [36], short pitch corrugation suppression [37], lateral force control [38], and rail wear reduction [20].

There are two types of rail lubrication systems: wayside systems and wheel flange lubricators. Wayside systems directly dispense the grease to the rail. The lubrication is then picked up by the wheels and dispersed along the rail length. Wheel flange lubricators are mounted to the train, and the grease is first applied on the flange, which will be further transferred to the rail. Poor lubrication equipment or improper settings on lubricators may lead to insufficient lubrication or ToR friction migration, thereby compromising traction and braking.

2.8.1 Rail lubrication monitoring

Rail lubricity conditions are periodically inspected by the track administrators. The ToR data are further evaluated and used for track and maintenance planning, lubricator adjustment, lubricant effectiveness evaluation, and train speed settings. Although visual ToR inspection is a common

practice, the skill and experience of the inspectors play an important role in rail inspection. The accuracy and consistency of the observations are highly affected by the inspector's skills, and could result in inaccurate assessments [39]. Therefore, it is beneficial for the inspectors to be equipped with a reliable ToR lubricant detection instrument.

In a recent research study, Hasan [40], [41] developed a new, quantitative measurement method for accurately assessing the state of rail lubrication. This method takes advantage of the light reflection and dispersion properties of laser-based optical sensors to provide a repeatable, verifiable, and accurate measure of the presence of ToR friction modifiers on the rail. Specular reflection is measured on the unlubricated rail and then compared with the lubricated rail. A lubricated rail reflects less light compared with an unlubricated rail due to the absorption (less reflection) of light that occurs when lubricants are present on the rail. The measurement system was assembled in a self-contained, portable rail cart that can be pushed on the rail at walking speeds. The rail lubrication system was successfully tested on various tracks, including a revenue service track. It is worth noting that all of the test results presented in [40] and [41] were made at low (walking) speeds, and the ability of the system to perform at higher speeds (say, in the range of 20 to 40 mph) is not discussed. As discussed in Chapter 8, the LIDAR sensors could also provide a reliable, non-contact rail ToR monitoring instrument for field use, potentially in a semi-autonomous or autonomous manner.

2.9 Track Speed and Curvature Detection

Accurate train speed and location detection is crucial to rail transportation planning and safety. Several different methods are typically used to detect train speed and location, each of which have advantages and disadvantages.

The wheel-mounted encoders are the most popular train speed measurement devices. Encoders or tachometers are mounted to the wheel axle and record the wheel rotation. The robustness and reliability of the wheel-mounted encoders have made them attractive to the rail industry [42]. Tachometers, however, are limited by their resolution, sampling time, electrical noise, wheel slippage, and slide [43]. Wheel slippage and slide cause erroneous speed and distance measurements since the encoder is attached to the wheel. Several researchers have worked

toward diminishing the slide and slip error in the encoder. Saab et al. [44] applied a Kalman filter to observe the speed and acceleration readings. In their method, if the velocity readings met a certain condition, the velocity results were adjusted by using linear interpolation between the speed prior to and after the slip/slide error. Ikeda [45] developed a Computer and Radio Aided Train (CARAT) system to detect the slip/slide errors in the travelled distance calculations and to eliminate these errors from the results. Allota et al. [46] used two encoders attached to two different axles and suggested an algorithm that could estimate the train speed and position during start/stop accelerations.

Global Positioning Systems (GPS) are also used to measure the train speed and distance. GPS is widely used for train location detection in order to prevent collisions and allow for appropriate spacing between the trains. The train location is determined by using at least four satellites and evaluating the travel time between each of the satellites and the GPS receiver. The speed can then be calculated directly by using the Doppler principle [43]. Although they are easy to implement, GPS systems have several disadvantages. First, the GPS satellite signal available to the public, known as Standard Positioning Service (SPS), is ‘dithered’ by the military, which lowers the accuracy of the readings. The accuracy of a GPS is about $\pm 5\text{m}$, which means that it cannot distinguish between two parallel train tracks. Additionally, a GPS does not receive a signal underground or in tunnels, which can significantly limit the availability and accuracy of the GPS signal in certain areas [47].

Another popular technique for measuring train speed and location is an Inertial Measurement Unit (IMU). IMUs typically consist of both accelerometers and gyroscopes. Accelerometers measure the inertial forces of the train, from which the acceleration can then be derived. The acceleration is then integrated to obtain the speed and position of the train. In order to accurately determine forward train speed, the accelerometers should not be sensitive to vertical and lateral accelerations. Also, the accelerometer sensor must be perfectly horizontal to avoid detecting acceleration components due to gravity [42]. Gyroscopes measure angular rotation of the train. Currently, Spinning Wheel Gyros (SWG), Ring Laser Gyros (RLG), and Fiber Optic Gyros (FOG) are the most common gyroscopes used to identify train rotation. Among these gyroscopes, FOG gyros are the most popular because they are small, light-weight, cheap, and do not contain any moving components. One of the major benefits of an IMU is that it is a self-

contained system which does not require a line of sight and can operate in any weather condition and location (including underground) [43].

In addition to train speed and location, track curvature measurement is an essential part of track geometry testing and maintaining rail functionality. One of the first techniques to measure track curvature was the Hallade Method, known as a mid-chord measurement [48]. This method utilizes a chord of a certain length stretched from one point on the gage face of a curved rail to another. Then the versine or length from the center of the chord to the rail is measured, and the radius of curvature can be determined based on the Pythagorean Theorem. For railway applications, a 62ft chord is most often used to make a mid-chord measurement because each inch from the midpoint (31ft) to the rail is equal to 1 degree of curvature. Nowadays, track curvature is usually measured using an Inertial Measurement Unit, as mentioned previously. An IMU uses an accelerometer to measure centrifugal forces, and a gyroscope to measure rotational forces. When a train passes through a curve, the IMU detects the changes in the inertial forces, which are converted into curvature readings.

2.10 Doppler LIDAR Technology

Doppler Light Detection and Ranging (LIDAR) technology, as used for speed sensing, is an accurate, non-contact speed measurement technique that uses the Doppler frequency shift imposed on laser radiation reflected from a moving object. A Doppler LIDAR transmits high-quality, single-wavelength laser beams into the air and receives the light backscattered from the object. The frequency of the received light is shifted due to the relative motion between the laser and the target (Doppler effect). This Doppler shift, which corresponds to the velocity of the target, is then extracted using coherent homodyne or heterodyne optical detection methods [49], [50].

According to classical physics, with c as the speed of light, V as the relative speed of the moving target with respect to the emitter, \hat{e} as the unit vector of the incident light, and f_T as the transmitted frequency, the returned laser beam has the shifted frequency of f_R as: [51], [52]

$$f_R = f_T \left(\frac{1 + \frac{V \cdot \hat{e}}{c}}{1 - \frac{V \cdot \hat{e}}{c}} \right) \quad (2-1)$$

Therefore, the Doppler frequency (Δf) is:

$$\Delta f = f_R - f_T = 2f_T \left(\frac{V \cdot \hat{e}}{c - V \cdot \hat{e}} \right) \quad (2-2)$$

Since for most practical applications, $V \ll c$, so $(c - V \cdot \hat{e}) \rightarrow c$, and we can write:

$$\Delta f \approx 2f_T \frac{V \cdot \hat{e}}{c} \quad (2-3)$$

Equation (2-3) can also be written as a function of measured relative velocity ($V_m = V \cdot \hat{e}$) and the wavelength of the transmitted laser beam λ_T as:

$$\Delta f \approx 2 \frac{V_m}{\lambda_T} \quad (2-4)$$

Pulsed LIDARs are most widely known for their law enforcement uses and share many characteristics with Doppler LIDARs in terms of precision. LIDAR is currently used by police officers as an alternative to Radio Detection and Ranging (Radar) for motor vehicle speed detection. The LIDAR narrower, coherent laser beam is capable of targeting a single moving vehicle in high traffic areas, whereas Radar emits high-frequency radio waves in a wider beam angle by a factor of 10,000, which is more likely to hit multiple vehicles, thereby reducing accuracy of the speed detection. Although LIDAR proves more effective on crowded roads, weather conditions such as fog, rain, and snow can significantly affect the LIDAR's speed accuracy. Unlike LIDAR, the accuracy of Radar's speed reading is unaffected by weather [53]. Inclement weather, however, can diminish the detection range of Radar devices. Both LIDAR and Radar are still widely used by law enforcement, but LIDAR seems to be growing in popularity [54].

One major application of Doppler-based LIDAR sensors is to measure the wind speed for air traffic monitoring and safety. Radar was originally used onboard aircraft for the purpose of wind turbulence detection, but it showed inconsistency in measuring sudden wind turbulence in areas

without clouds or rain. In 2007, the Japan Aerospace Exploration Agency studied the effect of wind turbulence on the number of aircraft accidents [55]. They developed an onboard proactive LIDAR sensor that was able to detect wind speed at the range of 9 km at cruising altitude. Their sensor emitted a laser pulse, which was then reflected off air particulates in the wind. The resultant Doppler frequency shift was used to determine the wind speed. The onboard LIDAR optic showed a promising functionality in detecting wind turbulence and proved to be more reliable than Radar. The researchers determined that detecting the wind turbulence in advance will allow the pilot to take appropriate action, such as reducing speed or securing the passengers in order to minimize damage. Similarly, Doppler LIDAR is successfully used in Hong Kong to measure the terrain-induced wind shear [56]. Terrain-induced wind shear affects the aircraft stability upon landing and takeoff. Recently, Doppler LIDAR sensors have been used onshore and onboard ships to measure the offshore wind speed imposed on wind turbines [57], [58]. Researchers at Mitsubishi Electric have developed a Coherent Doppler LIDAR system for wind field sensing. This device has successfully proven its robustness and its efficient measuring accuracy through extensive field experiments [49].

LIDAR is also used by NASA to determine helicopter speed and altitude [59]. In 2009, the NASA Langley Research Center mounted a LIDAR optic to the nose of a helicopter. Tests were conducted on the helicopter, and the helicopter's speed and altitude were measured. The results for both speed and altitude were compared against GPS data, and the comparisons showed excellent correlations for both measurements.

2.10.1 Doppler laser measurements

A Doppler effect occurs with relative motion that is not necessarily accompanied by displacement of the mean range of the target surface. In the following, four different laser-target configurations that result in a Doppler effect are discussed. Figure 2-5 shows the first configuration in which the sensor is stationary and the target is moving. The laser strikes perpendicular to the moving surface. The laser beam is transmitted at the wavelength of λ_t and is returned at the wavelength of λ_R . In this case, the perceived returned wavelength (λ_R)

increases if $V > 0$ and it decreases if $V < 0$. The measured velocity by the Doppler LIDAR is inversely proportional to $\lambda_R - \lambda_T$.

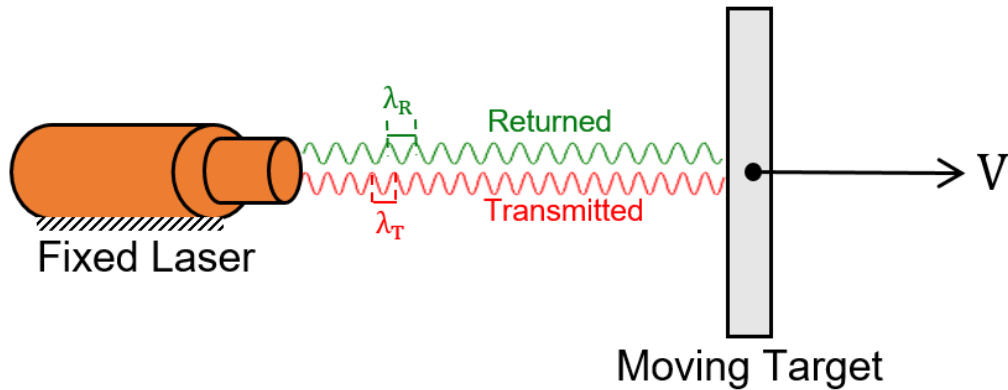


Figure 2-5. Measurement Configuration I: when a fixed laser strikes perpendicular to a moving target, the measured velocity is proportional to the difference between the transmitted wavelength and the returned wavelength.

The relative motion can be caused when the laser itself is moving, as depicted in Figure 2-6. In this case, similar to the first configuration (Figure 2-5), the laser beam strikes perpendicular to the moving surface, and the symmetric equations result in exactly the same Doppler shift. Therefore, the measured velocity by the Doppler LIDAR in this case is also inversely proportional to $\lambda_R - \lambda_T$.

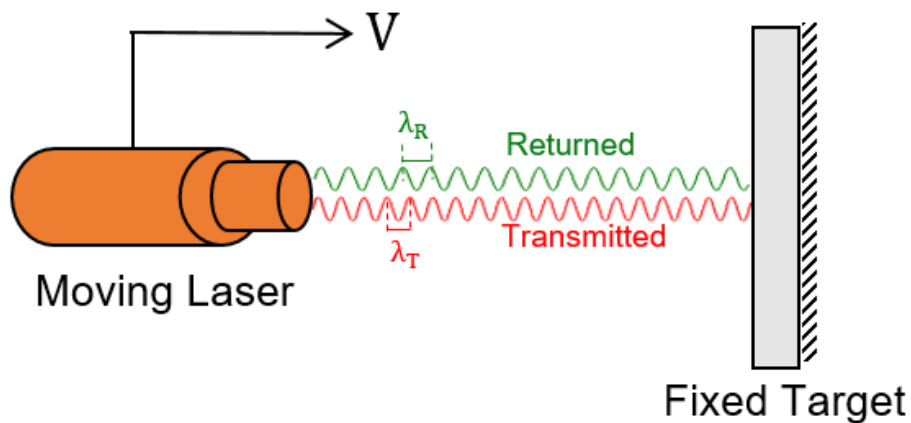


Figure 2-6. Measurement Configuration II: when a moving laser strikes perpendicular to a fixed target, the measured velocity is proportional to the difference between the transmitted wavelength and the returned wavelength.

The third configuration, as shown in Figure 2-7, describes a case in which a fixed sensor is oriented so that the laser is emitted to a moving target with a bias angle of θ . In this case, the velocity component in the direction of incidence (V_x) is the term that determines the wavelength variation ($\lambda_R - \lambda_T$), such that the perceived returned wavelength (λ_R) increases if $V_x > 0$, and decreases when $V_x < 0$. With this configuration, the velocity of the moving target (V) can be calculated as $V = \frac{V_x}{\cos\theta}$. It is very important to mention that for the measurement to be possible at oblique incidence, the target surface must have component of diffuse reflection because the laser beam must be backscattered to be received by the sensor.

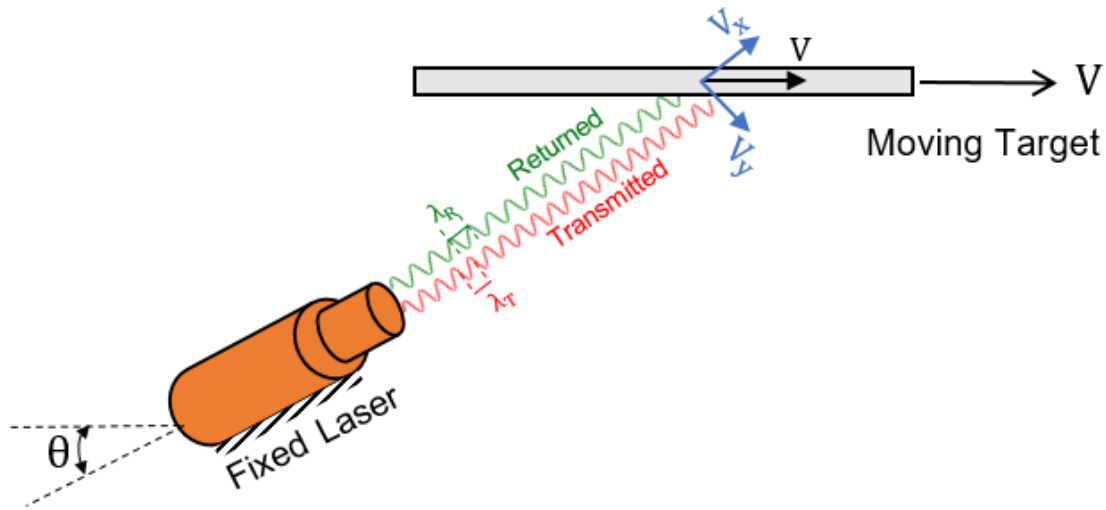


Figure 2-7. Measurement Configuration III: when a fixed laser strikes oblique to a moving target, the velocity in direction of incidence (V_x) is proportional to the difference between the transmitted wavelength and the returned wavelength. Measurement at oblique incidence is possible only if the target surface has diffuse reflection.

Figure 2-8 illustrates the fourth configuration, in which a moving laser strikes oblique to a fixed target. Similar to the third configuration, the velocity component in direction of incidence (V_x) is the term that determines the wavelength variation ($\lambda_R - \lambda_T$), such that the perceived returned wavelength (λ_R) increases if $V_x > 0$, and decreases when $V_x < 0$. Since the laser velocity (V) is the resultant of V_x and V_y , it can be calculated as $V = \frac{V_x}{\cos\theta}$. Again, Doppler velocity

measurement at this configuration is possible only if the target surface has a component of diffuse reflection.

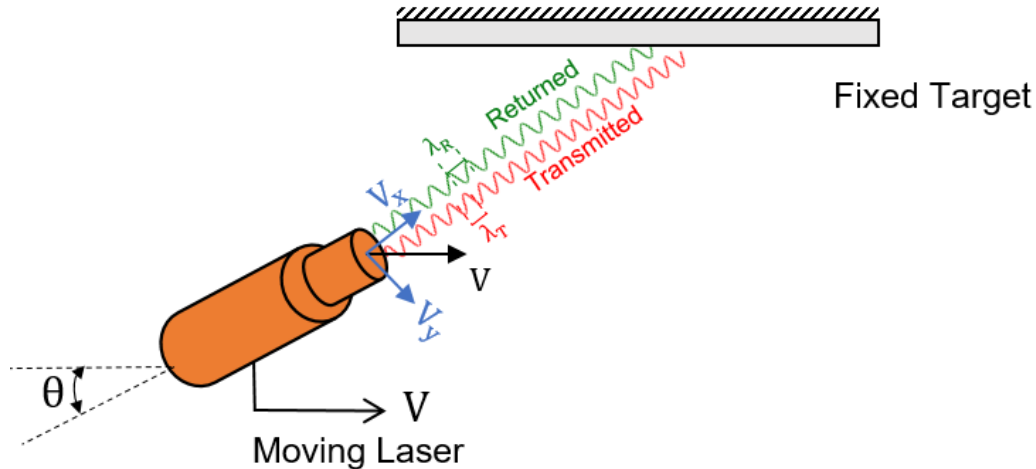


Figure 2-8. Measurement Configuration IV: when a moving laser strikes oblique to a fixed target, the measured velocity in direction of incidence (V_x) is proportional to the difference between the transmitted wavelength and the returned wavelength. Measurement at oblique incidence is possible only if the target surface has diffuse reflection.

The fourth configuration is adopted and used in this research for relative gage and profile deviation measurement. However, in this arrangement, from the perspective of the LIDAR system, it is the rail that moves through the stationary inertial frame of the laser as in the third configuration. Thus, it is the motion of the rail through this inertial frame that imposes a shift of momentum and photonic energy on the laser's emittance. It is worth mentioning that absolute range and profile cannot be measured with this technique.

2.10.2 Virginia Tech’s LIDAR system

A laboratory-grade LIDAR system is developed at Virginia Tech’s Railway Technologies Laboratory (RTL) for rail monitoring applications. The primary purpose for developing this system is to introduce LIDAR as a direct retrofit for encoders and inertial measurement units (IMUs) to the U.S. railroads. Virginia Tech’s LIDAR system offers a number of benefits to the rail industry. The non-contact measurement nature of Doppler LIDAR optics removes speed-

dependent design, reliability, maintenance, and accuracy issues otherwise seen in current tachometers. Additionally, the extensive amount of LIDAR data collected onboard metrology cars and Hy-Rail vehicles [60], [61] indicates that the LIDAR system can provide a reliable, non-contact track monitoring instrument for use over substantial track distance in inclement weather and harsh conditions with minimal operator supervision, comparable to high-precision track geometry applications, such as the FRA's Autonomous Track Geometry Measurement System [62], [63].

Figure 2-9 illustrates the concept inherent in using Doppler-effect LIDAR velocity sensors for rail inspection. The LIDAR sensor optics (i.e. lenses) are attached to the underside of a metrology car or a Hy-Rail truck with two laser beams propagating toward the left and right rails. The dashed arrow indicates the outgoing LIDAR beam, and the solid arrow shows the component of backscattered light returning to the sensor optics. The frequency differential between the emitted and reflected beams is the Doppler velocity shift for each rail imposed on the laser light by the motion of the rail vehicle. For the 1.5um lasers used in the VT LIDAR system, the frequency shift is 579KHz per mph [50]. Light signals are carried between the optical components, the laser source, and the processing electronics via optical fibers. As will be discussed later, the orientation of the laser beams with respect to the direction of rail travel and the mounting infrastructure, referred to as the LIDAR geometry configuration, is a function of the desired measurement function and can be highly variable by design. While the optical fiber connections provide a great deal of flexibility in configuring a LIDAR, they are not entirely necessary to a Doppler velocimetry system.

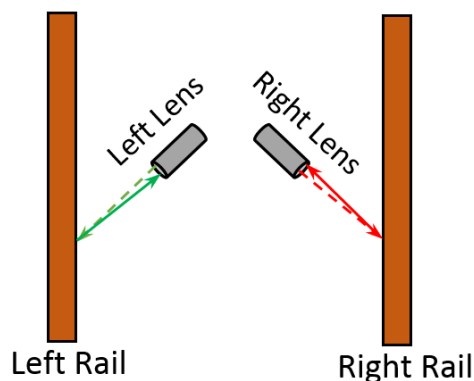


Figure 2-9. Simple schematic of LIDAR lens orientation with respect to the rail. The lenses serve as both light emitters and receivers.

As shown in Figure 2-10, the Doppler shift is electronically detected and passed to a digital central processing unit (CPU) through a high-fidelity RF amplifier and A/D converter. The CPU that is used for this work is a National Instruments (NI) PXI Computer that can be configured for industrial applications such as the rail LIDAR system. The PXI computer performs a number of tasks in real time, including computing the Fast Fourier Transform (FFT) of the two LIDAR signals, detecting the left and right rail velocities from the resulting complex frequency spectrum, and performing the necessary calculations for determining track centerline speed (based on the average speed of the two rails). Additional processing is currently achieved external to the LIDAR unit, but could be achieved internal to the unit with modifications to the unit's software. However, for the purpose of gathering scientific phenomenological data, such a procedure would unnecessarily lose the richness of the data. The track geometry data shown throughout this work is therefore data produced by externally post-processing the speed data via numerical filters to derive, smooth, correct, and calibrate the geometry parameters. Speed and distance measurements are analog and digital outputs of the PXI computer. Digital data is stored to a hard drive or solid-state drive (SSD) at a user-defined storage rate. Beyond track curvature and speed determinations, the internal post-processing of the LIDAR data includes a travel distance calculation that provides the basis for generating a foot-pulse signal, much in the same form as a conventional wheel encoder. The intent of the system is to demonstrate a direct retrofit capability for the wheel encoder and some geometry and rail inspection units in a track geometry car, without any changes to other instruments that use a foot-pulse signal for spatial demarcation of rail distance. Additionally, during post-processing, the LIDAR data can be assessed for rail surface inspection, data mapping, and spatial correlation. These features will be explained in the following chapters.

Although wheel-mounted encoders (also referred to as a tachometer throughout the dissertation) are robust, they are subject to non-linear slip, calibration variance with wheel diameter, and overshoot/undershoot. Wheel slip occurs when the wheel travels a shorter distance than an ideal wheel, which neither slips or slides. Wheel/rail contact condition is related to running states of the rail vehicle (such as accelerating, decelerating, climbing, and navigating curved tracks), environmental factors (such as snow, rain, fallen tree leaves, and sand/lubricant residues), and both profiles and materials of rail and [44], [64]. Although the extent of wheel slip is random, the

encoder's speed/distance measurements always include error [65]. Compared to the encoders, the non-contact LIDAR system provides track speed measurements with higher fidelity due to the absence of mechanical failures, high-speed parasitic slippage, and periodic recalibrations. As discussed in the following, the LIDAR system can act as a direct retrofit for the wheel-mounted encoder to trigger metrology equipment. The LIDAR system may also be used as a redundant speed sensor onboard a research car. In this case, LIDAR speed data can be implemented in data fusion algorithms to improve accuracy.

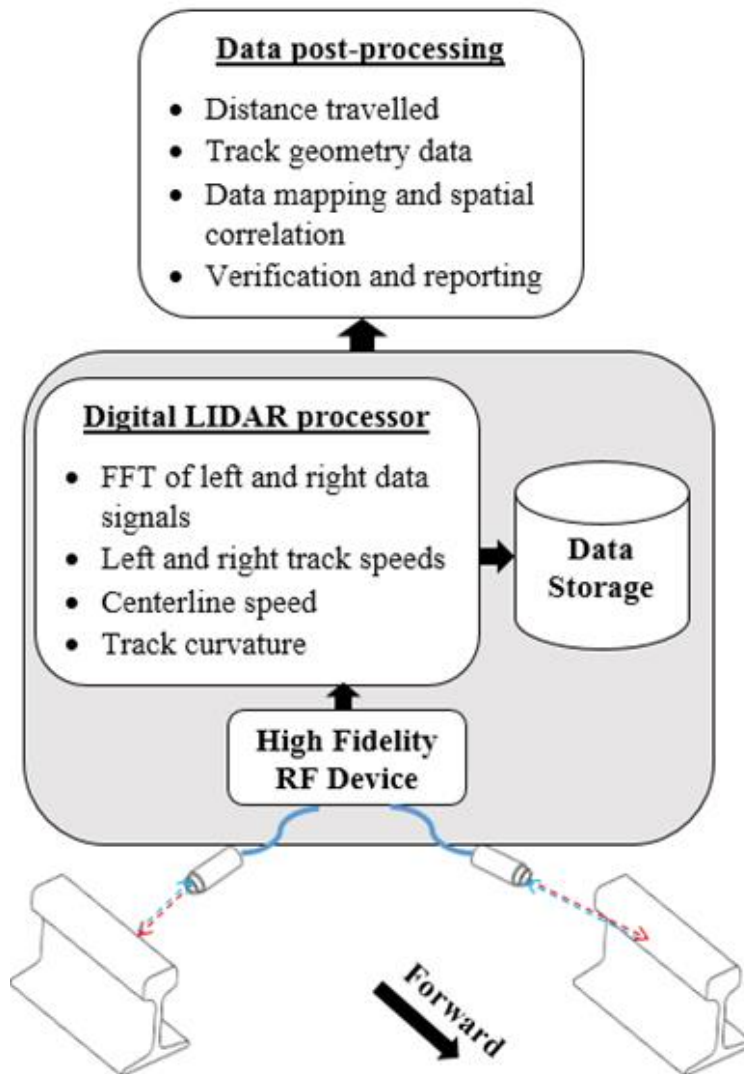


Figure 2-10. Block diagram of Virginia Tech's multi-functional LIDAR system for track speed and rail geometry measurements.

Current rail geometry car data measurement systems typically use an encoder to acquire per-foot demarcation of the measured data. A 10,000 pulse/rev encoder is scaled to generate a data acquisition pulse for every foot of forward travel in order to provide a spatial reference/displacement map of the data. This allows rail parameters such as gage and alignment to be located on rail track charts for maintenance. The system is “zeroed” at given distance intervals or rail fiducials to eliminate any drift or “skip” from the encoder, and to keep the measurements in sync with the ground-truth track charts. O’Connor et al. [66] evaluated the LIDAR system’s ability to act as a direct retrofit for the wheel-mounted encoder. They employed an external microcontroller to generate a foot-pulse signal using LIDAR speed measurements. This foot-pulse was then tested onboard the metrology car in a trial run. By producing a foot-pulse demarcation, the LIDAR system was able to emulate the wheel-mounted rotational encoder and trigger the acquisition systems of the metrology car.

The modern, conventional method of measuring track curvature employs Inertial Measurement instruments (IMU) installed on a Hy-Rail vehicle or a track geometry car. The advantage of the LIDAR system over IMUs is that it can measure track curvature at speeds far lower than is possible with IMUs that are commonly used in track geometry railcars. Experimentally, metrology car IMUs cannot detect curvature at speeds below 10 mph, while LIDAR can measure curvature below 0.5 mph [67]. This makes LIDAR suitable for instrumenting Hy-Rail trucks, which typically operate at lower speeds for local rail inspection operations. As discussed in chapters 7 and 8, the LIDAR system not only provides speed and curvature measurements, but its data may be further processed for track quality and top of rail surface monitoring. These auxiliary features make LIDAR more valuable for Hy-Rail applications. Moreover, LIDAR curvature comparisons with ground-truth data suggest that the LIDAR system is sensitive to instantaneous curvature changes and contains information about car body motion in addition to accurately recording general curvature data [68].

Virginia Tech’s LIDAR system offers a number of benefits to the rail industry, as compared with existing measurement units [69], including the following:

- LIDAR provides inherently accurate, speed-independent measurements with an absolute scale factor (580KHZ/mph). This factor is not subject to wear, track speed (slip and data rate), spatial resolution/standoff (Radar), environment, etc.

- LIDAR can operate over a wide range of track speeds (creep speed to hundreds of mph) that exceeds any current technology (analog/digital tachometers, radar, GPS, etc).
- LIDAR is a non-contact measurement technology that eliminates the speed-dependent design complexity, reliability, maintenance, and accuracy (slip) issues and limitations (e.g., vibration) of mechanically contacting or axle-linked tachometers (analog or digital).
- Track curvature measurement is possible by the LIDAR at far slower speeds than is possible with Inertial Measurement Units (IMUs), commonly used onboard the track geometry rail cars.
- VT's LIDAR is suitable for use onboard Hy-Rail trucks or portable units than can be operated remotely at walking speeds.
- With implementation of a data mapping algorithm, LIDAR's track geometry data can be accurately located along the track. This eliminates the need for a Global Positioning System (GPS).
- VT's LIDAR optical fibers operate in an eye-safe wavelength region ($\lambda = 1.5\mu\text{m}$).
- The optical fibers are flexible, which allows for arbitrary mounting locations and easier system integration.
- The VT's LIDAR coherent detection results in larger dynamic detection ranges than conventional intensity-based optical metrology sensors used for rail applications.
- Track speed can be detected on all surface materials (rock, steel, ice/snow, etc.), roughness (e.g., shiny or coarse), and colors (e.g., light or dark), while rejecting sun or artificial lighting (e.g., headlamps, etc.).

Chapter 3 Rail Geometry Inspection Car Testing

This chapter explains the installation and calibration procedures of the LIDAR system onboard the Norfolk Southern NS38 research car. Onboard tests are conducted to evaluate the applicability of the system for track geometry measurements. The data collected during the field tests are processed using different signal processing algorithms to obtain the track geometry measurements of interest, and the results are presented in subsequent chapters. The tests are also intended to ensure that the components installed underneath the inspection vehicle can withstand the vibrations, dirt, and grime that exist in a revenue service environment.

3.1 System Setup

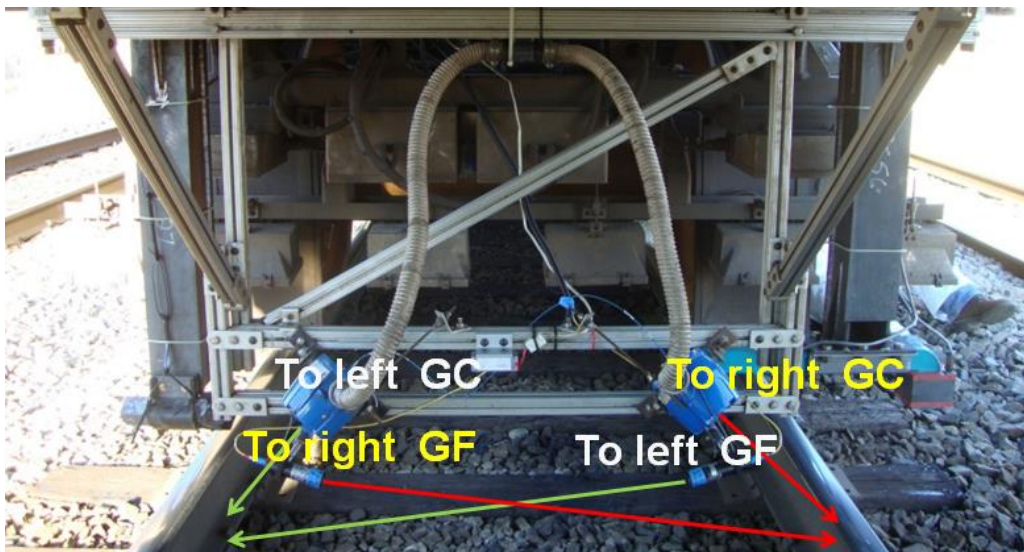
The LIDAR mounting frame is installed underneath the NS38 geometry car as shown in Figure 3-1. (a). Figure 3-1. (b) shows the system fastened to the underside of an NS rail geometry car. As shown in the figure, the frame supports four LIDAR lenses. The two lenses primarily employed for measuring train speed and vertical rail irregularities are enclosed in the blue housings. These housings contain positive pressure from air supplied by the attached hoses to protect the lenses from outside dirt and debris. The accelerometer is contained in the small case with a white label placed on the lower cross beam of the frame. The lenses oriented at the gage corner are angled 45° to the vertical axis and into the gage face, and are angled at 60° to the horizontal or longitudinal axis. The orientation ensures a near-constant contact angle on the rail, whether the beam transitions to the ToR or remains on the gage face due to motion of the car body. Because the lenses capture the component of the target's motion into the lens, the 60° orientation allows for a simple conversion factor of two to rail speed from that perceived by the detected Doppler shift. That is, true rail speed is twice that of the speed recorded by the system once it is compensated for the added 45 degree elevation angle.

A closer view of the lenses on the right side of the train is shown in Figure 3-2. The lenses that capture primarily gage variation are seen below the housings. They are oriented at shallower

vertical (elevation $< 5^\circ$) and lateral angles ($< 10^\circ$) to the normal of the gage face. These lenses capture gage variation, curvature, and/or alignment deviation of the rail on the opposing side. The lateral or “forward bias” angle is sufficient to allow for positive and negative deviations around the forward bias velocity of sufficient magnitude as to not fully cancel the Doppler bias imposed by the speed on the LIDAR beam



(a)



(b)

Figure 3-1. LIDAR body-mounted setup; (a) NS38 research car, (b) LIDAR mounting frame. LIDAR sensors are installed in blue housings to protect the lenses from dust and debris.



Figure 3-2. Close-up view of lens arrangement. The top lens is installed in a blue housing and captures rail speed. The lower lens captures rail alignment variation from the opposite rail.

The LIDAR processing system is located in the cab of the geometry car and is connected to the lenses below the car via fiber optic cables. Figure 3-3 shows the LIDAR computer set-up. The LIDAR computer is ported to the NS36 via the onboard KVM system. This allowed for system monitoring and control by an operator if needed.



Figure 3-3. LIDAR computer electronics are located in the cab of the research car.

3.2 Ground-truth Calibration

A ground-truth measurement was made near Roanoke, VA to calibrate the LIDAR system. A tangent track of 1,000-ft-long was selected and divided into five segments: including two 50-ft-long sections at the two ends and, three 300-ft-long spaces at the middle. These sections were measured by a glass-fiber tape and marked by six black and white fiduciary boards. As shown in Figure 3-4, boards were painted in black at the ends and in white at the middle to provide a strong fiduciary signal. They were mounted lengthwise on the center of the ties (Figure 3-5). The distances between the boards were also measured with a measuring wheel (Figure 3-6).



Figure 3-4. 4-ft-long fiducial boards were used for LIDAR distance calibration. Boards are painted in black at two ends and white at the middle to provide a good fiduciary signal.

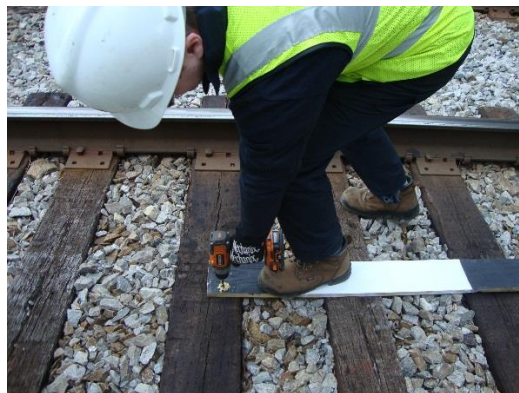


Figure 3-5. Fiducial boards were drilled to the ties.



Figure 3-6. Marked sections were also measured by a measuring wheel.

A fiduciary sensor was implemented to enable the system to capture the fiduciary marks. The sensor was installed in a cylindrical enclosure, as depicted in Figure 3-7, and mounted under the body close to the LIDAR frame.



Figure 3-7. Fiduciary sensor was installed inside a cylindrical enclosure and mounted under the body.

During ground-truth calibration runs over the tangent track test section, the train is moved over the fiduciary markers at a relatively low speed (a maximum speed of 4.5 mph was recorded on the test run under analysis) to ensure that the wheel encoder would have no binding or slippage. The calculated distance for the LIDAR is then compared against the distances measured by the tape, the measuring wheel, and the encoder, as shown initially in Table 3-1.

Table 3-1. Total distance measured by the encoder and LIDAR system compared with the ground-truth distance obtained with a measuring wheel.

Measurement Type	Distance (ft)
Measuring Wheel	997.25
Encoder	996.01
LIDAR	1000.90

Variance of the measurements in Table 3-1 from the tape measurement standard yields equivalent accuracies of -0.089%, 0.4%, and 0.274%, respectively for the measuring wheel, the geometry car wheel-mounted encoder, and the LIDAR. All applied measurement methods - tape measure, measuring wheel, encoder, and LIDAR - are then further compared in Table 3-2 for each of the five sections of the ground-truth tangent track, and analyzed statistically for error, which is essentially accuracy.

Table 3-2. Segmented distances measured with ground-truth equipment as well as the encoder and LIDAR system.

Section #	Fiber-glass tape (ft)	Measuring wheel (ft)	LIDAR (ft)	Encoder (ft)	LIDAR Error (in)	Encoder Error (in)	LIDAR Error %	Encoder Error %
1	50	49.88	49.76	49.67	2.88	3.96	0.48	0.66
2	300	299.20	300.01	298.59	0.12	16.92	0.0033	0.47
3	300	299.13	300.79	299.27	9.48	8.76	0.26	0.24
4	300	299.13	299.71	298.24	3.48	21.12	0.097	0.59
5	50	49.92	50.61	50.23	7.32	2.76	1.22	0.46

For subsequent tests, in order to determine the correct system calibration for field tests, the LIDAR calibration speed/angle constants are adjusted so that the distance measurements made here are scaled to exactly match the 1,000-ft ground-truth using the current results in Table 3-1.

A temporal comparison of the wheel encoder and LIDAR over the calibration test is plotted in Figure 3-8. The distance measurements taken during this run are also shown in Figure 3-9. These two figures serve to further illustrate the close correlation between LIDAR and encoder measurements, as well as to illustrate the higher instantaneous statistical variance inherent in the wheel encoder due to mechanical effects even at low track speeds.

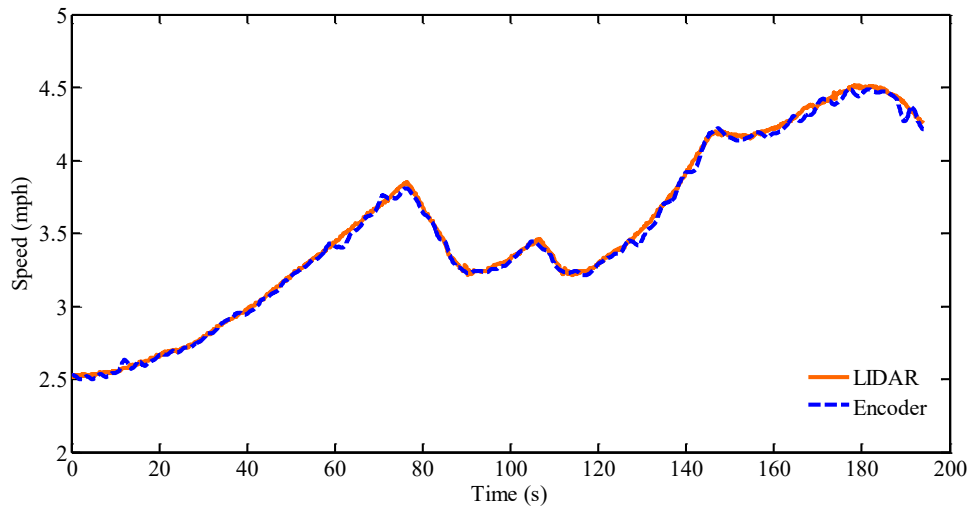


Figure 3-8. Speed profile of the calibration run as recorded by the encoder and LIDAR system. There is high correlation between the speed signals, however, the wheel encoder shows significantly higher instantaneous variation across the entire test run due to mechanical effects.

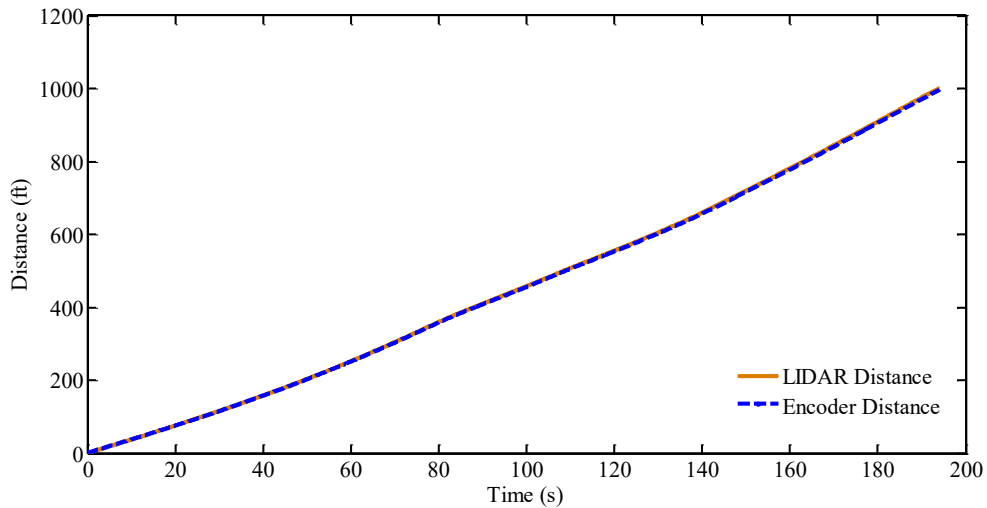


Figure 3-9. Calculated distance traveled by the encoder and LIDAR system. There is high correlation in distance measurement, as confirmed by the data provided in Table 3-2.

Following the low-speed ground-truth calibrations and analysis, a comparison is made between the LIDAR speed data and wheel encoder speed data across 40 miles of track to further evaluate the performance and accuracy of the LIDAR system prior to curvature testing. The encoder and LIDAR speeds match well, as shown in Figure 3-10. For this data sequence, speed difference between the two sensors is well under 1% at any point during the run.

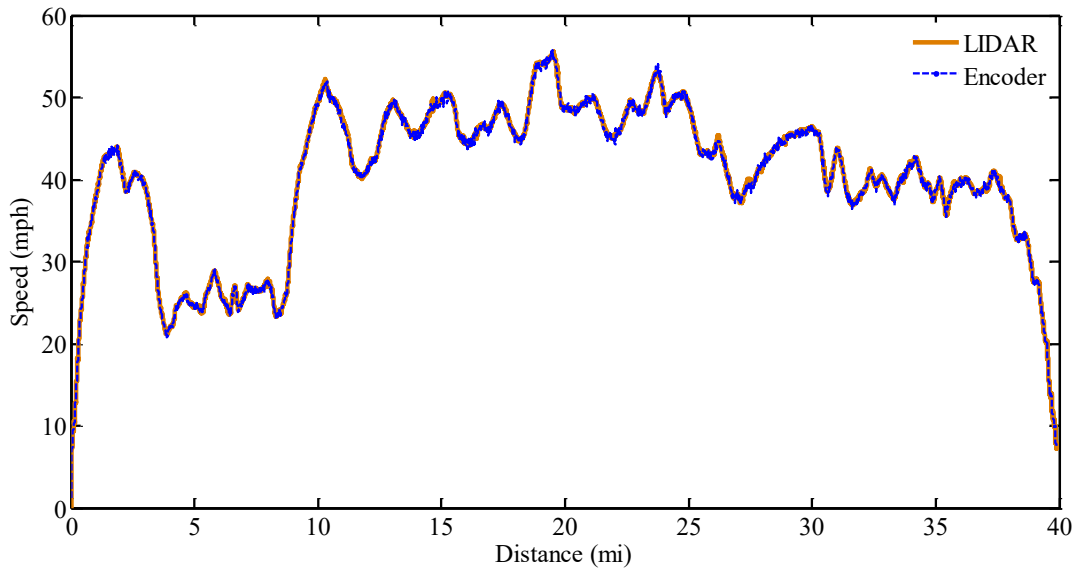


Figure 3-10. Using the information gathered from the calibration run, the appropriate gain in the LIDAR data is applied to match real conditions. The plot above shows the speed result after ground-truth calibration.

3.3 Test Routes

LIDAR data was collected for a round-trip between Roanoke and Lynchburg, VA (about 50 miles one way). Encoder speed data, onboard inertial measurement unit (IMU) data, and gage sensor data were also collected. The system specifications of the onboard IMU are listed in Appendix A. The data collected from the metrology equipment is used to evaluate the LIDAR measurements in the following chapters.

3.4 LIDAR Lens Orientation and Coordinate System

In this work, the rail coordinate system (X_R - Y_R - Z_R) is defined so that the X_R axis is aligned with the rail trajectory, and the Y_R axis is perpendicular to the gage face. This system is set as the reference frame for lens orientation and velocity vector definition. The lens coordinate system (X_L - Y_L - Z_L) is locally defined according to the lens orientation with respect to the track coordinate axes. Figure 3-11 shows the two Cartesian systems for an arbitrary LIDAR sensor

orientation. As this figure suggests, the lens coordinate is selected so that the laser beam strikes the rail along the Z_L axis.

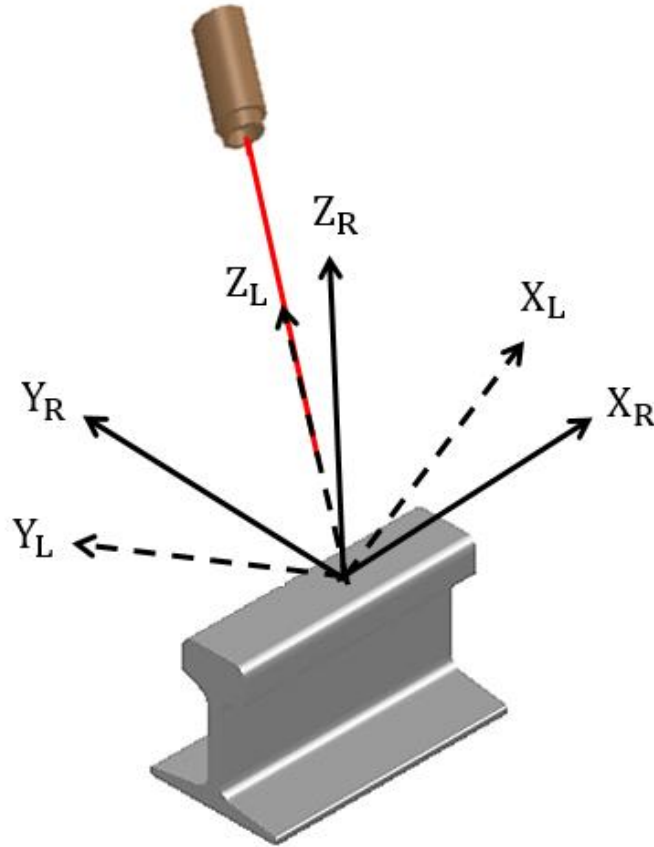


Figure 3-11. The laser coordinate system (X_L - Y_L - Z_L) is oriented with respect to the rail coordinate system (X_R - Y_R - Z_R). the lens coordinate is selected so that the laser beam strikes the rail along the Z_L axis.

When the LIDAR sensor is oriented with respect to the rail, the incident light is no longer perpendicular to the rail trajectory, and the Doppler frequency shift is affected by the motion in different directions (two or three different components based on the lens orientation). The laser beam strike direction (\hat{e}) should be determined with respect to the speed direction in order to correctly identify and separate the speed components.

The laser beam strike direction (\hat{e}) is derived by finding the transformation matrix that transforms the track coordinate system to the lens coordinate system. Before the transformation, the lens is positioned so that the beam direction overlays the vertical axis of the rail (Z_R). The

laser is then oriented with the order depicted in Figure 3-12. The coordinate is first rotated about the lateral axis (Y_R) with a bias forward angle of θ , followed by a rotation about the longitudinal axis (X_R) with an elevation angle of $-\varphi$. The transformation matrix for these rotations T_L is as follows:

$$T_L = \begin{bmatrix} 1 & 0 & 0 \\ 0 & \cos \varphi & -\sin \varphi \\ 0 & \sin \varphi & \cos \varphi \end{bmatrix} \begin{bmatrix} \cos \theta & 0 & \sin \theta \\ 0 & 1 & 0 \\ -\sin \theta & 0 & \cos \theta \end{bmatrix} = \begin{bmatrix} \cos \theta & 0 & \sin \theta \\ \sin \varphi \sin \theta & \cos \varphi & -\sin \varphi \cos \theta \\ -\cos \varphi \sin \theta & \sin \varphi & \cos \varphi \cos \theta \end{bmatrix} \quad (3-1)$$

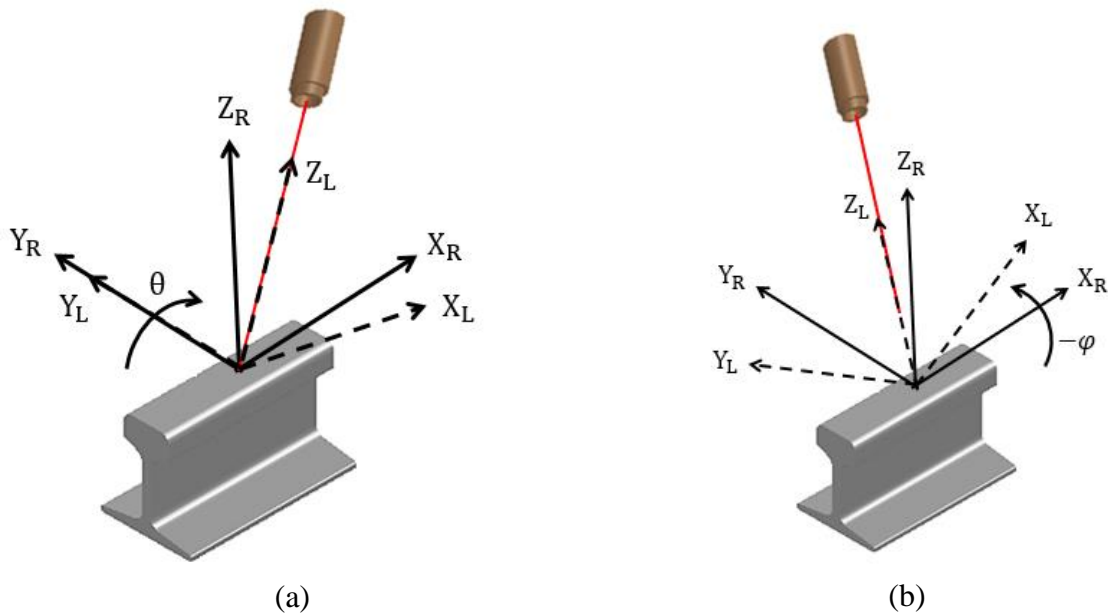


Figure 3-12. LIDAR system coordinate system transformation: (a) rotation of the laser coordinate system about the rail lateral axis to capture forward track speed, (b) rotation of the laser about the rail longitudinal axis to accommodate lens installation and/or capturing lateral track speed.

Since the beam strike direction vector \hat{e} lies in parallel with Z_L , it is found as:

$$\hat{e} = \begin{bmatrix} \cos \theta & 0 & \sin \theta \\ \sin \varphi \sin \theta & \cos \varphi & -\sin \varphi \cos \theta \\ -\cos \varphi \sin \theta & \sin \varphi & \cos \varphi \cos \theta \end{bmatrix} \begin{bmatrix} 0 \\ 0 \\ 1 \end{bmatrix} = \begin{bmatrix} \sin \theta \\ -\sin \varphi \cos \theta \\ \cos \varphi \cos \theta \end{bmatrix} \quad (3-2)$$

The speed detected by the LIDAR (V_m) contains three components of the rail motion (V_x , V_y , and V_z) and is determined by the inner product of the laser beam direction vector and the rail speed vector as:

$$V_m = \begin{bmatrix} V_x \\ V_y \\ V_z \end{bmatrix} \begin{bmatrix} \sin \theta \\ -\sin \varphi \cos \theta \\ \cos \varphi \cos \theta \end{bmatrix} = V_x \sin \theta - V_y \sin \varphi \cos \theta + V_z \cos \varphi \cos \theta \quad (3-3)$$

The equation suggests that the rail motion in different directions has different impacts on the measured velocity by the LIDAR system, depending on the lens orientation and relative magnitude of the speed components. For instance, when the lens is installed with relatively large inclination angles (θ), the forward speed component V_x is the dominant term, while the lateral speed component V_y is dominant when the beam strikes the gage face with a shallow inclination angle.

Chapter 4 Lateral Track Geometry Measurements

The application of Doppler-based, Light Detection and Ranging (LIDAR) technology for calculating the lateral track geometry parameters, including alignment and gage variation, from track speed measurements is investigated in the following chapter. In the proposed embodiment, two low-elevation LIDAR sensors are employed with their beams reflected off the rail gage face on each side. LIDAR lenses are installed with a slight forward angle of 5 degrees to generate velocity signals that contain two components: 1) the left and right track speeds, and 2) any lateral speed caused by track irregularities. A processing technique is developed based on the frequency bandwidth dissimilarities between the vehicle speed and track geometry irregularity to separate the two from each other. The LIDAR system is body-mounted to a geometry inspection car and tests are carried out on revenue service track. The comparison of LIDAR computations with geometry data collected from other established onboard geometry measurement units reveals a close match between the measurements in terms of range and variations. The results indicate that the LIDAR system can provide a reliable non-contact track monitoring instrument for use over substantial track mileage in inclement weather and harsh track conditions with minimal operator supervision.

In the current chapter, the ability of the LIDAR system to detect bi-directional changes in alignment and gage, including curvature and instantaneous angle (i.e. track geometry) will be discussed. If changes in gage and instantaneous angle are assumed to be zero, then alignment is equal to curvature.

It is worth noting that Doppler LIDAR systems are inherently used for measuring velocity, although they may be configured for simultaneously measuring velocity and absolute distance. Likewise, IMUs are essentially instruments that measure acceleration. In the current embodiment of the LIDAR instrument, the system is only configured for measuring velocity, i.e. rate of change of distance. Therefore, it is the spatial variations in gage and elevation that are analyzed and discussed in the following sections. It is the forward velocity of the train that

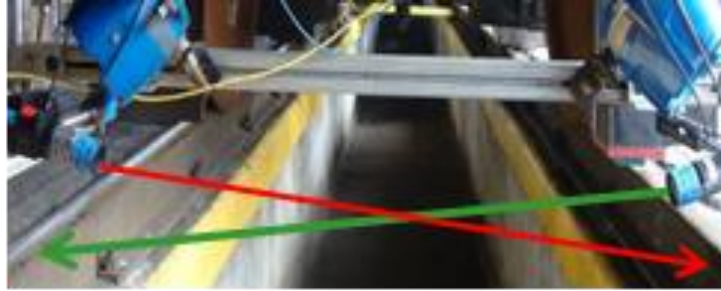
enables such measurements (i.e. a change of gage when the train is moving forward is seen as a lateral velocity by the Doppler LIDAR).

Considering the nature of the IMU (acceleration-based) and LIDAR (velocity-based), IMU is expected to have a higher noise sensitivity than the LIDAR with respect to train body motions and vibrations. On the other hand, LIDAR has higher noise sensitivity to ground-truth variations. This is simply due to the fact that acceleration is the derivative of velocity, and velocity is the derivative of distance. Therefore, variation amplitudes are multiplied by the radian frequency ($\omega = 2\pi f$) for each derivative. This effect can be observed in the data, and analyzed with appropriate filtering of the signal.

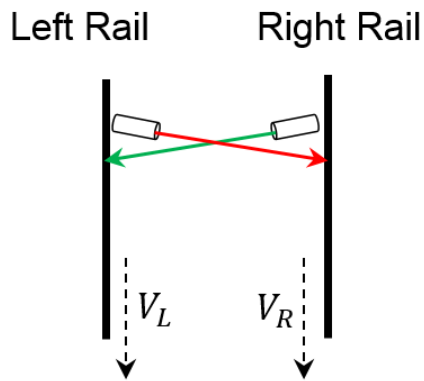
Lateral track geometry is described by alignment and gage. Gage is simply defined as the separation of the rails as measured at the rail gage corner. Track alignment is defined in terms of variations in the lateral positions of the left and right rails from a mean trajectory over a specific length of the track. Positive deviation in alignment denotes a lateral deviation of the track to the left, while negative deviation in alignment corresponds to a lateral deviation of the track to the right. Considering this sign convention, “effective” gage increases with positive results and decreases with negative results.

4.1 LIDAR Sensing and Processing

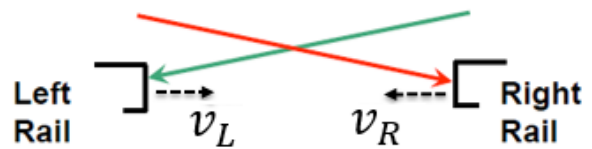
In order to measure the track lateral variations during field testing, a body-mounted LIDAR system is used with a gage face beam configuration, as shown in Figure 4-1 (a). The two low-elevation, slightly tilted LIDAR sensors are nominally pointed at the rail gage face on each track. The LIDAR lenses are installed with a slight forward angle to measure track speed in both longitudinal and lateral directions. The train speed is calculated from the LIDAR left and right forward bias speed measurements; these two velocities are termed V_L and V_R , and are labeled in Figure 4-1 (b). Figure 4-1 (c) shows a front view of the rails, while LIDAR beams detect the left and right rail lateral motions (v_R and v_L). The lateral speed measurements are processed for assessing the track gage and alignment variations. These velocity components and their calculation algorithm are further discussed in the following section.



(a)



(b)



(c)

Figure 4-1. Lateral LIDAR optics used for lateral geometry measurements; (a) beams target the gage face of the rails, (b) left and right track speeds are measured, (c) rates of left and right lateral geometry are observed by the lateral lenses.

4.1.1 Configuration of LIDAR lenses

Doppler sensors measure the velocity in the direction of the laser beam. The sensor is typically mounted in such a way that the laser strikes perpendicular to the moving surface. Therefore, as depicted in Figure 4-2, the ideal LIDAR lens orientation for the lateral track geometry measurements is achieved when the laser strikes perpendicular to the gage face with no elevation. With this orientation, the LIDAR sensor only measures the lateral rail motion, and thus the track forward velocity is not recorded. Additionally, without the forward speed as the offset signal, the direction of the rail lateral motion (gage widening or narrowing) cannot be detected. This orientation was also not possible during field testing onboard the metrology car due to installation limitations.

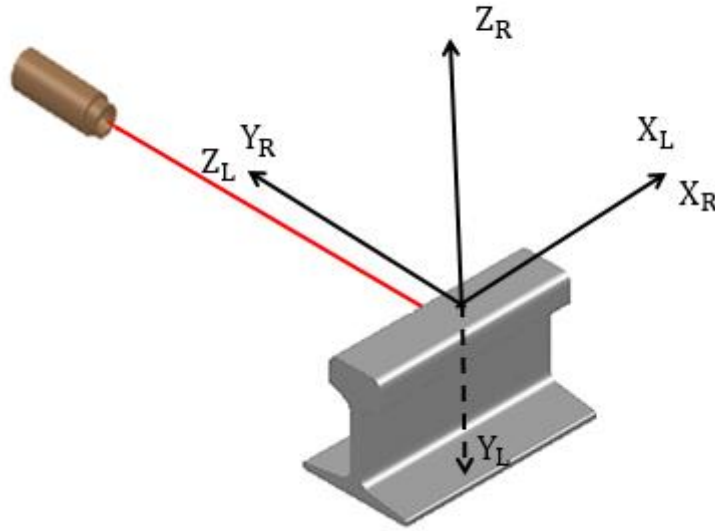


Figure 4-2. The ideal LIDAR lens orientation for lateral track geometry measurements is achieved when the laser strikes perpendicular to the gage face with no elevation. With this orientation, the rail forward velocity is not captured by the LIDAR sensor. This orientation was not possible during field testing due to installation limitations

In the proposed lens embodiment for lateral rail irregularity measurements, the LIDAR sensor is not positioned exactly perpendicular to the gage surface, but the laser strikes the rail face with a bias angle of θ . Also, the lens is not installed at the same height as the gage surface due to mounting limitations, but the laser direction has an inclination angle of φ with the gage face. With this configuration, the sensor's reading has a component of forward driving speed, as well as a component that represents the rail lateral motion. The discussed embodiment is shown in Figure 4-3 for the right side by neglecting the rail vertical motion. In this case, the velocity measured by the right sensor (V_{mR}) is related to the right rail forward velocity (V_R) and right rail lateral deflection velocity (v_R) as:

$$V_{mR} \approx V_R \sin \theta + v_R \cos \varphi \cos \theta \quad (4-1)$$

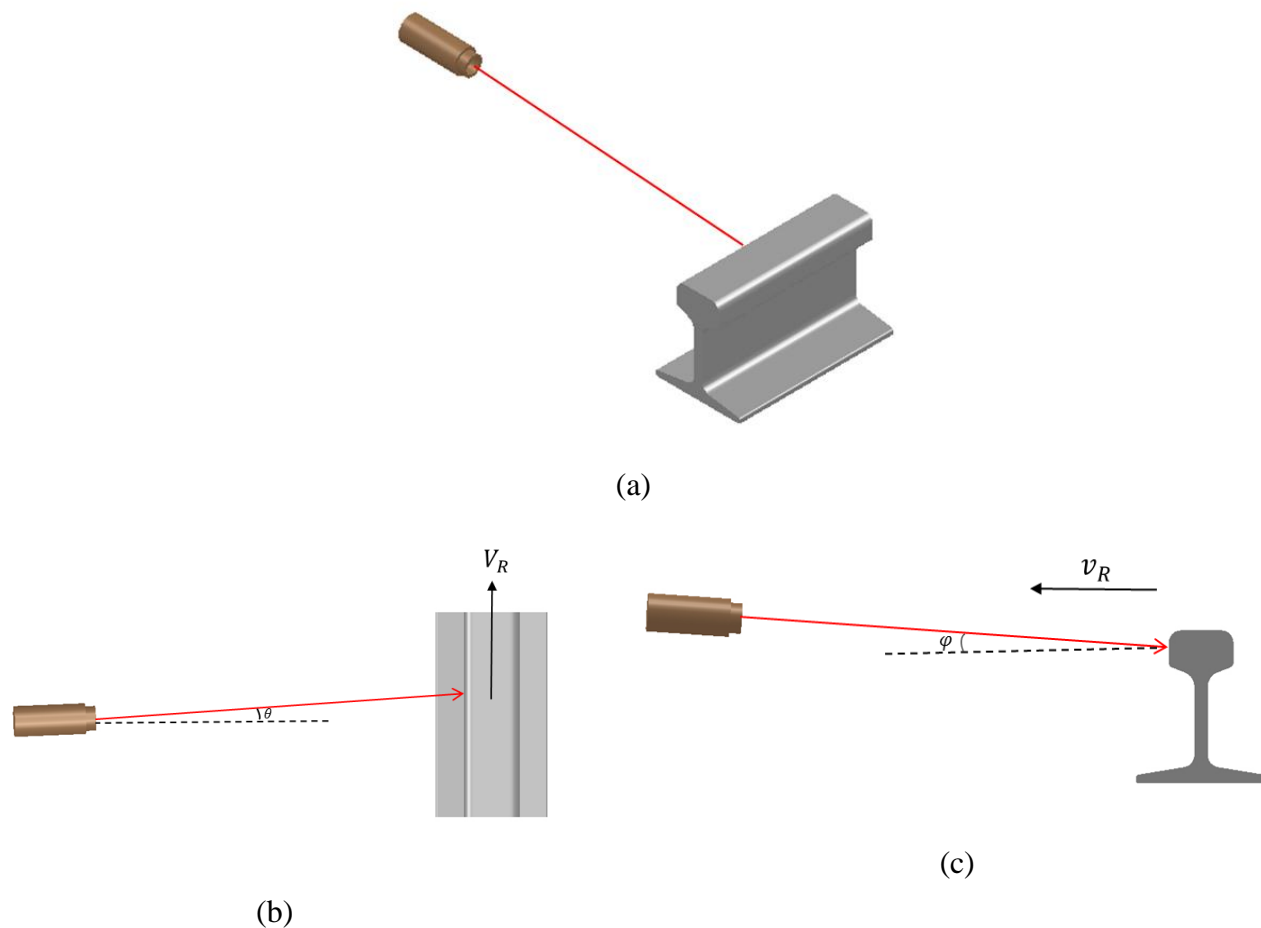


Figure 4-3. The proposed LIDAR lens orientation for lateral track geometry measurements onboard the metrology car; (a) 3-D isometric view of the embodiment for the right rail, (b) top view of the embodiment for the right rail, (c) front view of the LIDAR embodiment for the right rail.

4.1.2 LIDAR data processing technique

Before any meaningful results can be produced from the LIDAR data, it is necessary to determine the exact nature of the data and devise a valid method of analysis. The proposed calculation procedure is illustrated in Figure 4-4. The recorded velocities (V_{mR} and V_{mL}) contain information relating to the vehicle forward speed, distance travelled, and rail lateral displacement, which need to be extracted and manipulated differently. When extracting the forward bias speeds (V_R and V_L), it is necessary to filter the raw data with appropriate Nyquist frequency. This is possible by determining the frequency bandwidth of the driving velocity. Of

course, any information above the cut-off frequency of the low-pass filter (including the rail lateral displacement velocity) will be lost within this process. The average of forward speeds yields the centerline velocity (V_{CL}) that is used to calculate the travelled distance of the train.

The alignment readings for the left and right rails are produced by calculating the lateral displacements of the rails. To extract the rail lateral velocity, the computed forward bias velocity is multiplied by the sine of bias angle ($\sin \theta$) and then subtracted from the raw velocity signal. According to Equation (4-1), vertical inclination of the laser direction should also be compensated by multiplying the resultant velocities by $\cos \varphi$ to obtain the right and left lateral velocities (v_R and v_L). Forward bias velocities are also used to calculate the track curvature that will be later added to the calculated spontaneous alignment deviation to produce the overall alignment for each rail.

In this work, it is proposed that alignment is a function of lateral velocity and curvature that is represented by $(V_R - V_L)$. Thus, left alignment, A_L , is calculated as:

$$A_L = \alpha_L \Delta t v_L + \beta_L (V_R - V_L) \quad (4-2)$$

where α_L is the left lens correction factor, Δt is time increment, and β_L is the track curvature constant for the left alignment. Right alignment, A_R , is similarly computed as:

$$A_R = \alpha_R \Delta t v_R + \beta_R (V_R - V_L) \quad (4-3)$$

where α_R is the right lens correction factor, and β_R determines the effect of track curvature on the right alignment computation. The reason that different curvature constants are considered for the left and right alignments is the slight misalignment of the two laser beams that should be accounted for during the calculation.

Gage variation is assumed to be a function of left and right lateral velocities, as well as forward bias speeds. A linear relation is proposed in this work for the gage variation, Δg , as:

$$\Delta g = \Delta t [\alpha_{Rg} v_R + \alpha_{Lg} v_L] + \beta_g (V_R - V_L) \quad (4-4)$$

where α_{Rg} and α_{Lg} determine the effect of associated lateral velocities on the gage variation. These terms are not identical if the laser beams are not perfectly aligned. The track curvature is taken into account in Equation (4-3) with a constant parameter β_g . The values of the introduced parameters are listed in Table 4-1.

Table 4-1-Numerical values used in the processing of LIDAR data for calculation of lateral track geometry parameters

SYMBOL	PARAMETER	VALUE
θ	lens bias angle	5 degrees
φ	lens inclination angle	11 degrees
α_L	left alignment correction factor	1.1
α_R	right alignment correction factor	1.3
β_L	track curvature correction factor for the left alignment	1.58
β_R	track curvature correction factor for the right alignment	1.51
α_{Rg}	effective right lens correction factor for the gage variation	0.22
α_{Lg}	effective left lens correction factor for the gage variation	-0.26
β_g	track curvature correction factor for the gage variation	0.23
-	forward cut-off frequency	0.2 Hz

4.2 Experimental Results and Evaluation

Data was taken for a round-trip between Roanoke and Lynchburg, VA (about 50 miles one way). Encoder speed data, onboard inertial measurement unit (IMU) data, and gage sensor data were also collected as asynchronous parallel data files. Speed/velocity and track geometry results are presented below for 7.2 miles of track, which included multiple sections of tangent and curved tracks traveled in an eastbound direction. The research car was traveling from Roanoke to Lynchburg (eastbound) on this section through mile-posts N221 to N214.

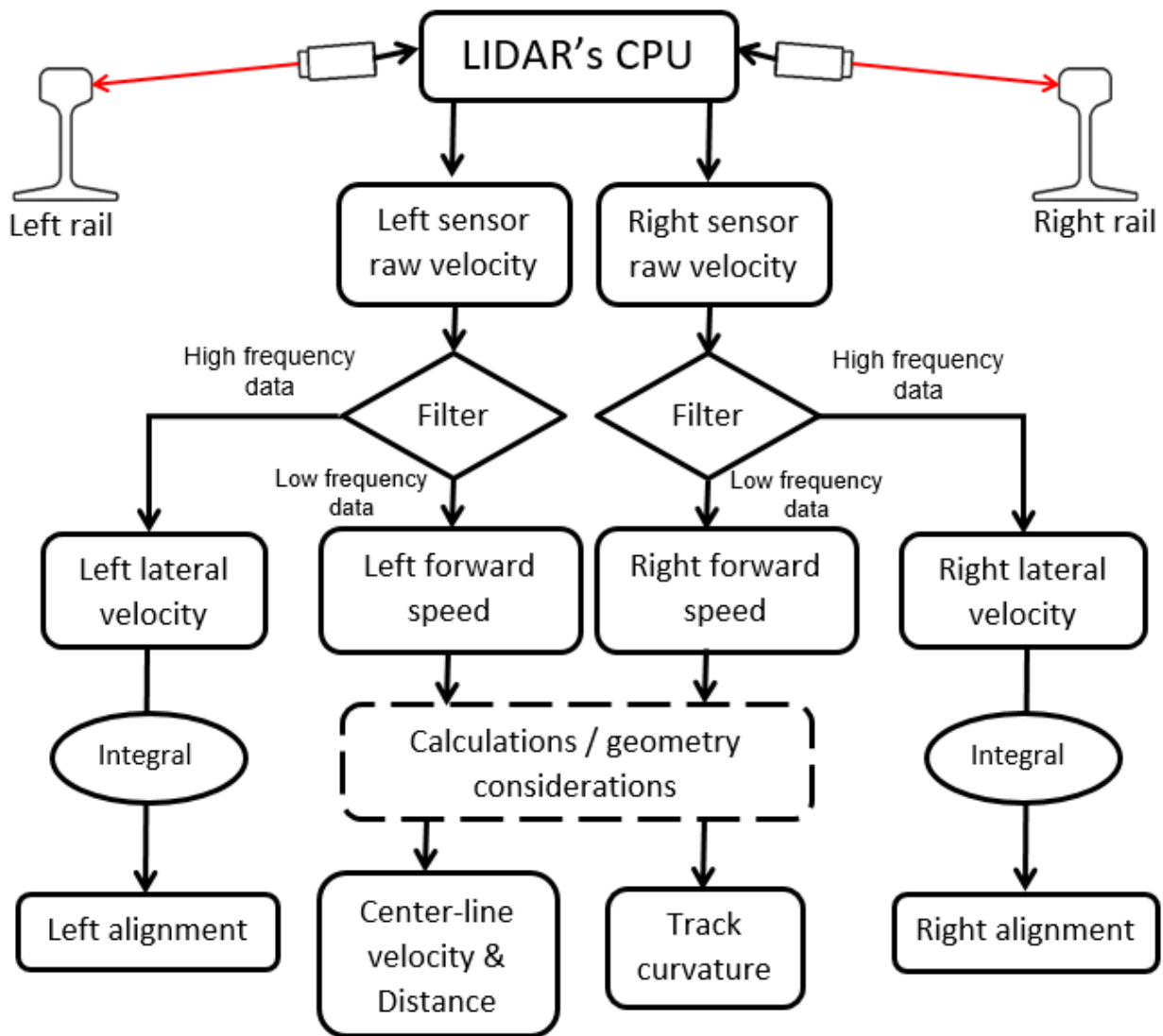


Figure 4-4. Post-processing algorithm implemented to derive train speed, track curvature, and lateral track irregularities using LIDAR measurements.

4.2.1 Time domain analysis

LIDAR system is a real time measurement unit and all calculations are initially conducted in the time domain. As discussed earlier, the first step in alignment and gage calculation is to extract the left and right forward speeds (V_L and V_R). These speeds are plotted versus time in Figure 4-5

for the selected test run. Since these vectors represent the left and right wheels' forward velocities, they are expected to be identical in tangent tracks, and different in curves.

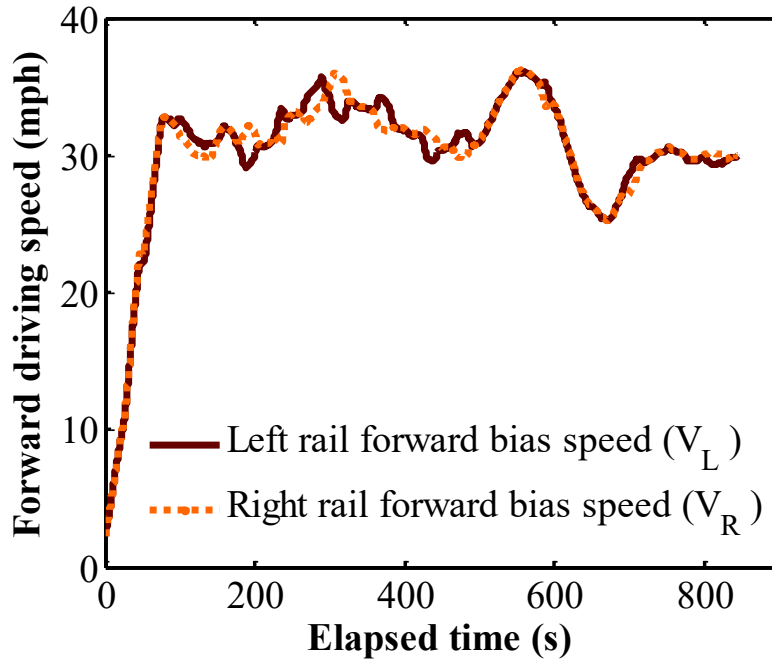


Figure 4-5. LIDAR left and right forward bias speeds in time domain.

The average of left and right forward bias velocities is taken as the centerline speed (V_{cl}) and is compared against wheel-mounted encoder measurements in Figure 4-6. There is a high correlation between LIDAR and encoder speed outputs, which strongly supports extracting lateral variations due to lateral motion/spatial deviations from the bias of the forward speed signals. Net deviation between the LIDAR and the wheel encoder is less than $\pm 0.9\%$ at an average speed of 34mph, with the encoder typically undershooting or overshooting the more stable LIDAR signal due to mechanical/wheel-rail effects.

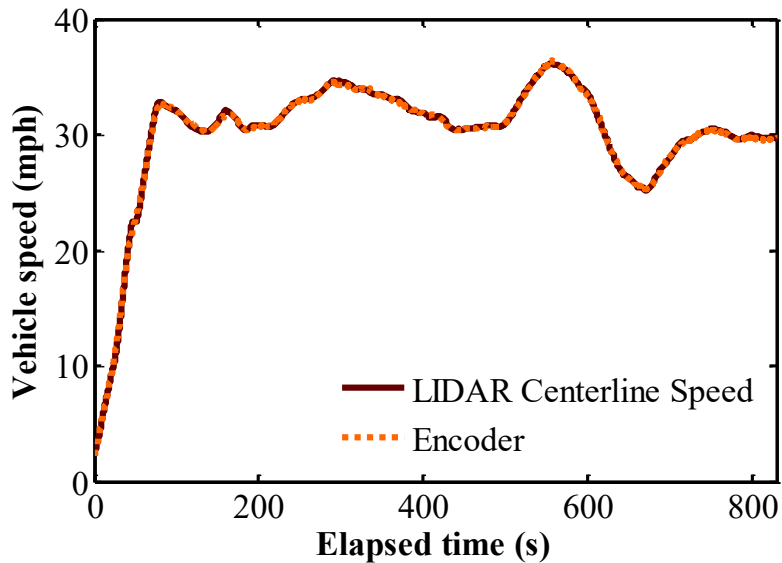


Figure 4-6. LIDAR centerline speed in comparison with encoder reading.

The key step in the proposed calculation procedure is finding the lateral displacement. The calculated lateral velocities are plotted in Figure 4-7 for 20 seconds of travel. It is worth noticing that signed vectors resulted for the lateral velocities due to the forward bias angle in the beams. Signed values allow us to assess whether the gage is narrowing or extending.

The periodicity of the signals plotted in Figure 4-7 indicates lateral deviations at spatial frequencies between 70ft and 200ft, which is reasonable for the track environment. The standard deviation is around 0.83in for the lateral deviations along approximately 1000 ft. This is again not unreasonable, considering that some portion of the variation is also due to alignment variation in the single curve of this analysis zone.

4.2.2 Spatial domain analysis

After processing the LIDAR data in time domain as described in the previous section, the data was re-evaluated in the spatial domain to allow for the comparison between the LIDAR system and other measurement units, including encoder, IMU, and onboard gage sensor. These instruments sample the data spatially at a rate of 1 or 2 samples per foot. Given the nominal speed over a specific length of track, the resampling frequency for the LIDAR data is determined.

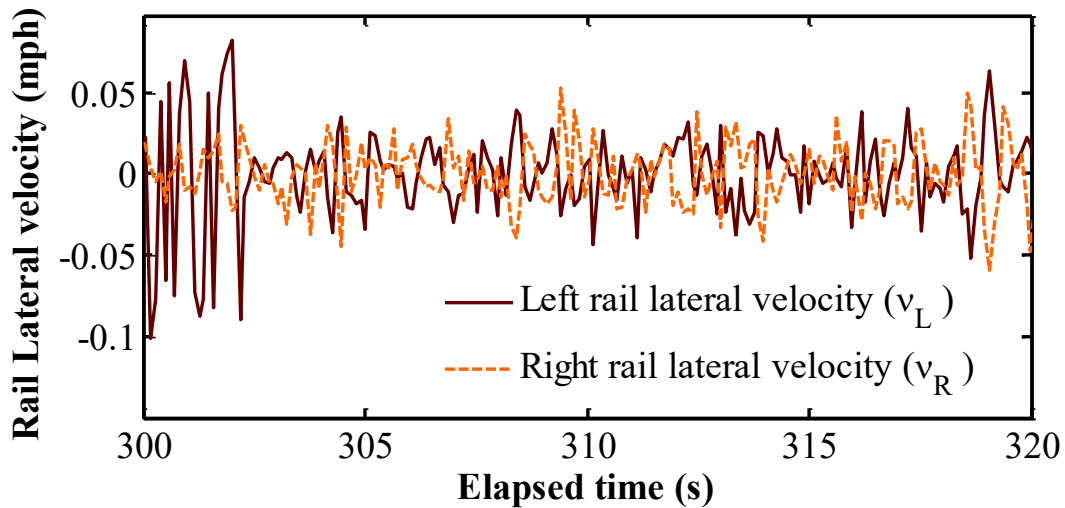


Figure 4-7. Computed left and right lateral velocities for 20 seconds of travel.

LIDAR left alignment calculated from the lateral velocity data is compared to onboard IMU readings in Figure 4-8. This figure shows a good overall agreement between the LIDAR and IMU measurements. As expected, large changes are observed in the alignment readings in curves. Separating out and analyzing the curvature responses in Figure 4-8 leads to the conclusion that for this shallow forward bias angle condition, the curvature response difference between the LIDAR and the IMU is simply a constant linear scale factor for both positive and negative curvature, i.e. the IMU measured curvature response is 7% less than that measured by the LIDAR. Previous ground-truth measurements indicated that IMU has an average error relative to the ground-truth curvature of -8.95% with a standard deviation of 3.29%. This implies that the LIDAR in this beam condition is in fact more accurate than the IMU, and has an error on the order of 1.95%. Additionally, the peak curvatures in Figure 4-8 are consistent with the track chart readings over the stretch of track surveyed.

The local alignment variations that are caused by lateral velocity ($\Delta t v_L$), not the curvature, for the specified right and left curves are compared in Figure 4-9 and Figure 4-10. IMU curvature reading is also overlaid for each curve in those figures, and is scaled to fit within the spatial reference of the graph. LIDAR signal magnitudes compare closely with IMU magnitudes in measuring the range and variation trend of the rail deviations. However, a perfect correlation is not achieved since the two measuring systems use different sensing mechanisms and have different temporal bandwidths. Additionally, exact spatial correlation cannot be established since

the measurements are made asynchronously despite the reasonable overlay achieved for the graphs. Such asynchronicity leads to some apparent random phase motion between the signals that is not really present in the data. In Figure 4-9 and Figure 4-10, positive increases are outward deviations of the rail or increasing angle and gage. In both figures, there is a slightly positive “offset” to the LIDAR signal that, in reality, is the LIDAR measuring the long, slow right-hand curvature of the total track path. Even at the track speed of 34mph, the IMU does not react to this low level of curvature, while the LIDAR does.

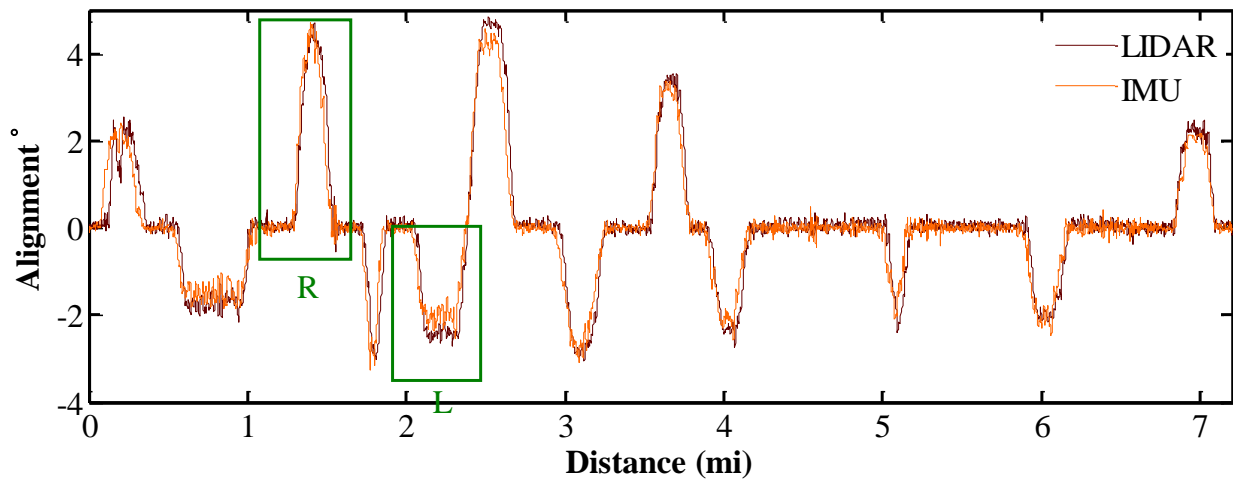


Figure 4-8. Left rail alignment profile measured by the LIDAR system and IMU, showing good correlation on a larger scale. The boxed sections are examined more closely in the following figures.

Right alignment is also studied, and the results are shown in Figure 4-11. The data yields similar conclusions and statistics as developed for the left alignment measurements. The boxed sections of Figure 4-11 are examined closely in Figure 4-12 and Figure 4-13 to complete the left-right curves data set. In particular, the difference between IMU measured curvature and LIDAR measured curvature in Figure 4-11 is a fixed gain factor (1.08), implying a nearly linear relationship between the two sensors. This affirms the fact that the LIDAR accurately measures curvature if the beam angles do not engage the rail curvature in the non-linear large angle regime. The results indicate that LIDAR is at least as good as the IMU at measuring curvature and alignment when the beam angles are configured properly.

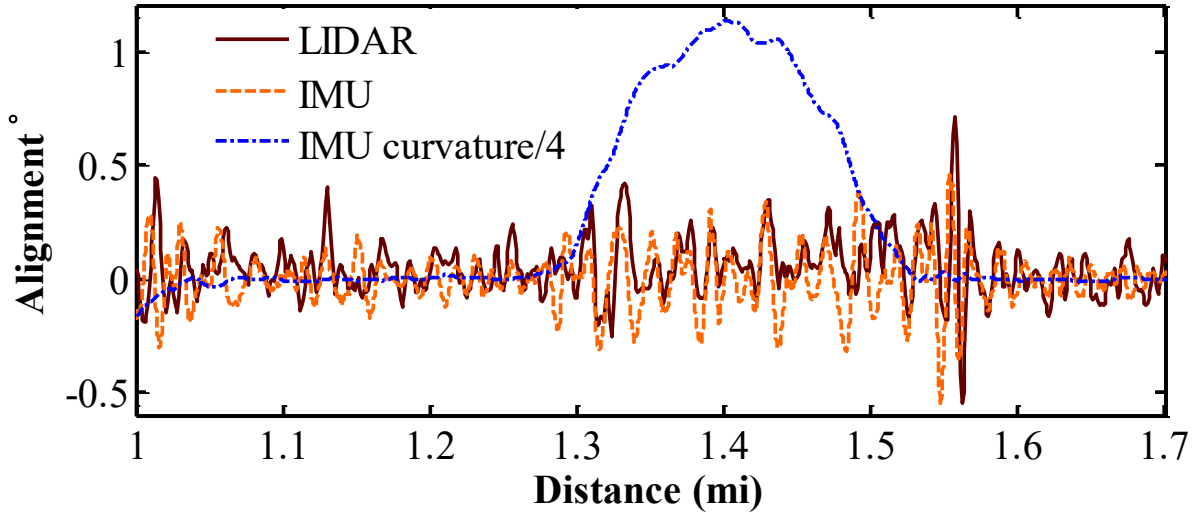


Figure 4-9. A closer look at the left rail alignment deviations before, along, and after the right-hand curve boxed in Figure 4-8. The variation profiles do not show high correlation, however, the magnitudes of the variations are similar, signifying a detection of variation by the LIDAR system.

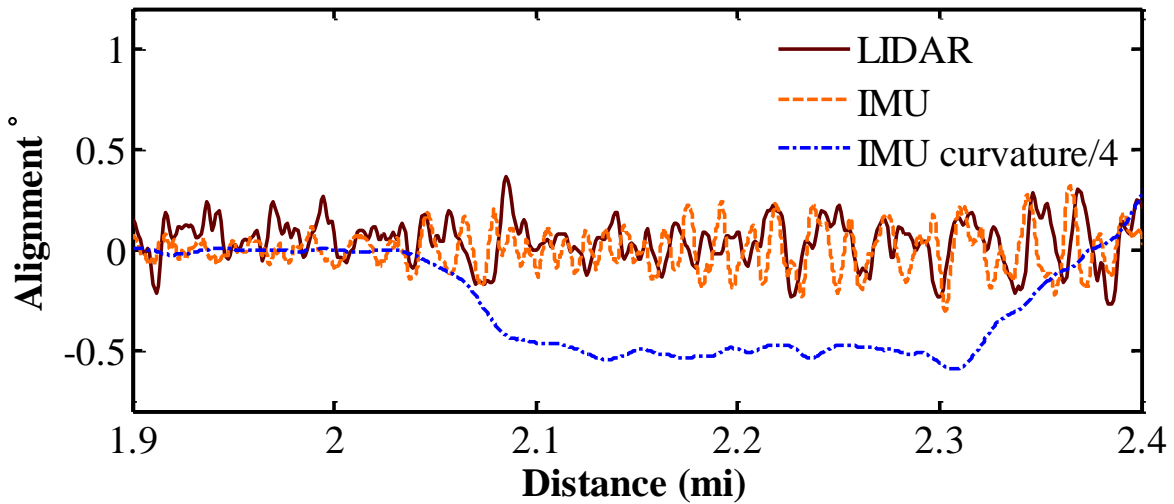


Figure 4-10. Left rail alignment deviations along the boxed left-hand curve in Figure 4-8. Similar to the profile along the right-hand curve, the magnitude of alignment deviations matches closely with that of the IMU's detection of alignment.

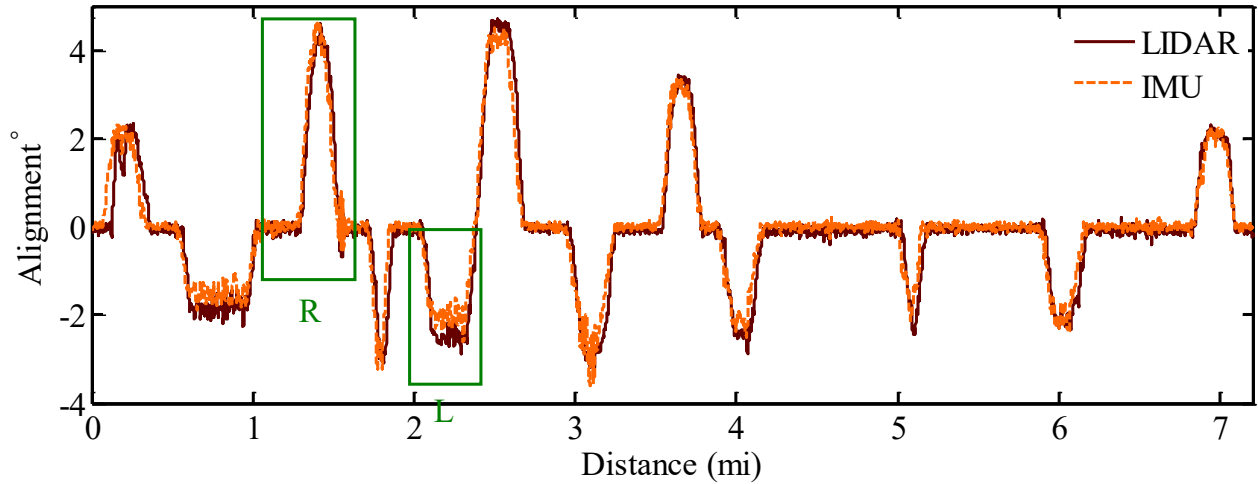


Figure 4-11. Right rail alignment profile measured by the LIDAR system and IMU, showing good correlation on a larger scale.

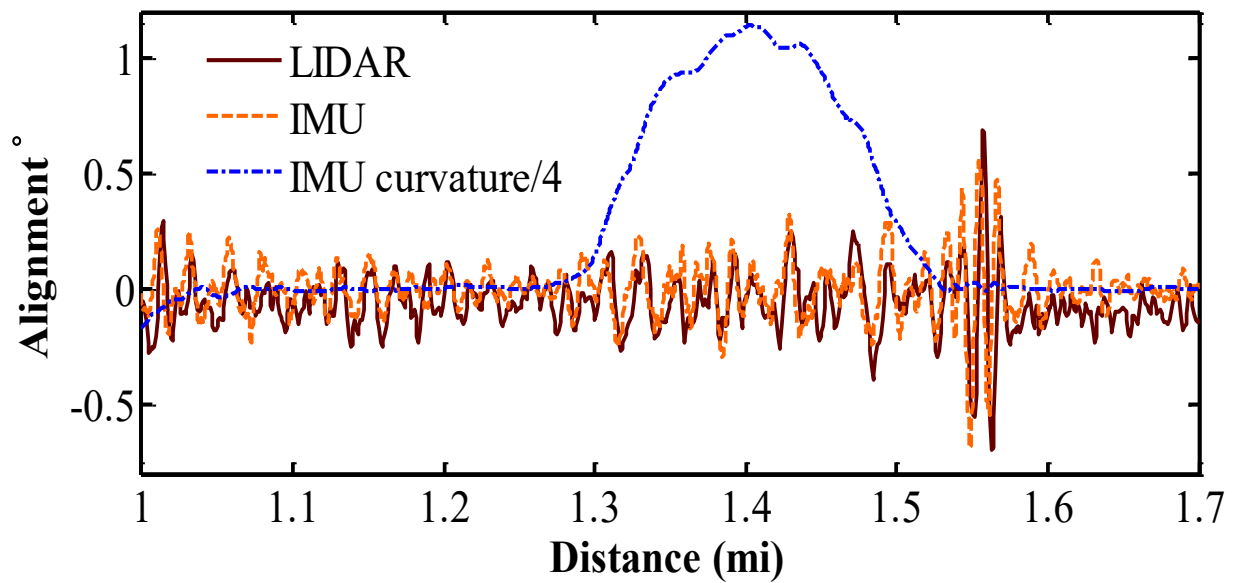


Figure 4-12. A close-up view of the right rail alignment along the right-hand curve boxed in Figure 4-11. The same observations made for the left rail apply to the right rail. Some correlation is found between the LIDAR and IMU signals, however, the magnitude of alignment variation is the primary similarity between the two.

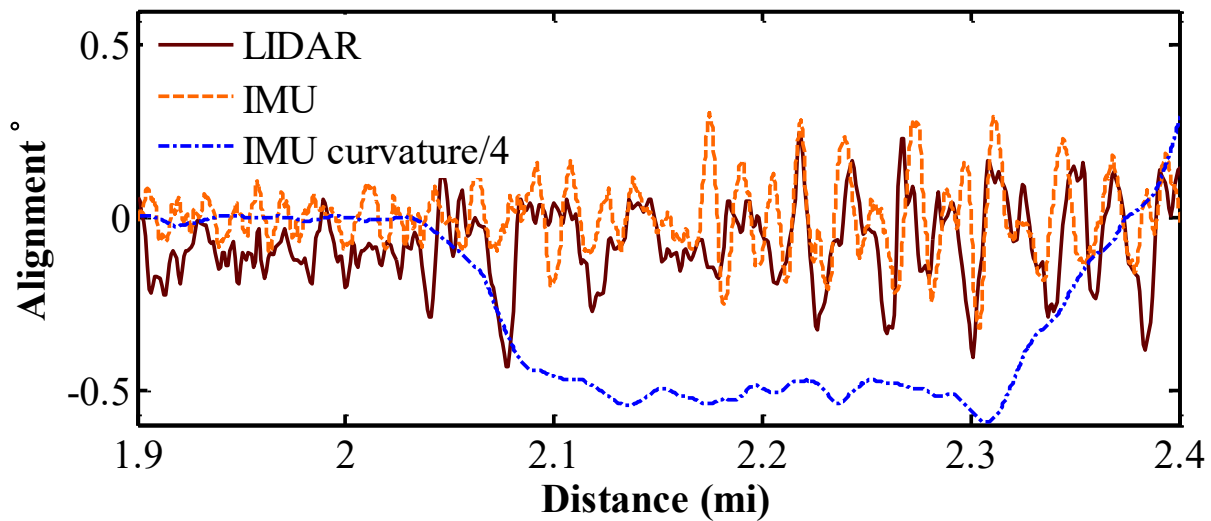


Figure 4-13. Right rail alignment variation profile along the left-hand curve boxed in Figure 4-11.

LIDAR gage variation measurement is compared to an onboard gage sensor reading in Figure 4-14. Although LIDAR predicts a similar trend, there is a clear deviation between the two measurements that is believed to stem from asynchronous measuring techniques. This deviation, however, is mostly observed in the curved sections, where the curvature factor is applied in the calculations. The local gage variations when the curvature effect is filtered out, for the specified right and left curves, are compared in Figure 4-15 and Figure 4-16. These plots show how closely LIDAR matches with the gage sensor in measuring the range and variation trend of gage. If the curvature effects in Figure 4-14 are removed with further processing and filtering, as in Figure 4-15 and Figure 4-16, the LIDAR data can be more completely analyzed for gage variation. The local gage variations that result when the curvature effect is filtered out are compared in Figure 4-15 and Figure 4-16 before and during right-hand and left-hand curves, respectively. These plots easily show how closely the LIDAR-measured gage variance matches with the results from the gage sensor in measuring the range and variation trend of gage.

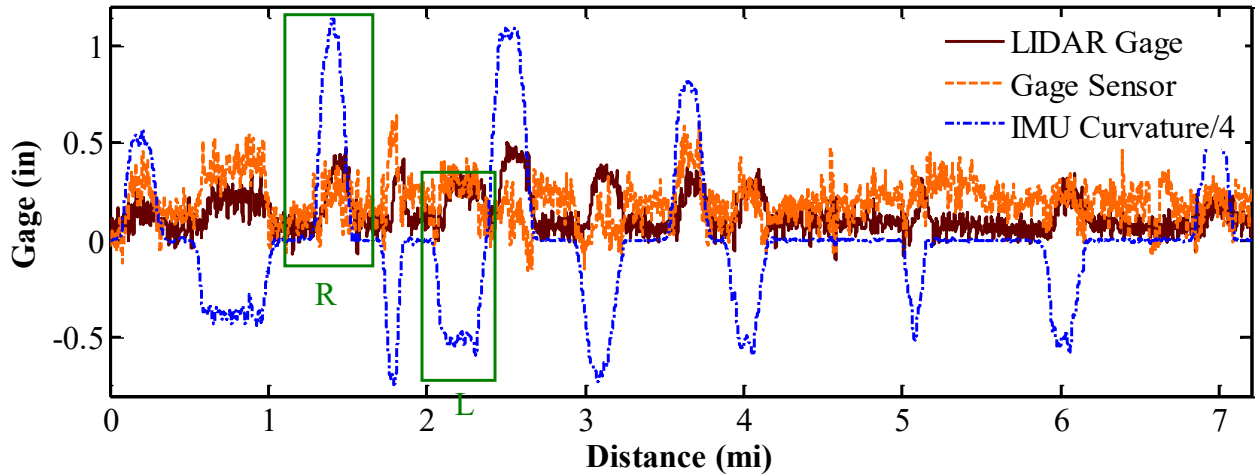


Figure 4-14. LIDAR gage calculation compared with the gage sensor onboard the geometry car without curvature subtraction and appropriate filtering.

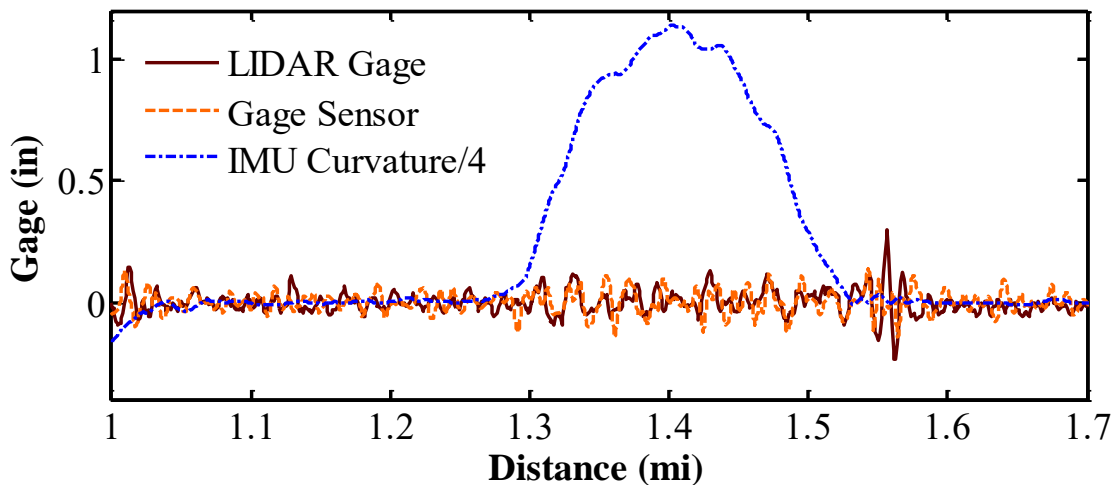


Figure 4-15. Gage variation measured by the LIDAR system and gage sensor onboard the geometry car in the boxed right-hand curve of Figure 4-14. The primary correlation lies in the magnitude of gage change detected along both the curved and tangent sections.

The gage measurement results indicate that with the appropriate filtering, both the LIDAR and the gage sensor report standard deviations of 0.08 inches of gage variance over the track distance surveyed. For the LIDAR to provide useful measurements over longer track distances, processing algorithms need to be developed to periodically reset gage offsets that develop from mathematical integration processing artifacts. The scale factor difference between the two sensors is minimal when absolute gage offsets are taken into account for the gage sensor. Again, it is worth noting that LIDAR does not measure absolute gage, but rather gage deviation.

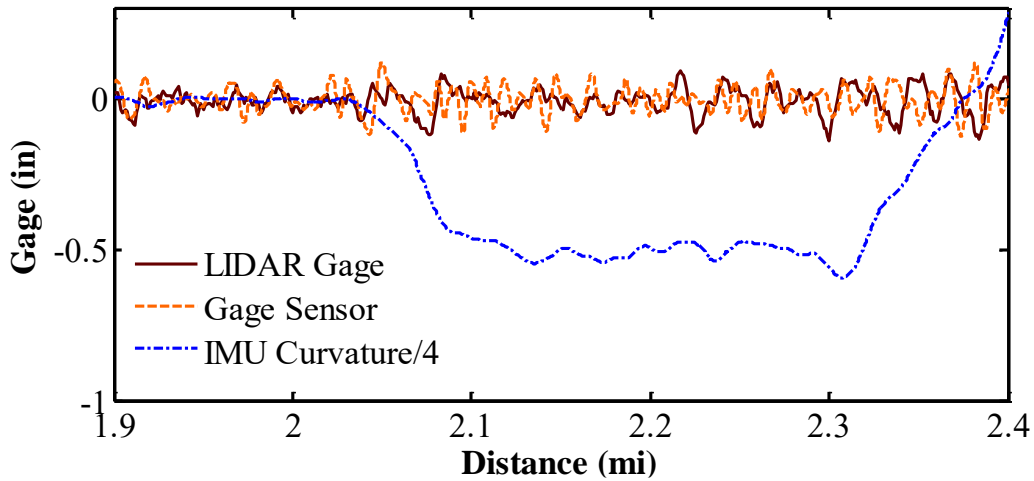


Figure 4-16. Gage variation detected along the boxed left-hand curve of Figure 4-14.

4.3 Statistical Probability Distributions: Evaluation of Alignment and Gage

Spatially-based visual and graphical analysis of alignment and gage data showed reasonable overall correlation between LIDAR and other measurement sensors in the previous section. Agreement in magnitude was sufficient to show the capability of the LIDAR systems to make useful measurements of the magnitude variations in those parameters. However, no absolute, comprehensive spatial or temporal phase correlation was observed, principally due to the asynchronous nature of the measurements, spatial separation of the compared sensors onboard the train, and differences in fundamental instrument characteristics. The phase correlation in data, such as presented in Figure 4-14 through Figure 4-16, is quantitatively partial, though suggestive of high correlations, and is source-dependent (e.g. body vs rail motions). Phase information is particularly affected by instrument location, response bandwidth, asynchronous data collection, and unfiltered, coupled vibration/body motions. Further magnitude analysis is carried out by using probability distributions of the data. Such an analysis can produce and evaluate assessments of sensor agreement in the magnitude domain on a statistical basis.

Probability distributions are defined for intervals, not single points. For a continuous function, the probability density function (PDF) is the probability that the variant takes the value x . PDF is expressed in terms of an integral between the interval $[a, b]$ as

$$P(a \leq x \leq b) = \int_a^b f(x)dx \quad (4-5)$$

Cumulative distribution function (CDF) is another useful distribution tool. CDF is the probability that the variable takes a value less than or equal to x . CDF is also expressed in terms of integral as:

$$CDF(x) = \int_{-\infty}^x f(t)dt \quad (4-6)$$

PDFs of LIDAR and IMU left alignment, along with the associated CDFs, are shown in Figure 4-17 using data from Figure 4-8. These graphs show good agreement between the two measuring units in terms of parametric magnitudes. If the two sensors are not measuring the same parameters with a similar sensitivity and signal-to-noise ratio, the magnitude probability statistics would be radically different in peak amplitude, width, and spectral distribution (cumulative density, CDF). The same comparison is also made for the right alignment, as shown in Figure 4-18 using data from Figure 4-11. Probability and cumulative density functions are also computed for the local gage variation data made using the LIDAR and the onboard gage sensor, as shown in Figure 4-19. The data sources for these graphics are from Figure 4-14. It should be noted that the curvature parameter is automatically eliminated by the mathematics when calculating the local gage statistical variations studied in these plots in this manner.

For the range of measurements obtained by the LIDAR system and the onboard IMU and gage sensor, we further extend the analysis by calculating the 95th percentiles of the data sets and plotting the results in Figure 4-20. For the left alignment, 95% of LIDAR and IMU data magnitudes fall equally below 3.11 and 3.28 degrees, respectively. For the 95th percentiles of the right alignment, the analogous results are 3.10 and 3.16 degrees. For LIDAR gage and gage sensor variation data, 95% of the magnitudes fall below 0.40 in and 0.35 in, respectively. In synopsis, the probability distributions for the various sensors are similar enough to conclude that they represent identical functional capabilities.

In conclusion, what this form of analysis shows is that the LIDAR data, taken at appropriate beam angles and properly filtered/offset/scaled, can be used to determine the magnitudes of rail alignment and gage variations. Further, given the spatial/temporal alignments of prior sections, the LIDAR will also properly reproduce the temporal and spatial data necessary to locate rail geometric variations on the rail itself.

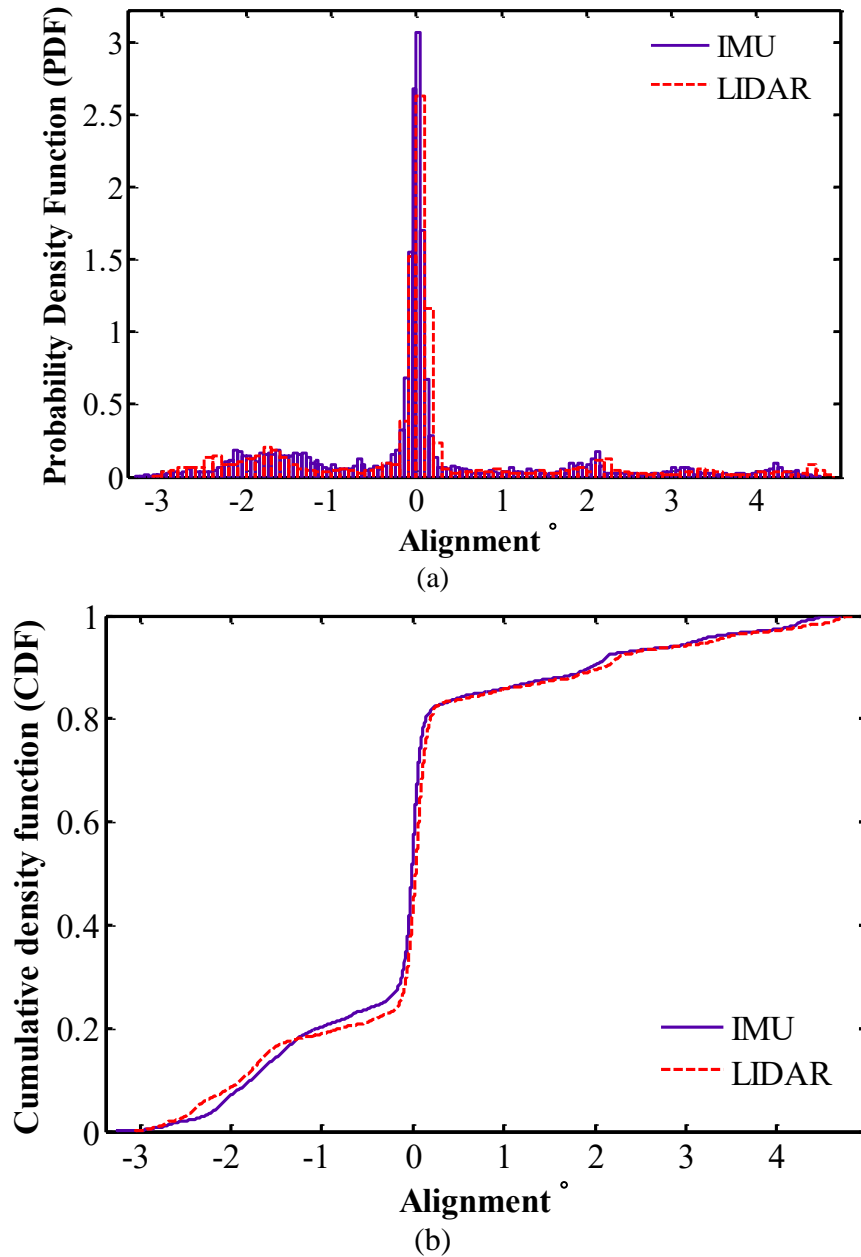
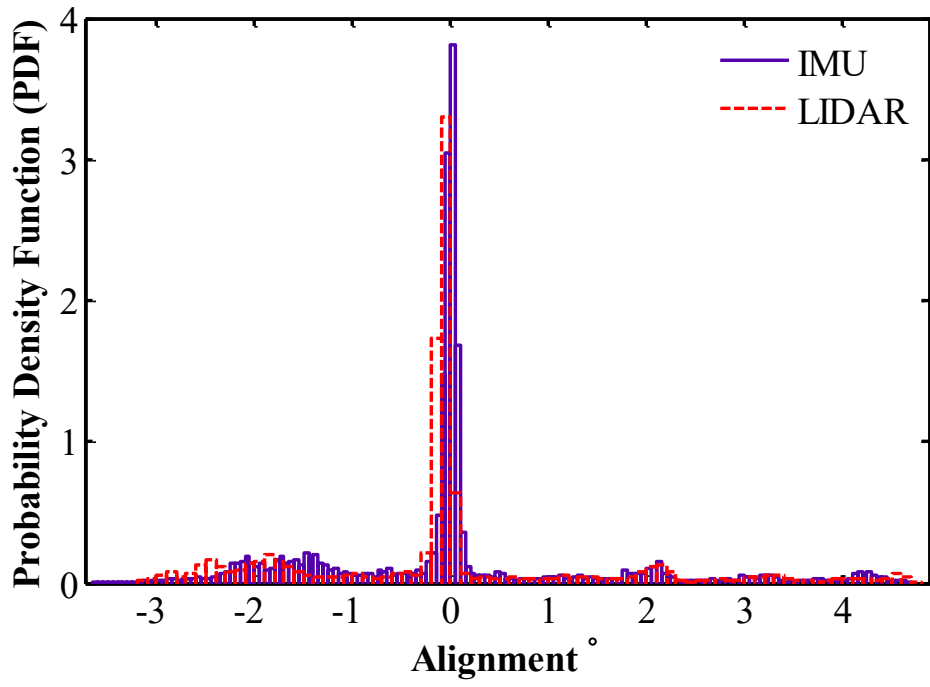
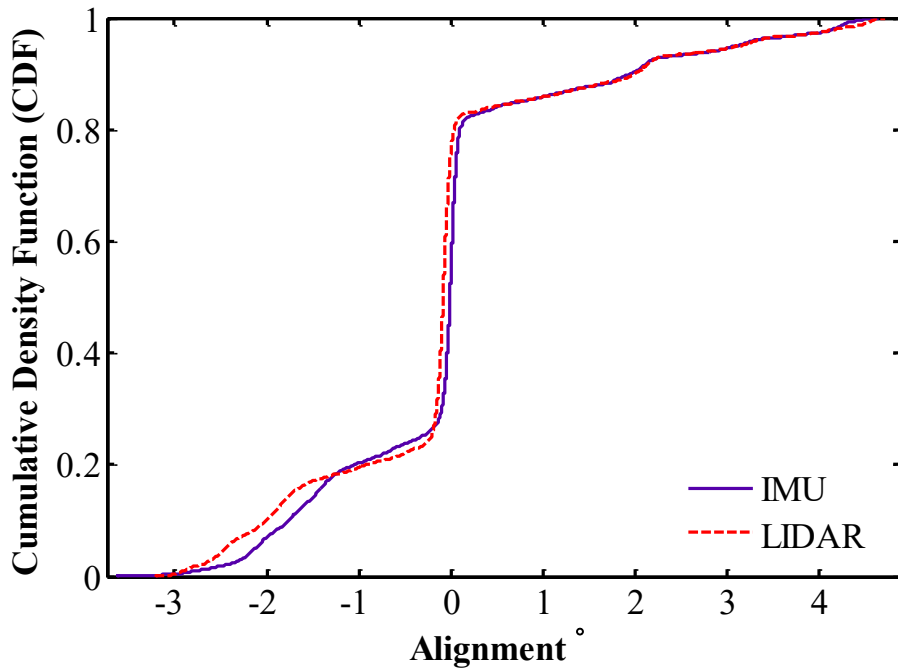


Figure 4-17. Probability distributions of LIDAR and IMU left alignment measurements; (a) left alignment probability density function (PDF), (b) left alignment cumulative density function (CDF).

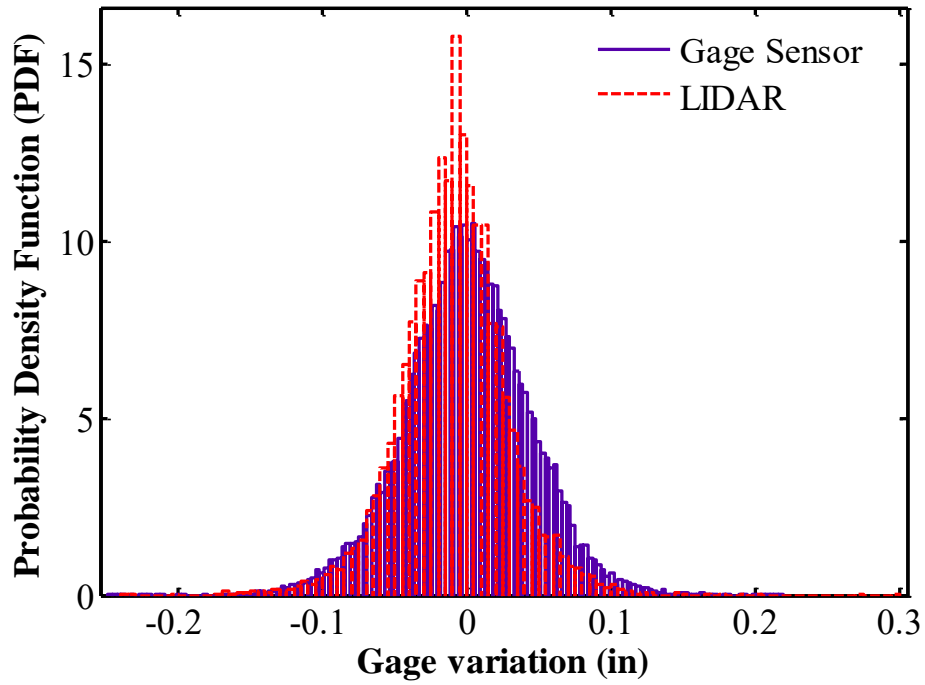


(a)

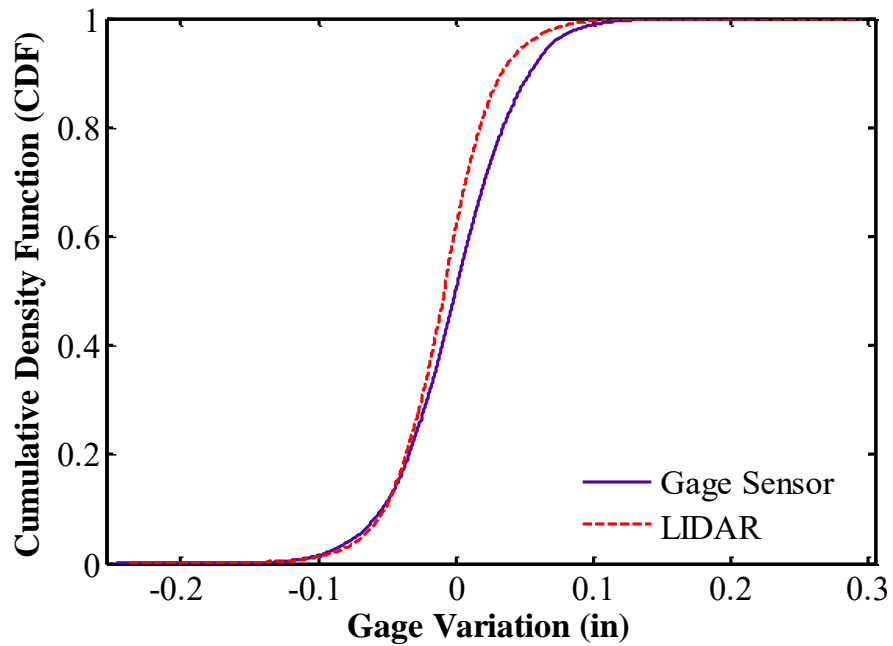


(b)

Figure 4-18. Probability distributions of LIDAR and IMU right alignment measurements; (a) right alignment probability density function (PDF), (b) right alignment cumulative density function (CDF).



(a)



(b)

Figure 4-19. Probability distributions of LIDAR and onboard gage sensor measurements; (a) local gage variation probability density function (PDF), (b) local gage variation cumulative density function (CDF).

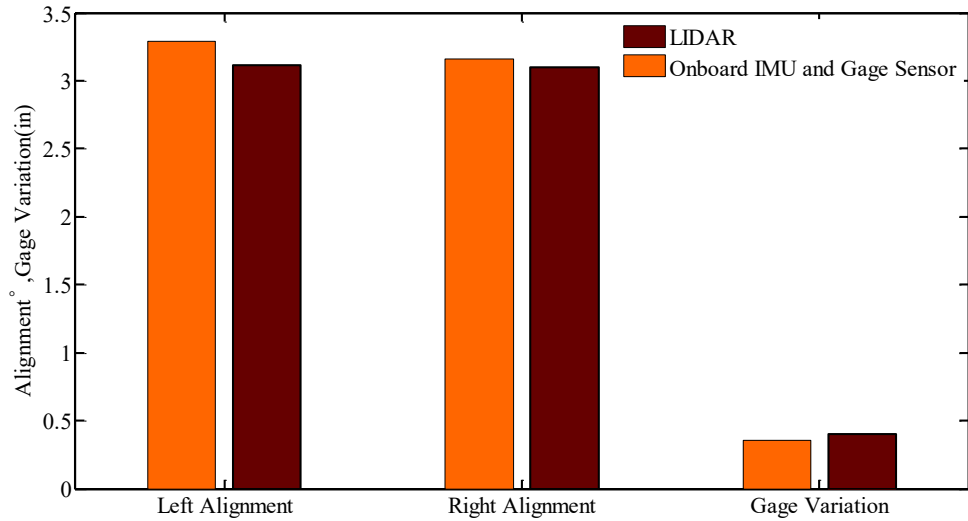


Figure 4-20. 95th percentile amplitude distribution for gage and alignment measurements.

4.4 Universality of Track Geometry Measurements

As mentioned earlier, all the analyses presented in the previous sections (4.2-4.3) are extracted for 7.2 miles of the track from mile-posts N221 to N214 (train heading east). To investigate the universality of the calculation algorithms and the accuracy of the calibrated parameters, measurements and the analysis are repeated for another set of data over 5 miles of travel distance. While it is statistically necessary to repeat the analysis more than twice to accurately assess repeatability, twice was the only opportunity afforded by the analytical portion of the program schedule. However, if the results are statistically the same or similar to those in the prior section, it is reasonable to assume that the results are repeatable using only two assessments. This makes the comparison worthwhile for inclusion in the report. For this analysis, the train was traveling from Lynchburg to Roanoke (westbound) on the selected section of track between mile-posts N217 and N222. This places the orientation of the LIDAR beams such that the sign of the Doppler effect is now subtractive from the optical carrier instead of additive, thereby reversing temporal lead/lag effects between the LIDAR and IMU. However, the results are visually similar to those of the orientation in the prior

sections, except in the curve at 4.25 miles in Figures 62 and 64. In this curve, the speed of the train is below the accuracy threshold of the IMU, causing the sensitivity of the IMU to be reduced and therefore inaccurate. Numerically, the data yields the same quantitative results found in the prior section within a factor of two or so.

LIDAR left alignment is compared against the onboard IMU measurement in Figure 4-21. The local left alignment variations for the specified right and left curves are compared in Figure 4-22. Similar comparisons are made for the right alignment measurements, and the results are depicted in Figure 4-23 and Figure 4-24. It can be concluded again that the LIDAR measurement correlates with IMU data in measuring the range and trend of alignment variation, but an exact spatial correlation is again not achieved due to different measuring techniques, asynchronous acquisition, and displaced sensor locations. In any case, the sensing results are shown to be statistically repeatable.

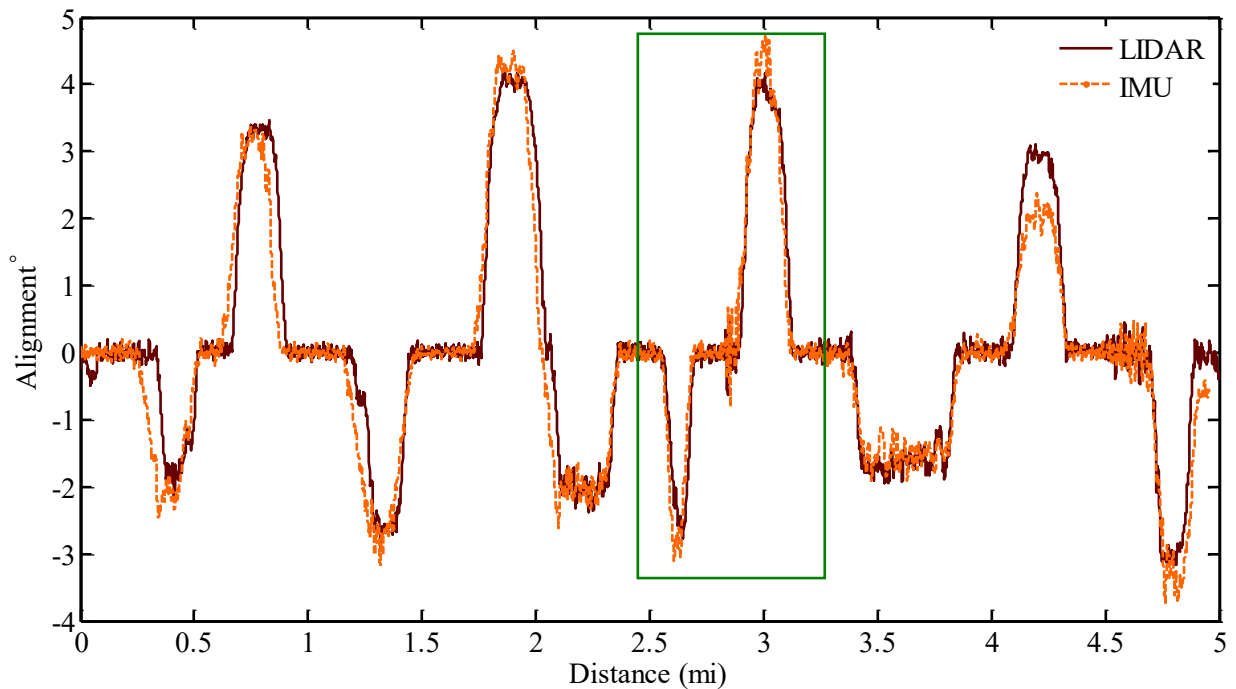


Figure 4-21. Left rail alignment comparison between LIDAR and IMU measurements in the spatial domain.

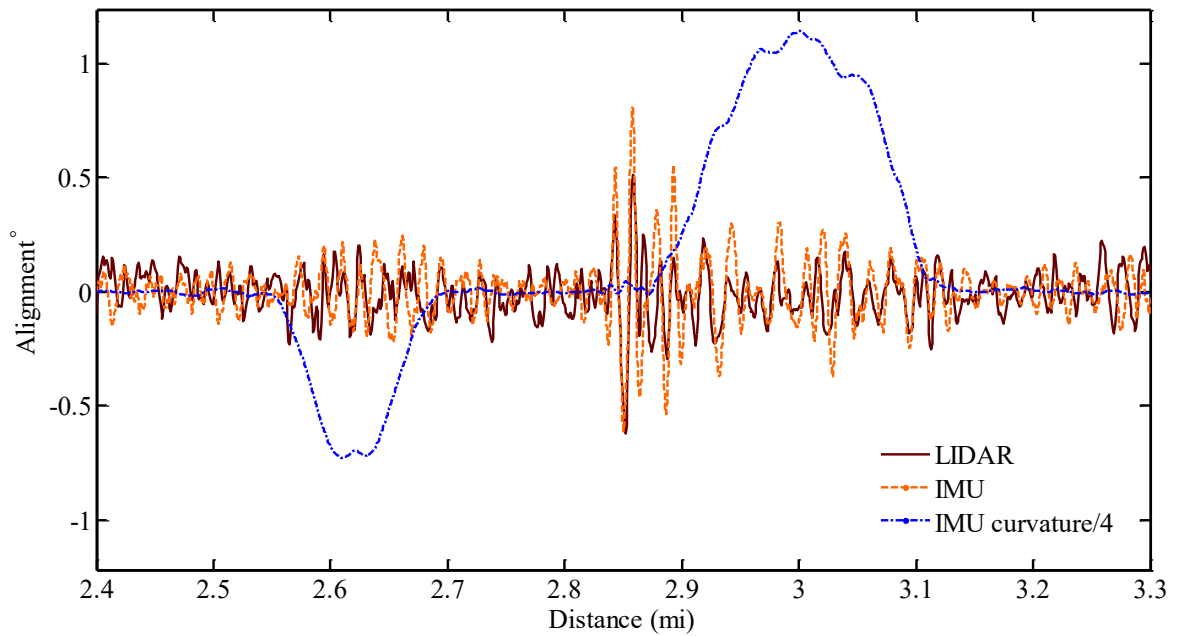


Figure 4-22. Variation of left rail alignment from the boxed section in Figure 4-21.

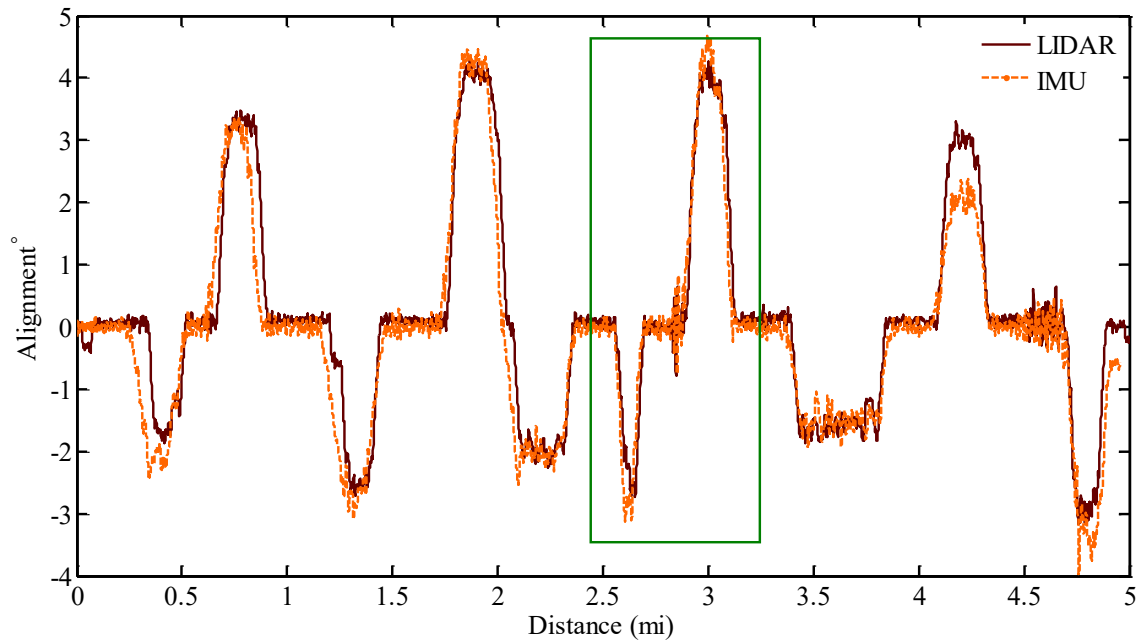


Figure 4-23. Right rail alignment comparison between LIDAR and IMU measurements in the spatial domain.

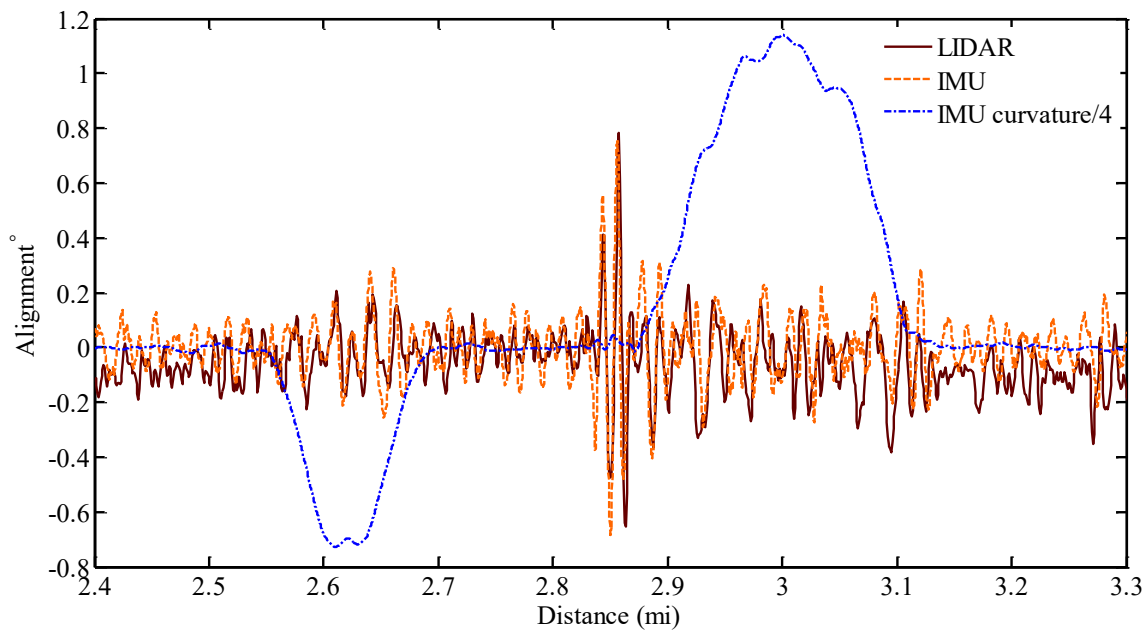


Figure 4-24. Variation of right rail alignment from the boxed section in Figure 4-23.

Gage variation data for the LIDAR and the onboard gage sensor are compared in Figure 4-25 for this series of tests. As discussed earlier, there is a significant absolute difference between the two measurements in curves. However, the LIDAR again closely matches the gage sensor in measuring the local gage variations (i.e. instantaneous variation), as shown in Figure 4-25. In Figure 4-26, at a location between 2.8 and 2.9 miles, the LIDAR sensor responds to a vehicle “slap” impulse response that the other sensors did not detect. This response is to a rail alignment transient impulse that excites the suspension or car linkages and produces a classic damped oscillatory response. Such transients can be the immediate result of alignment transients or can be the response to rail defects including breakage, galling, loose plates, etc. In any case, it is worth noting that the LIDAR possesses detection capabilities that the gage and IMU sensor do not possess.

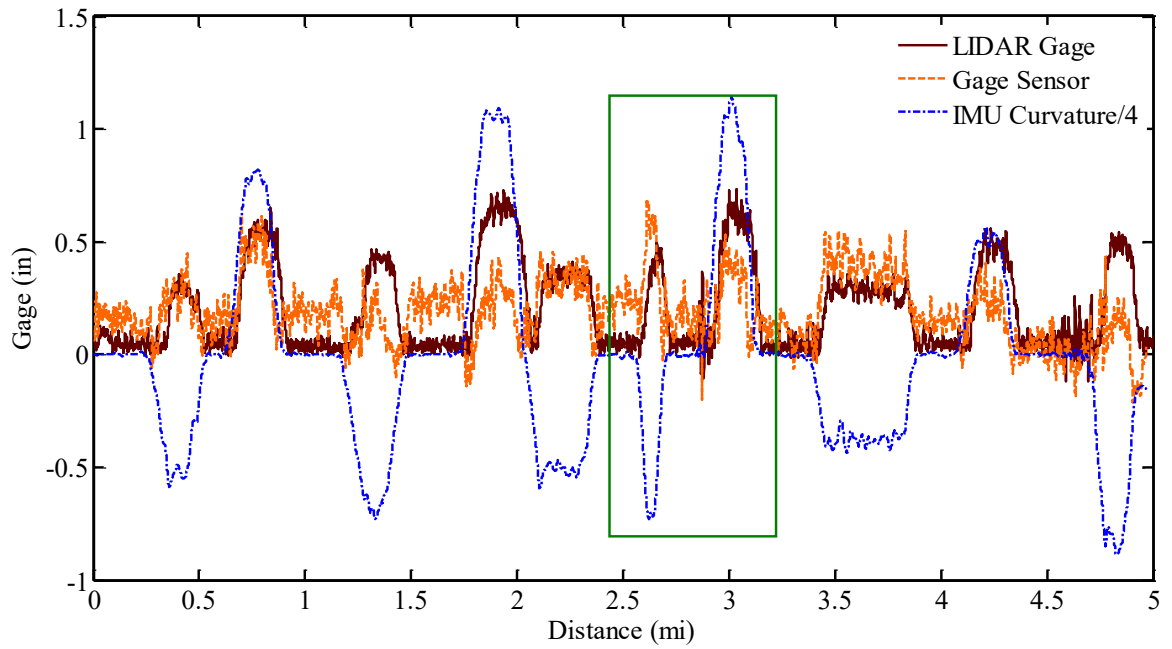


Figure 4-25. Overall gage variation comparison of LIDAR and onboard gage sensor measurements in the spatial domain.

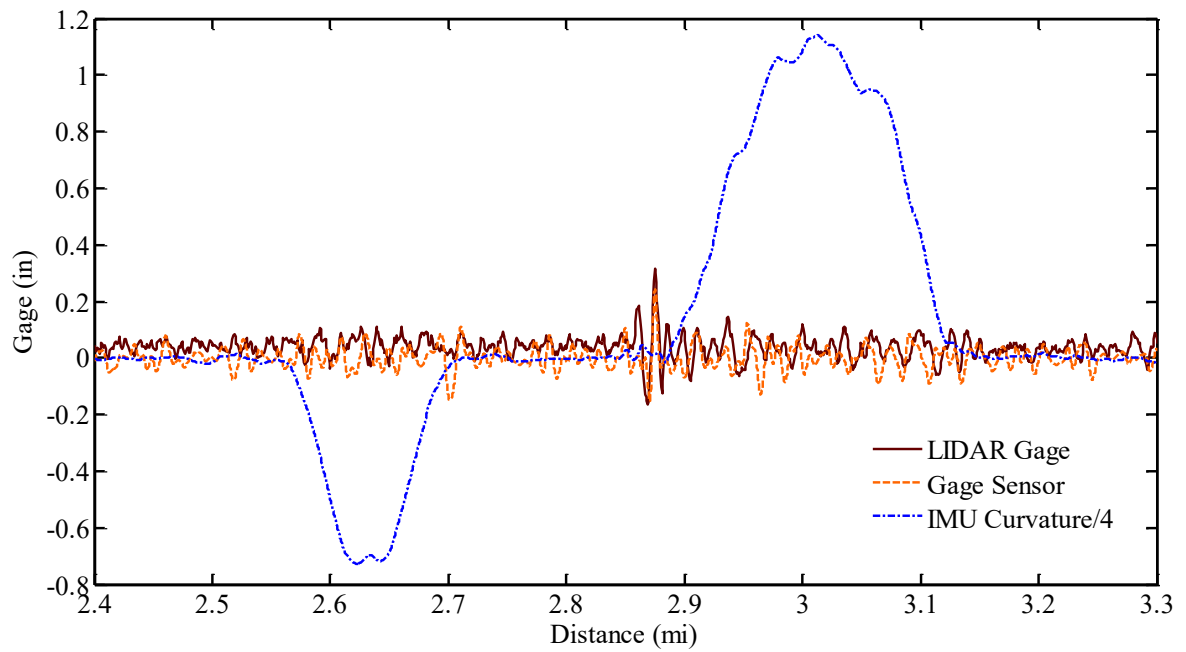


Figure 4-26. Gage variation in the boxed section in Figure 4-25.

Chapter 5 Vertical Track Geometry Monitoring

This chapter explains the applicability of a Light Detection and Ranging (LIDAR) system for measuring vertical track geometry condition simultaneously with track speed. The suitable LIDAR embodiment is introduced, and effective parameters are elaborated. Regarding geometry considerations, a signal-processing algorithm is proposed to derive track speed, profile, and track elevation from LIDAR speed measurements. The LIDAR system is mounted on NS38 inspection car and fiducially calibrated. Track geometry data is collected and probability distribution functions are used to quantitatively evaluate the quality of the LIDAR measurements.

5.1 LIDAR Sensing and Processing

A Doppler sensor measures rate of deflection occurring in the direction of the laser beam. The ideal LIDAR lens orientation for vertical track geometry measurements is such that the laser strikes parallel to the direction of rail vertical motion (Figure 5-1). With this configuration, the measured velocity is identical to the velocity of rail vertical motion/deflection. With this orientation, however, the rail forward velocity is not recorded by the LIDAR system. Without the forward speed component, the rail vertical direction cannot be detected. This orientation was not possible during field testing due to installation limitations.

Figure 5-2(a) shows the two LIDAR sensors used for vertical geometry monitoring. LIDAR system is used with a gage corner beam configuration as shown in this figure. The train speed is calculated from the LIDAR left and right forward bias speed measurements. These two velocities are termed V_L and V_R , and are labeled in Figure 5-2(b). Figure 5-2(c) shows a front view of the rails, while the LIDAR beams detect the left and right vertical speeds (v_R and v_L). These velocity components and their calculation algorithm are further discussed in the following section.

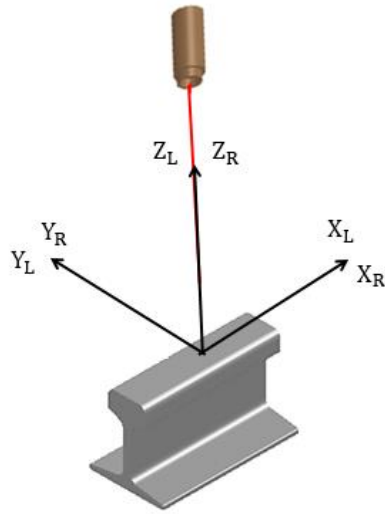
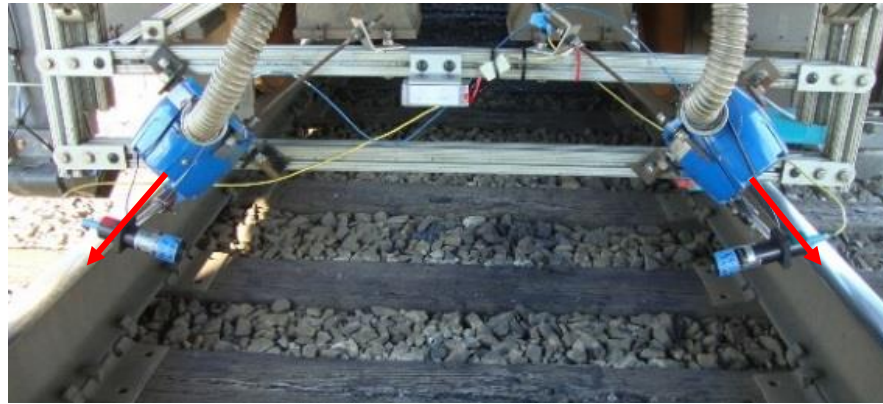


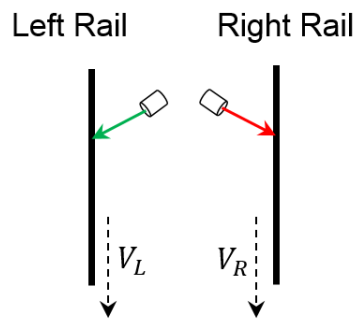
Figure 5-1. The ideal LIDAR lens orientation for vertical track geometry measurements overlays the rail coordinate system with the laser coordinate system. With this orientation, however, the rail forward velocity is not recorded. This orientation was not possible during field testing due to installation limitations.

In this chapter, since the goal is to extract the vehicle velocity and vertical track geometry irregularities simultaneously, LIDAR sensors are not positioned exactly perpendicular to the rail surface, but the lasers strike the rail face with a bias angle of θ . Also, due to mounting consideration, the lasers have an extra inclination angle of φ with the rails. As a result of this configuration, each sensor's reading has a component of forward driving speed and the vertical deflection velocity. As an example, the proposed embodiment is shown in Figure 5-3 for the right rail, while neglecting the rail lateral motion. In this case, the velocity measured by the right sensor, V_{mR} , is related to the right rail forward velocity and right vertical deflection velocity as:

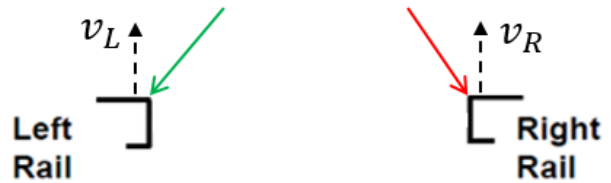
$$V_{mR} \approx V_R \sin \theta + v_R \sin \varphi \cos \theta \quad (5-1)$$



(a)



(b)



(c)

Figure 5-2. Vertical LIDAR optics used for vertical geometry measurements; (a) beams target the gage corner of the rails, (b) left and right track speeds are measured, (c) rates of left and right vertical geometry are observed by the lateral lenses.

5.1.1 Track geometry estimation

The variation of vertical track irregularities can be computed if the rate of vertical deflection is known. As discussed above, due to a non-perpendicular beam configuration, LIDAR's measured velocities (V_{mR} and V_{mL}) are related to forward bias speeds (V_R and V_L) and vertical rail velocities (v_R and v_L). A calculation algorithm is proposed to separate and process these terms, as illustrated in Figure 5-4. According to this flow-chart, the raw measured speeds are passed through a low-pass filter to derive the forward bias speeds (V_R and V_L). The average of forward speeds yields the centerline velocity (V_{CL}), which is used to calculate the travelled distance of the vehicle.

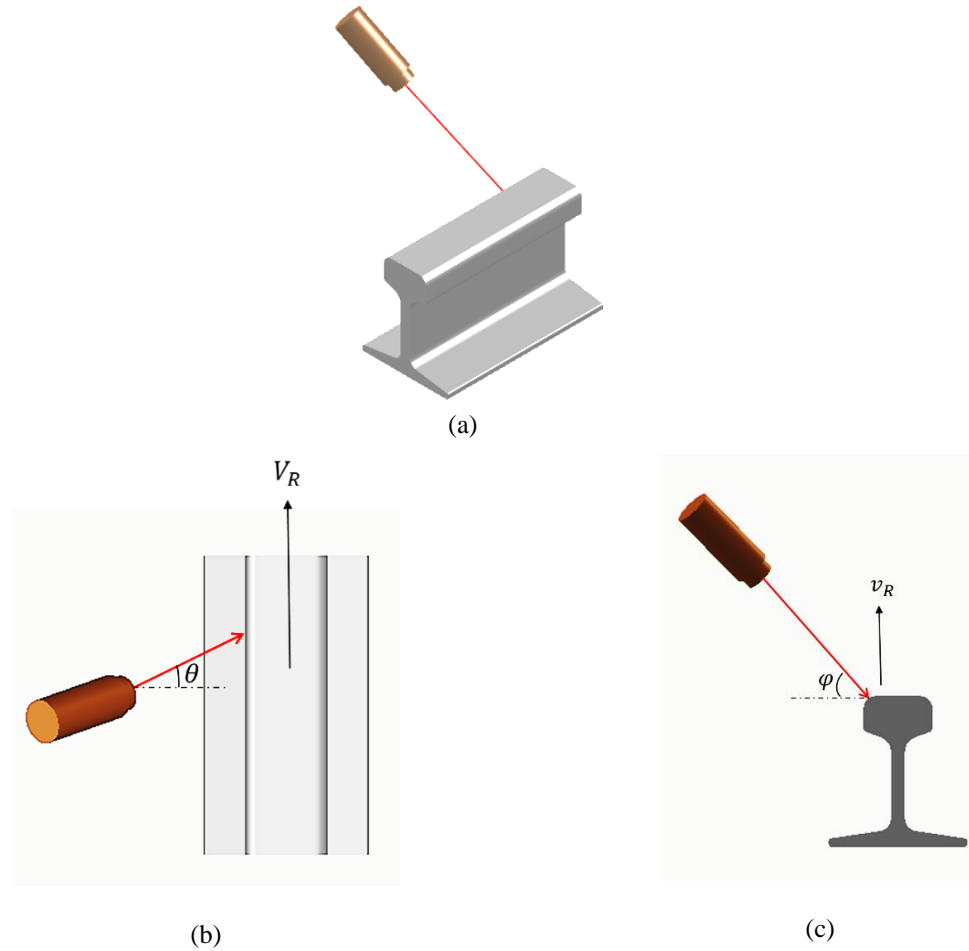


Figure 5-3. Velocity measurement of the right LIDAR sensor; 3-D isometric view of the embodiment and right rail, (b) top view of the embodiment and right rail, (c) front view of the embodiment and right rail.

In order to extract the rail vertical velocity according to Equation (1), the computed forward bias velocity is first multiplied by the sine of bias angle ($\sin \theta$), and then subtracted from the raw velocity signal. Vertical inclination of the laser direction is then compensated by multiplying the resultant velocity terms by $\cos \varphi$ to obtain the right and left vertical velocities (v_R and v_L).

Profile or vertical surface displacement P_L is calculated as:

$$P_L = \Delta t \alpha_{LP} v_L \tag{5-2}$$

where α_{LP} is the left profile scaling factor and Δt is time increment. For the right profile, P_R the following expression is used:

$$P_R = \Delta t \alpha_{RP} v_R \quad (5-3)$$

where α_{RP} is the right profile scaling factor. The scaling parameters, α_{LP} and α_{RP} , are not identical if the laser beams are not perfectly aligned.

Track elevation variation is assumed to be a function of left and right vertical velocities, as well as forward bias speeds. A linear relation is proposed in this work for the track elevation variation ΔE as:

$$\Delta E = \Delta t [\alpha_{RP} v_R - \alpha_{LP} v_L] + \beta_E (V_R - V_L) \quad (5-4)$$

where the track curvature is taken into account with a constant parameter β_E . The values of introduced parameters are listed in Table 5-1.

Table 5-1. Numerical values used in the processing of LIDAR data for calculation of vertical track geometry parameters

SYMBOL	PARAMETER	VALUE
θ	lens bias angle	30 degrees
φ	lens inclination angle	75 degrees
α_{LE}	left vertical profile correction factor	0.6
α_{RE}	right vertical profile correction factor	0.7
β_E	track curvature correction factor for the track elevation	1.4
-	forward velocity cut-off frequency	0.2 Hz

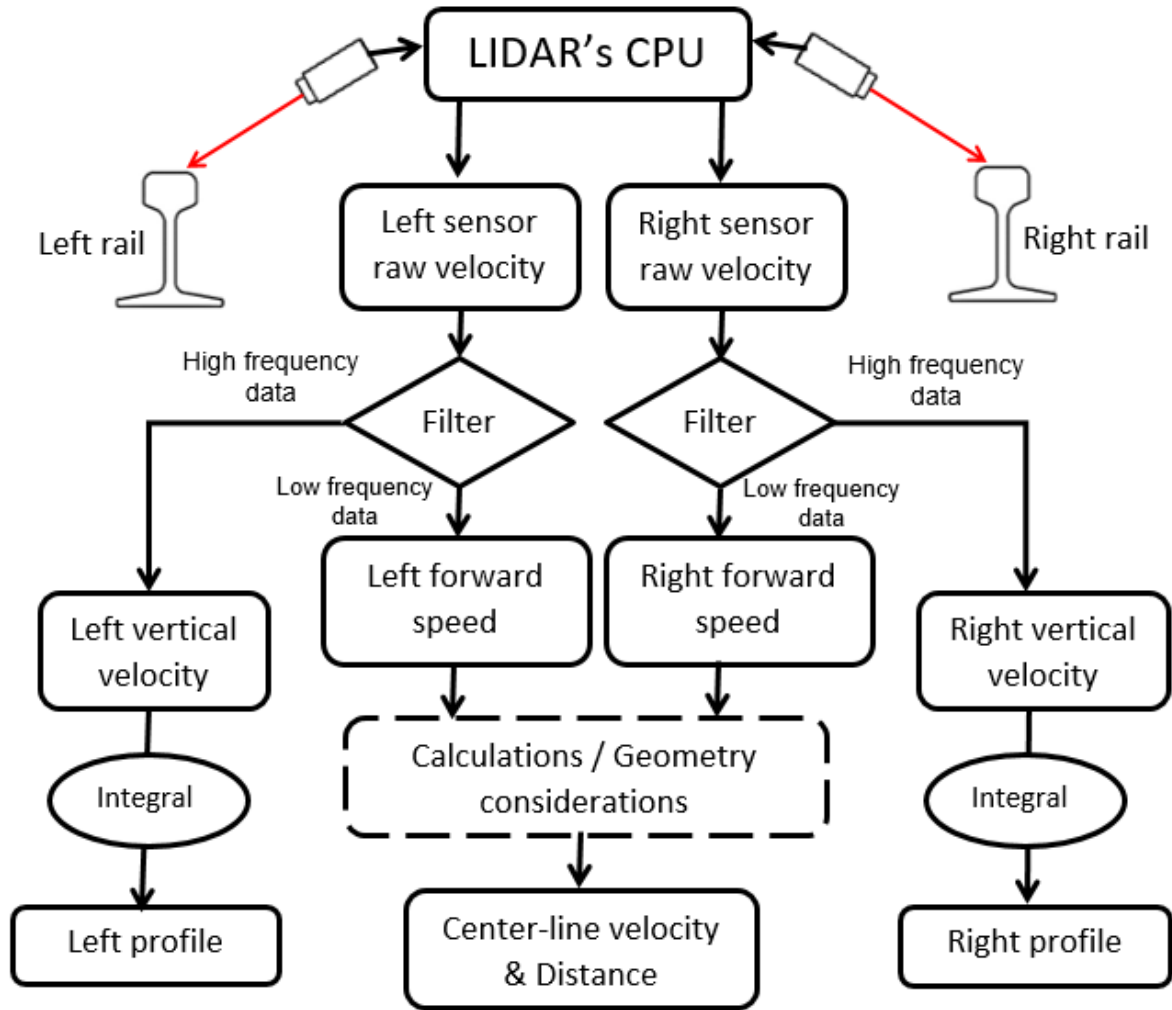


Figure 5-4. Calculation procedure applied to LIDAR measurements to extract vertical track irregularities.

5.2 Experimental Results and Evaluation

For the sake of comparison, a sample of 5 miles (from mile-posts N221 to N216) is selected, and LIDAR's capability for the profile and elevation measurements is evaluated over this zone. This portion of data includes multiple sections of tangent and curved tracks.

Figure 5-5 shows the left and right forward bias speeds (V_L and V_R) versus time. These two speeds must be evaluated before extracting the vertical terms of speed from the LIDAR data.

They also represent the curvature of the track. The average of forward bias velocities represents the centerline speed, and it is compared to a wheel-mounted encoder speed in Figure 5-6.

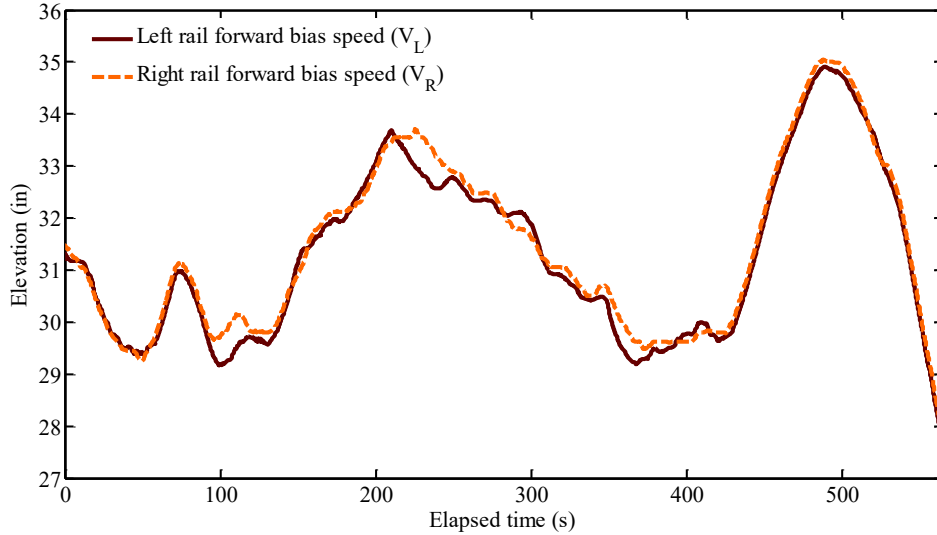


Figure 5-5. Forward left and right rail speeds determined from the bias forward angle of the lenses.

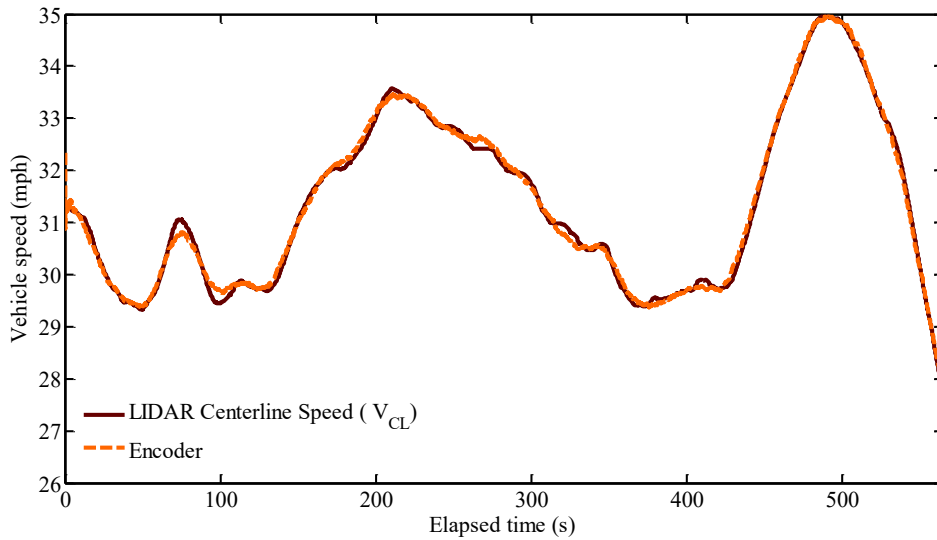
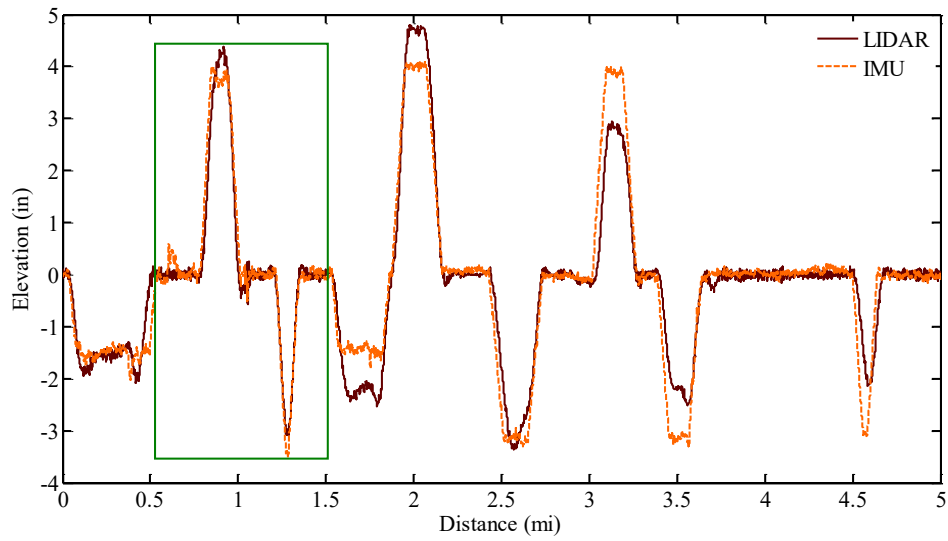


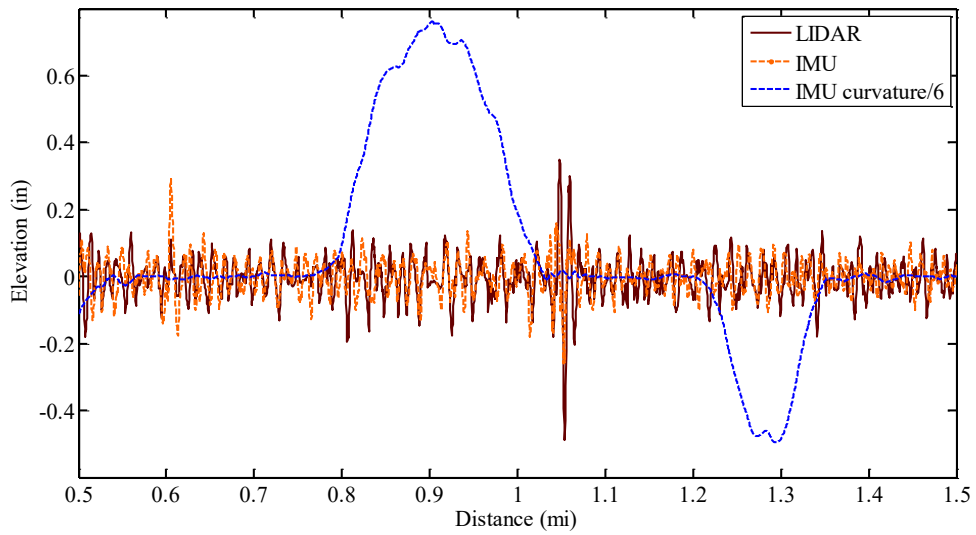
Figure 5-6. The computed centerline speed from the left and right speed signals compared with the encoder signal. A good correlation exists between the two instruments' estimation of speed.

Similar to lateral track geometry measurements, track elevation is best evaluated in the spatial domain rather than in the time domain. The calculated LIDAR track elevation is

compared to the onboard IMU reading in Figure 5-7(a). For this figure, elevation in inches is approximately equal to track cant in degrees. This plot shows a good general agreement between LIDAR and IMU measurements. The average difference between the two sensors is 1.2%, with a standard deviation of 23.6%. As expected, abrupt changes (which explain the wide standard deviation) are observed in the elevation readings over curves due to the high non-linear beam angles. The local elevation variations, which are caused by instantaneous vertical deviations, not the gross curvature, for the boxed section of Figure 5-7(a) are compared in Figure 5-7(b). This boxed section corresponds to the time between 40 and 180 seconds in Figure 5-6, where the average speed is around 30mph. The IMU curvature reading is also overlaid on the plot in Figure 5-7(b). In this figure, the LIDAR closely matches the IMU vertical data in measuring the range and variation trend of the instantaneous deviations. However, exact mathematical spatial correlation again cannot be easily achieved since the measurements are made asynchronously and by sensors whose mounting locations are physically displaced from one another. Similar comparisons are made for the right and left rail profiles in Figure 5-8 and Figure 5-9 through the specified zone. These plots again show that the two monitoring units measure the same range of variation (magnitude), although the exact spatial correlation is not possible without the correction of the large beam angles.



(a)



(b)

Figure 5-7. Comparison of LIDAR and IMU track elevation measurements in spatial domain; (a) total track elevation, (b) track elevation variation in the specified segment.

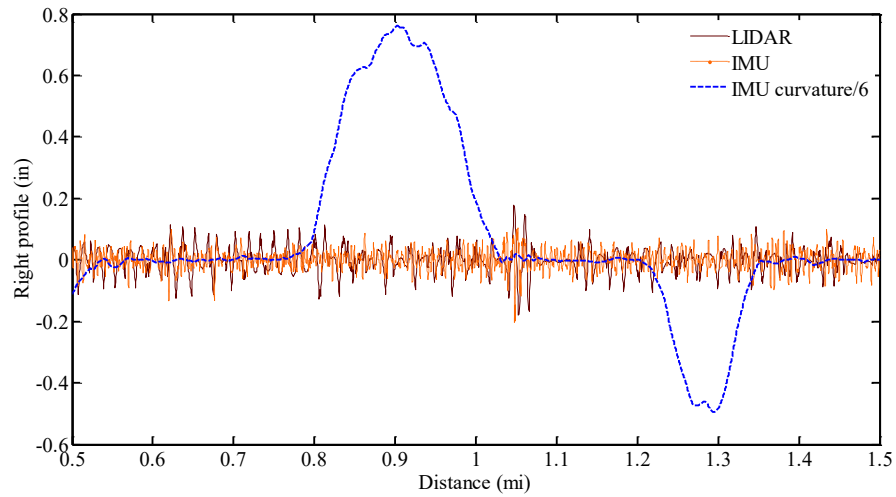


Figure 5-8. Comparison of LIDAR and IMU right profile in spatial domain for 1 mile of the track.

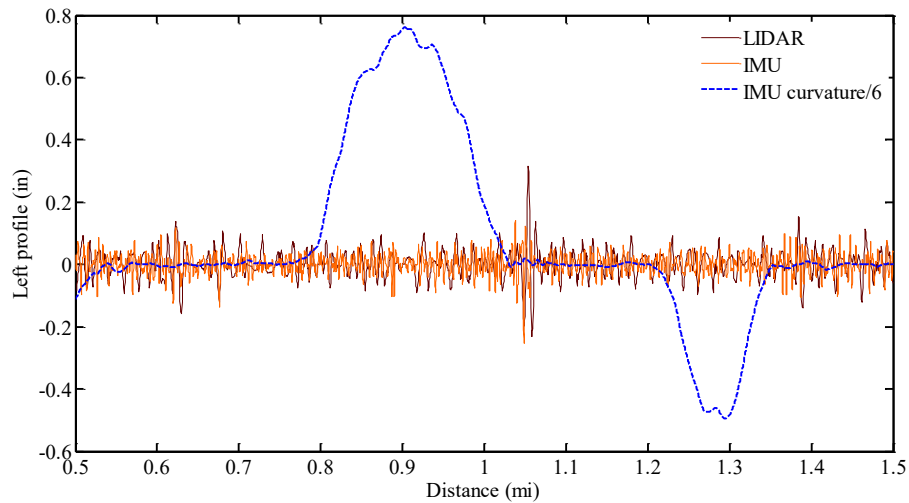
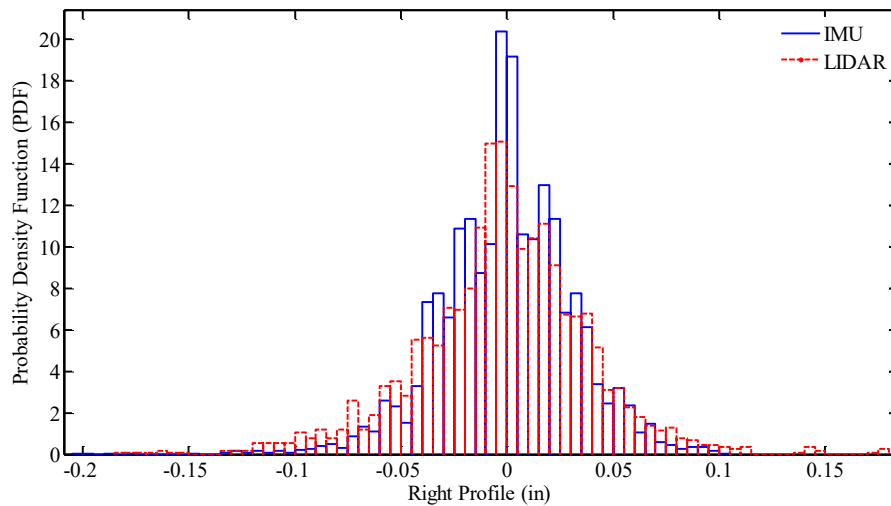


Figure 5-9. Comparison of LIDAR and IMU left profile in spatial domain for 1 mile of the track

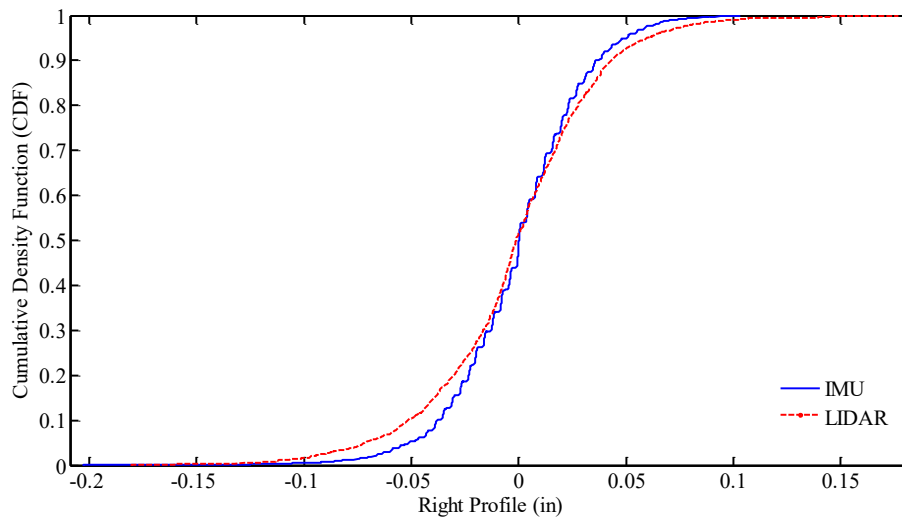
5.3 Probability Analysis

In order to investigate the correlation between LIDAR and IMU measurements, probability density functions (PDF) and cumulative density functions (CDF) of the two monitoring methods for the right and left profiles, as well as track elevation, are calculated as shown in Figure 5-10 through Figure 5-12. These probability distributions show good agreement

between the two measuring units. Moreover, the 95th percentiles of the data are also computed: 95% of the LIDAR and IMU track elevation measurements fall below 0.086 in and 0.077 in, respectively. For the right profile, 95th percentile of the LIDAR and IMU measurements are 0.05 and 0.059 in. This measure for the LIDAR left profile is 0.055 in, and for the IMU, it is 0.071 in.

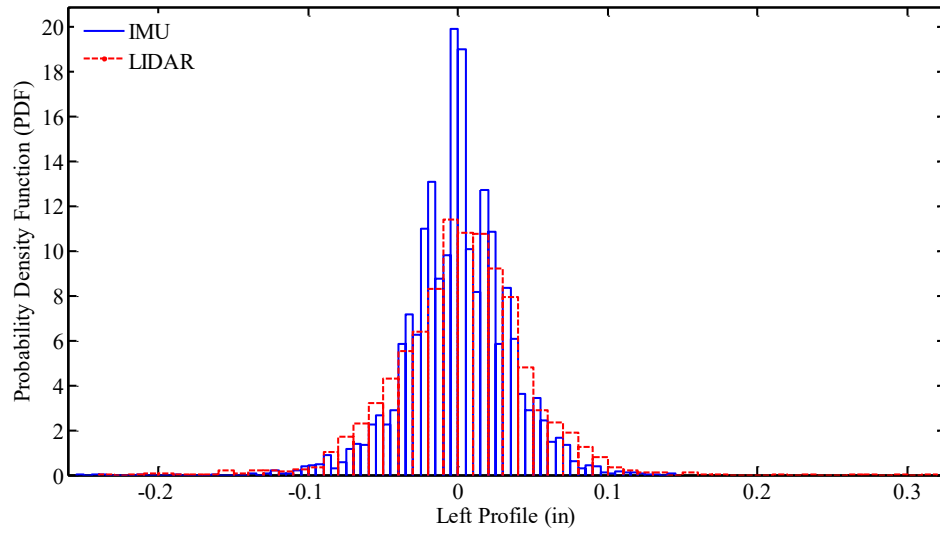


(a)

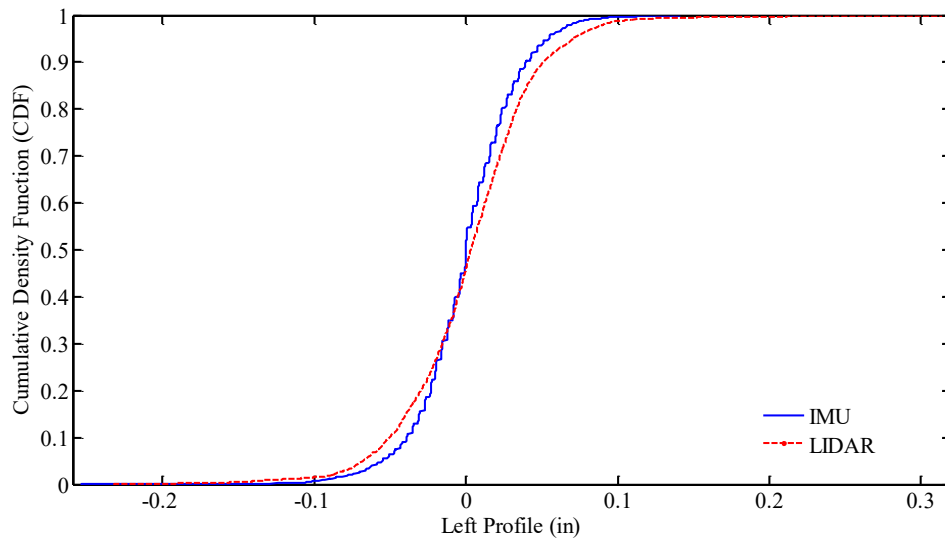


(b)

Figure 5-10. Probability distributions of LIDAR and IMU right profile measurements; (a) right profile variation probability density function (PDF), (b) right profile variation cumulative density function (CDF).

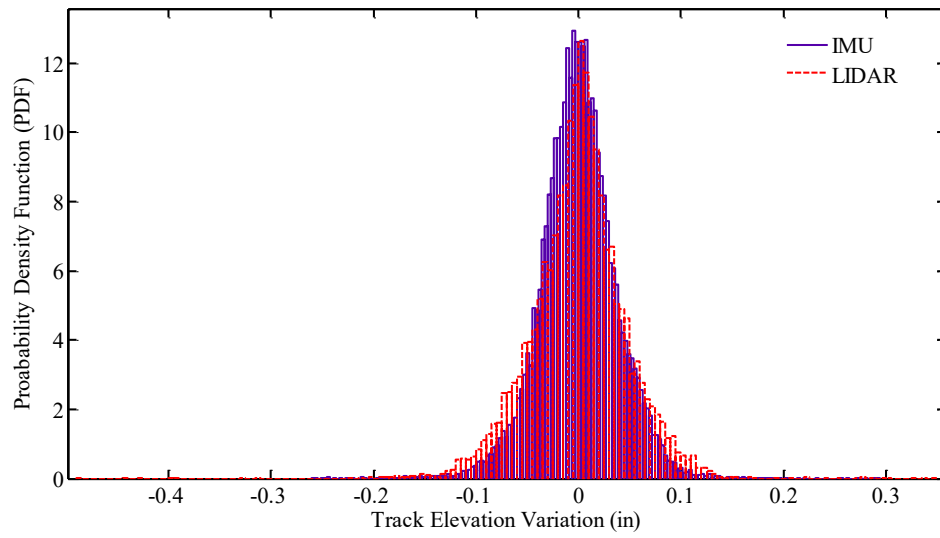


(a)

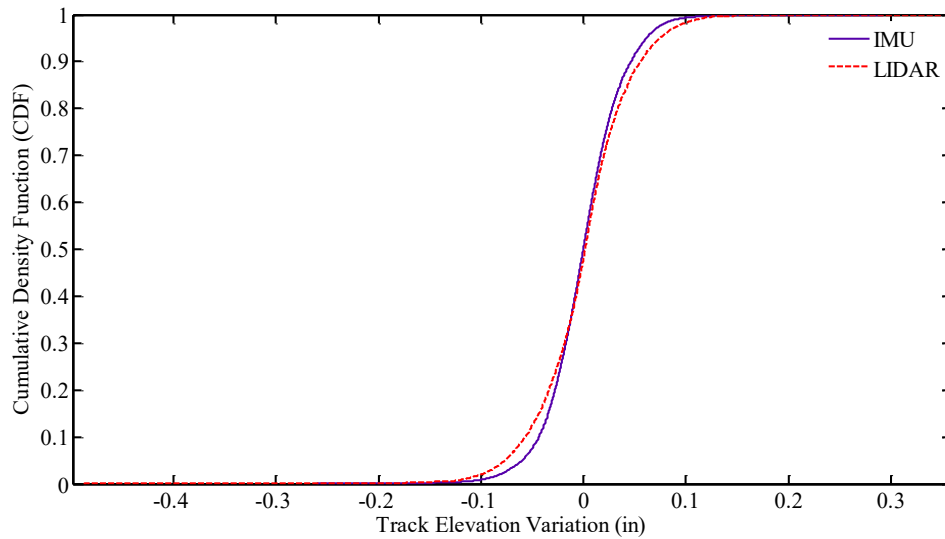


(b)

Figure 5-11. Probability distributions of LIDAR and IMU left profile measurements; (a) left profile variation probability density function (PDF), (b) left profile variation cumulative density function (CDF).



(a)



(b)

Figure 5-12. Probability distributions of LIDAR and IMU track elevation measurements; (a) track elevation variation probability density function (PDF), (b) track elevation variation cumulative density function (CDF).

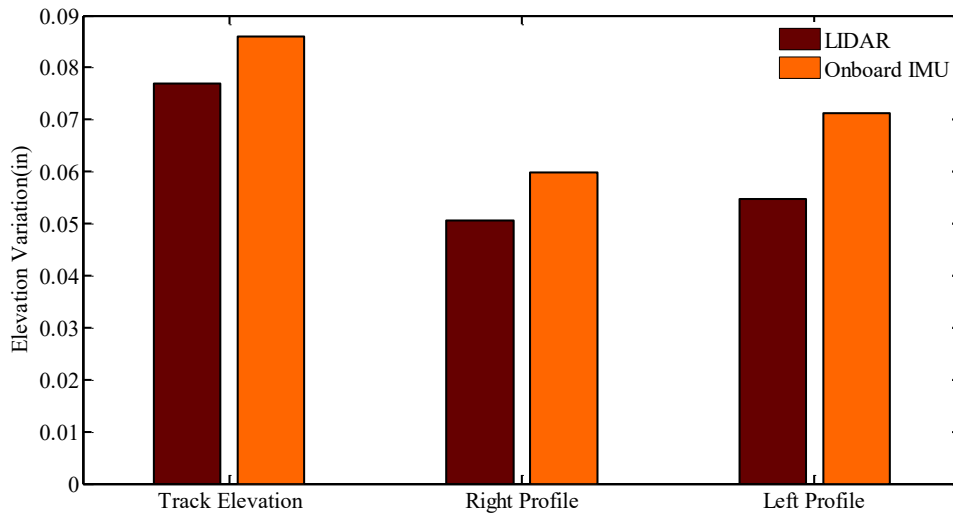


Figure 5-13. 95th percentile amplitude distribution elevation measurements

The results presented above confirm the utility of the LIDAR velocity detection system in measuring vertical deviations of track rails. The data from the field tests demonstrate the capability of developed signal processing algorithms to identify and separate the different vector speed components to calculate the variations in track geometry. The results show very good agreement for track elevation and profile between LIDAR measurements and other established measurement methods (IMU). The relative accuracy of the LIDAR will improve as the non-linear scale factors, due to the large beam angle of attack, are compensated, or as alternate, shallow beam geometries are used.

Chapter 6 Bi-directional Speed Measurement Using LIDAR

The application of Doppler-based, Light Detection and Ranging (LIDAR) technology for measuring train velocity in the presence of track-induced dynamics is experimentally investigated. Track-induced vibrations cause high-frequency oscillation in the LIDAR velocity measurements. Train speed is also captured by Doppler optics and allows for directional vibration detection by creating an off-set low-frequency velocity component. A frequency bandwidth-based process is implemented to separate the driving and vibration contributions of the LIDAR velocity measurements. An extensive series of tests are conducted to determine the feasibility of the proposed approach. Results indicate that various vibration waveforms with different driving frequencies and amplitudes can be detected by the designated LIDAR embodiment. Measurements can be made at different driving speeds and surface figures. Moreover, self-normalizing the LIDAR speed measurements yields a vibration index, which can be employed to detect and assess the track infrastructure elements. Using LIDAR sensors to measure track-induced dynamics facilitates track health monitoring and defect detection.

6.1 Bi-directional Speed Measurement

A Laser Doppler Velocimetry (LDV) sensor measures the velocity of an object moving in the direction of the emitted beam. Normally, the Doppler sensor is mounted so that the laser strikes parallel to the direction of motion, and the measured velocity and object velocity are identical. This 1-D speed measuring method is suitable for objects with only one speed component or for 2-D or 3-D moving targets where only one of their speed components is to be recorded.

As shown in Figure 6-1, the LDV can make 2-D speed measurements if it is not positioned exactly perpendicular to the front surface of the target, but oriented with a bias angle of θ .

The target in this figure translates in the x-direction with the speed of v_x , while oscillating in the perpendicular direction (y) with the speed of v_y . In this case, the measured velocity, V_m is related to two orthogonal speed components as:

$$V_m = v_x \sin \theta + v_y \cos \theta \quad (6-1)$$

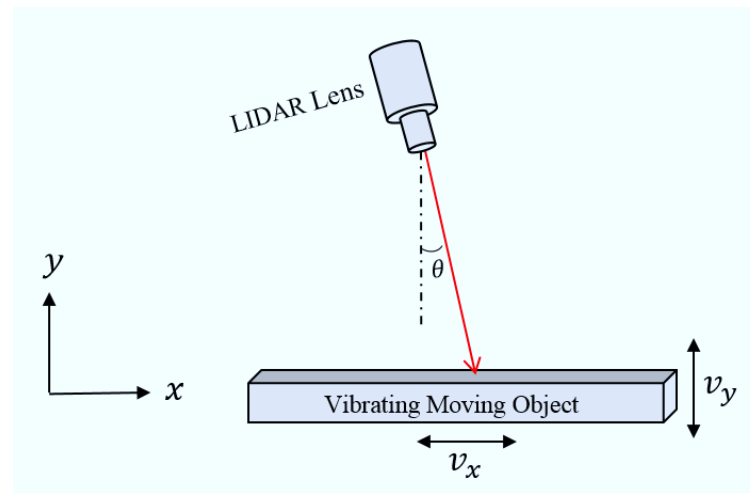


Figure 6-1. LIDAR speed measurement contains information about both translational speed (x-direction) and oscillating velocity (y-direction) when the lens is oriented and the laser strikes the moving target with a bias angle.

The LIDAR system measures track speed when it is car/body-mounted and its laser strikes the rail. The measured track speed (V_m) has a primary low-frequency, off-set component that demonstrates the train forward speed (v_x), and a secondary high-frequency, low magnitude speed component as a result of track vibration perpendicular to the rolling direction (v_y). Depending on the mounting geometry, this vibration could be vertical or lateral. Forward speed can be measured for both the left and right rails and averaged to compute the centre-line velocity and distance travelled, or differentiated to derive the track curvature. On the other hand, the extracted track-vibration speed component reveals rich information about the health condition of the track. This component can be further integrated over time to establish the induced deflection. The frequency contents of the vibration can

also be found and employed, together with the deflection information, to detect track defects and/or track infrastructure condition. By employing distance travelled data, the exact position of the defects and infrastructures can also be determined. This enables the LIDAR unit to perform independently of the Global Positioning System (GPS).

6.2 Experimental Set-up

An extended experimental study is conducted at the Railway Technologies Laboratory (RTL) at Virginia Tech. The purpose is to demonstrate the applicability of the proposed approach (discussed above) in extracting the track-induced dynamics from LIDAR track speed measurements. Lab testing is selected over field testing since it offers a controllable and suitable environment necessary for accurate dynamic tests. Additionally, LIDAR can be extensively evaluated against other measuring techniques available at the laboratory, while measurements are limited when made onboard a track geometry car. Field tests, however, are recommended to be carried out in a future program to further assess the performance of the LIDAR system in real-world conditions.

In the following, a brief description of the testing equipment and LIDAR data processing unit for the vibration characterization is presented.

6.2.1 Instrumental equipment

The LIDAR sensor is mounted to the right column of the Roehrig damper dynamometer. The Roehrig dynamometer provides a robust platform to conduct axial mechanical tests at a wide range of excitation waveforms and frequencies, and has been previously exploited for damper characterization. As shown in Figure 6-2, the rotary disk is placed on the Roehrig actuator, which produces out-of-plane (vertical) vibration, simulating the track dynamics.

In order to replicate the linear motion of the train (forward track speed), a steel disk is mounted to a 9V high-speed DC motor and rotated in constant speed. A rotary disk is attached to the Roehrig actuators in two different configurations for the tests reported in this

paper. In the first configuration, as shown in Figure 6-3 (a), the LIDAR beam targets the disk face. This allows a wide range of bias angles and off-set speeds at a constant driving voltage. This configuration, however, leads to erroneous measurements when the disk is vertically actuated with large amplitude of displacement and the striking point moves radially on the disk. To overcome this issue, the disk can be mounted vertically, as depicted in Figure 6-3 (b). The laser strikes the disk's wall and linear speed remains constant at different vertical locations of the actuator. The bias angle, however, is more limited in this embodiment, and it strongly depends on the wall thickness of the disk. Sandpaper is adhered to the disk in order to increase the surface roughness and improve the intensity of the scattered beam. As will be shown later, the LIDAR system can make successful vibration measurements even when light is emitted to a polished surface.

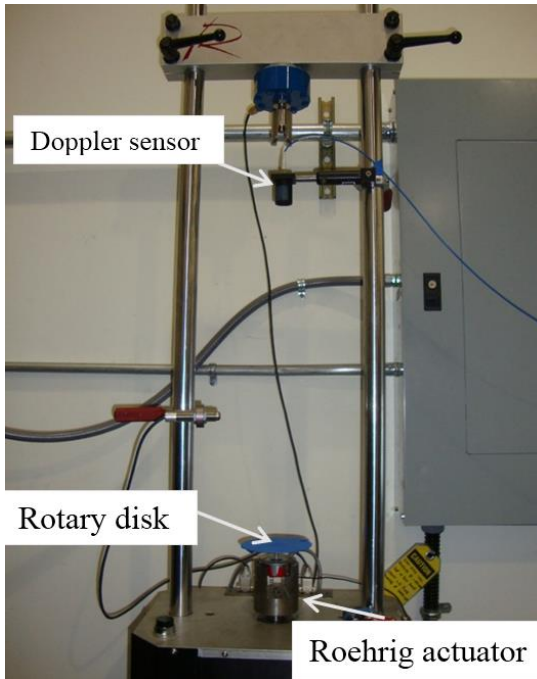
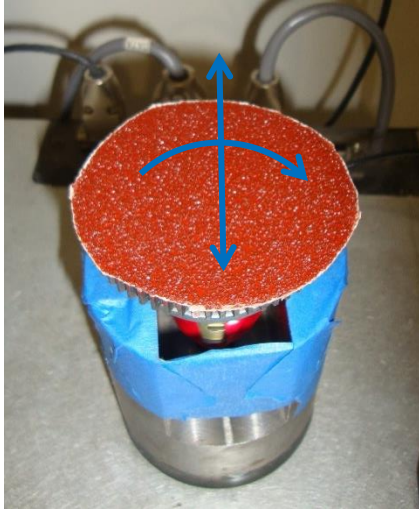
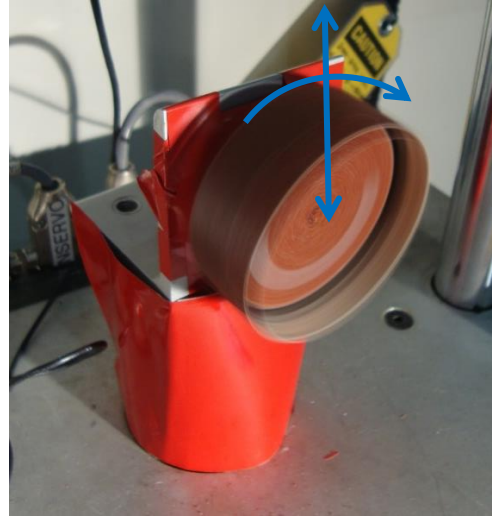


Figure 6-2. LIDAR-Roehrig set-up; the rotary disk replicates vehicle speed, and the Roehrig electromagnetic actuator simulates track dynamics by vertically vibrating the disk. The LIDAR beam strikes the disk face with a slight bias angle to allow for 2-D speed measurements.



(a) Disk face configuration



(b) Disk wall configuration

Figure 6-3. A rotary disk is mounted on the Roehrig in two configurations: a) LIDAR beam targets the disk face. This configuration allows for a wide range of bias angles and off-set speeds. (b) LIDAR strikes the wall. This embodiment allows for larger vertical motions to be simulated while keeping the constant linear motion.

6.2.2 Data acquisition and processing set-up

The Doppler shift measured by the optic is passed to a central processing unit (CPU) through a high-fidelity RF device. The CPU that is employed in this study is a National Instruments (NI) PXI Computer (Figure 6-4). The PXI computer performs a number of tasks in real time, including computing the Fast Fourier Transform (FFT) of the LIDAR signal, establishing the target velocity. Doppler frequency is sampled at 1 MHz, frequency analyses are done with 256 FFT point, and speed data is recorded at 100 Hz.

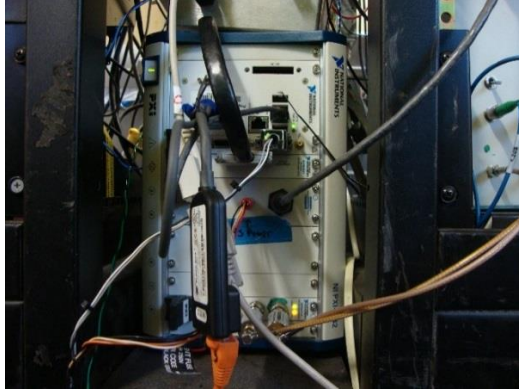


Figure 6-4. A National Instrument PXI computer is employed to perform FFT analysis and compute target speed from Doppler frequency shift.

6.3 Results and Discussion

Numerous tests are conducted at different off-set speeds with various actuation waveforms, driving frequencies, and surface figures. In this section, the data from some of these tests are presented to show how the proposed measuring technique can be implemented to capture and characterize the track-induced dynamics.

6.3.1 Vibration detection

LIDAR speed data (V_m) is shown in Figure 6-5 for a test with 10 in/s off-set speed. This plot shows how the oscillating velocity, generated by the Roehrig actuators, *rides* on the off-set speed caused by the rotary disk. The disk starts to rotate until it reaches a constant speed at the plateau. This speed relates the second term on the right-hand side of Equation (6-1) as ($v_x \sin \theta$). Beginning from 42 (s), the actuator begins to vibrate the disk in a sinusoidal waveform at 5 Hz for 20 cycles. A closer view of the oscillating section and measured vibration speed (v_y) is shown in Figure 6-5. Direction of the oscillation is detected within the off-set speed, which is labelled as V_{limit} . This speed limits the maximum rate of vibration. The DC motor is finally turned off at 52 (s) and speed drops to zero.

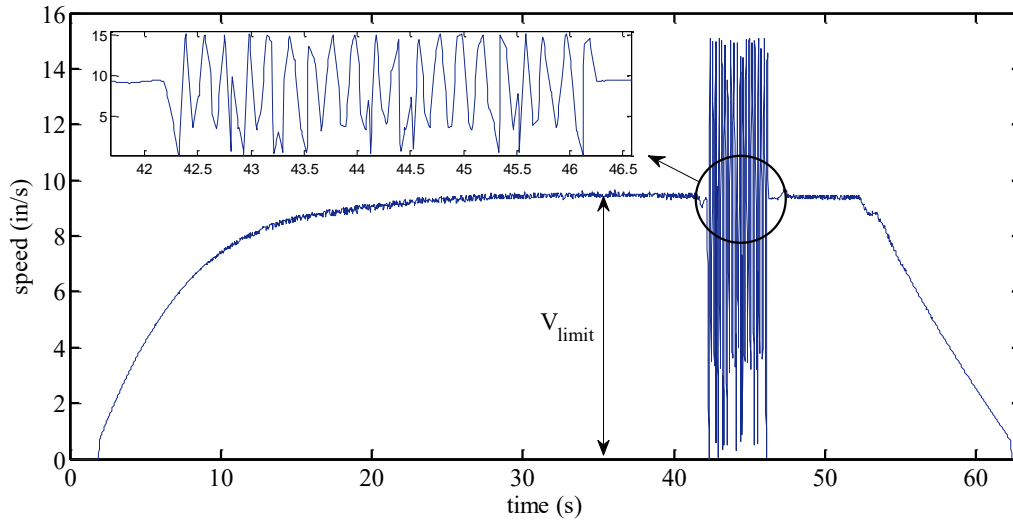


Figure 6-5. LIDAR speed measurements with the presence of vibration; the rotary disk starts to rotate and generates the off-set speed required to detect the sinusoidal oscillation applied by the Roehrig actuator.

6.3.2 Oscillation shape characterization

LIDAR is able to detect and extract different vibration waveforms from the off-set driving speed. Figure 6-6 shows the oscillation speed of a 1 Hz sinusoidal vibration with 0.5 in displacement amplitude. LIDAR oscillation speed data is calculated by subtracting the 10 in/s off-set speed from the overall speed measurement. This plot shows how LIDAR measurements match closely with the Roehrig velocity output. The same comparison is made in Figure 6-7 for the case when a 1 Hz triangular excitation with 0.5 in amplitude is applied.

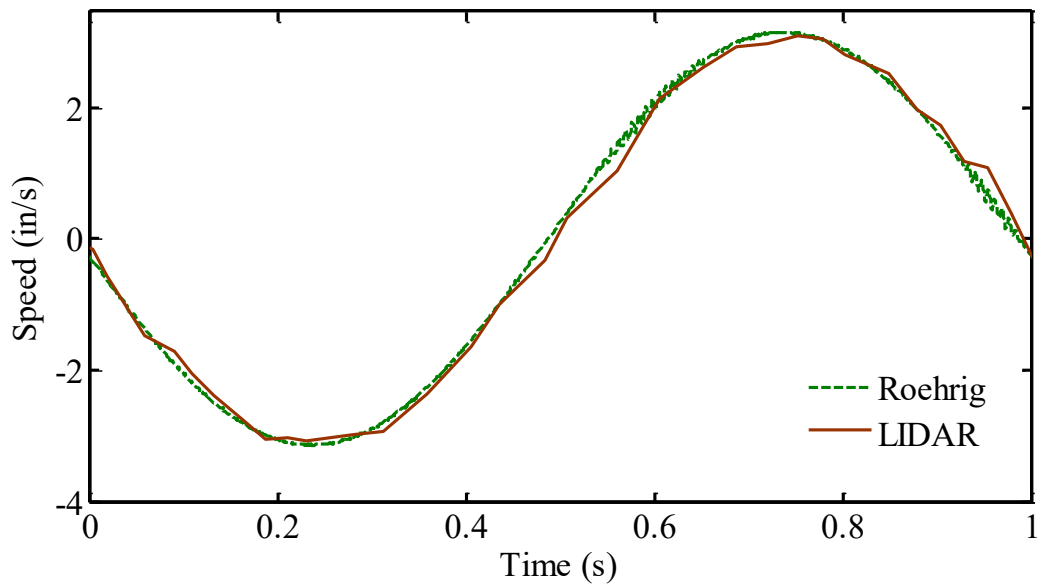


Figure 6-6. LIDAR speed measurement for a sinusoidal displacement excitation with amplitude of $A=0.5$ in and frequency of $f=1$ Hz is compared with the Roehrig velocity reading for 1 cycle.

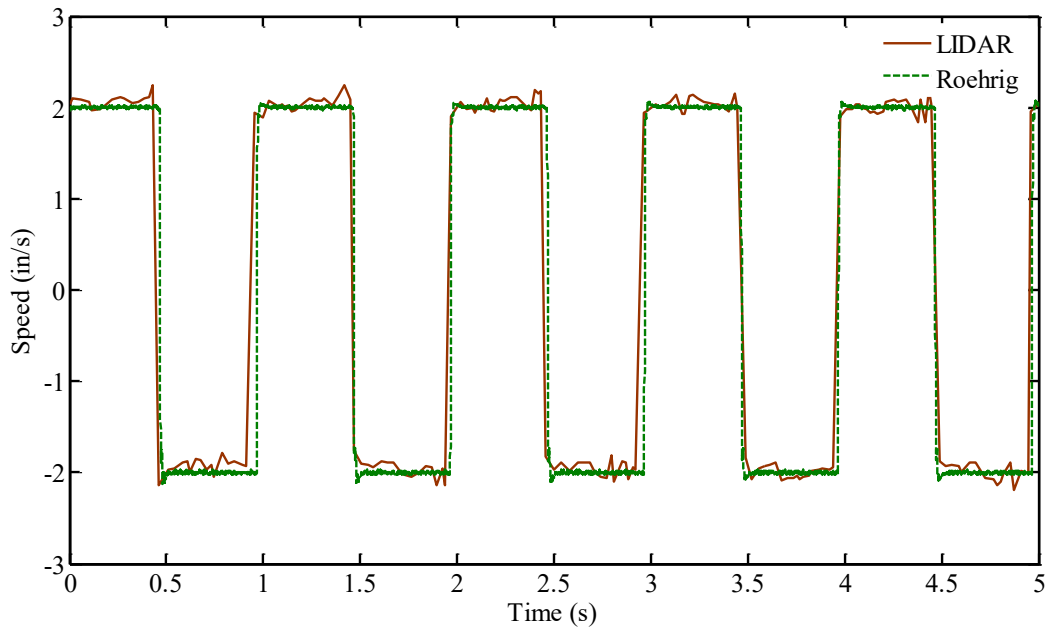


Figure 6-7. LIDAR speed measurement for a triangular displacement excitation with amplitude of $A=0.5$ in and frequency of $f=1$ Hz is compared with the Roehrig velocity reading.

6.3.3 Frequency spectrum characterization

Analyzing the frequency content of high-fidelity data is useful for quantifying the dynamic behavior of a mechanical system by identifying the major vibratory sources of the system, and for establishing the impact of those vibrations. To evaluate the functionality of the LIDAR system in detecting different frequency contents, a variable frequency test is conducted. The disk is rotated while four sinusoidal oscillation waveforms ranging from 5 to 20 Hz are applied. Each excitation is repeated 100 times. The amplitude of the sinusoid (A) for each excitation is selected so that maximum velocity ($|V| = A\omega$) is constant and equal to 1 in/s. Figure 6-8 shows the FFT analysis of the LIDAR oscillatory speed data. All four driving frequencies are captured and labeled on the plot.

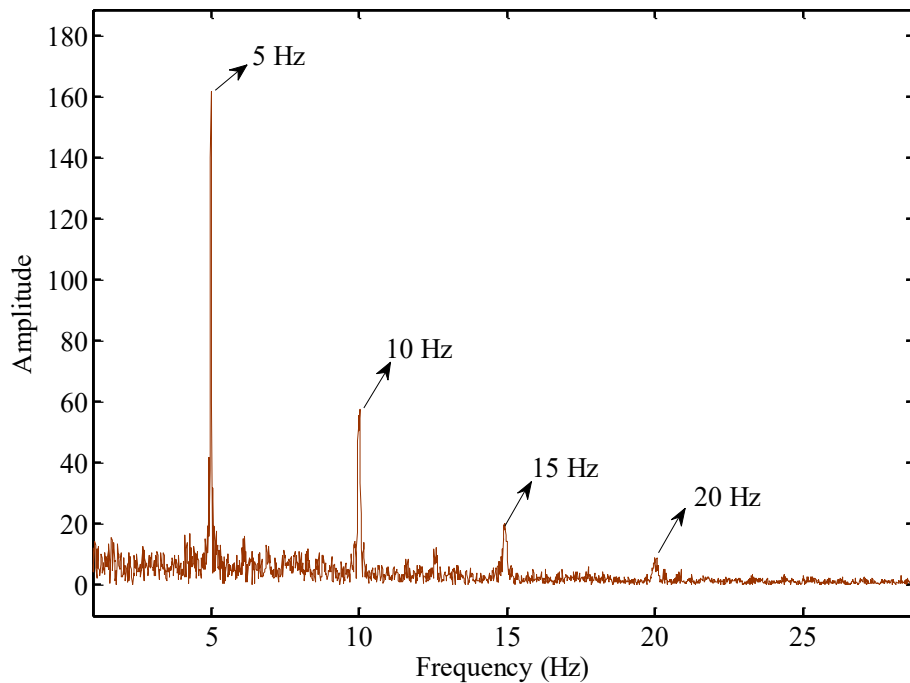


Figure 6-8. FFT response of LIDAR velocity measurement for sinusoidal excitations with 1 in/sec maximum vertical velocity.

6.3.4 Intricate mechanical vibration series

The rotary disk is vertically actuated by a sequence of six waveforms with different amplitudes, frequencies, and shapes. The specifications of these waveforms are listed in a table on the right side of Figure 6-9. Short-time Fourier transform (STFT) of LIDAR oscillatory speed data is computed and plotted in Figure 6-9. STFT determines the frequency content of local sections of the velocity signal as it changes over time. This kind of STFT data, when overlaid with distance data, can provide rich information about specific sections of the railway track. FFT response of the measurements is also depicted in Figure 6-10. One can easily identify all the major frequency contents of the applied vibration sequence (1 Hz, 2 Hz, 5 Hz, and 10 Hz) from this plot. In addition to frequency content, amplitude of the vibrations can also be established by integrating the LIDAR oscillatory speed data. LIDAR displacement trajectories for four of the applied waves are compared with the Roehrig's data in Figure 6-11. These graphs show good agreement between the two measuring units.

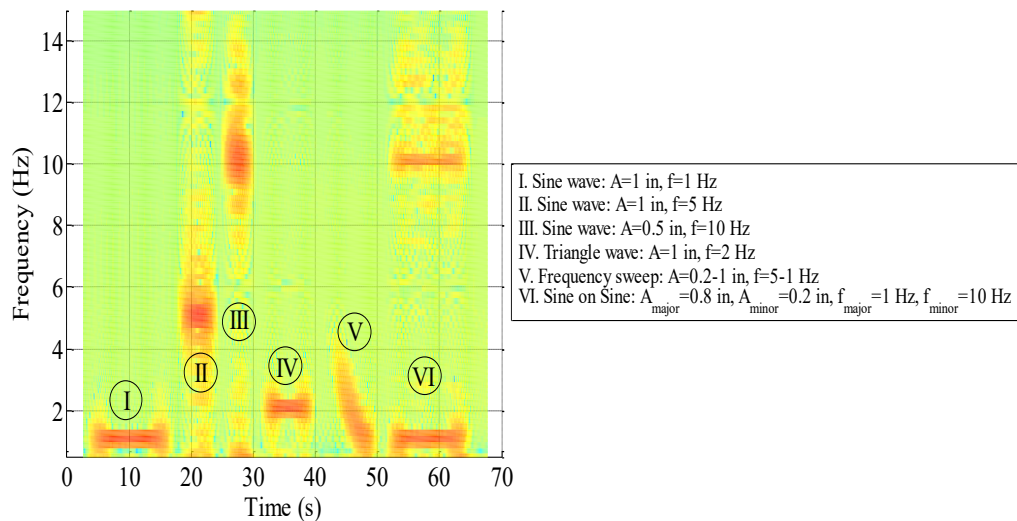


Figure 6-9. STFT (short-time Fourier transform) of LIDAR velocity measurements for a series of large amplitude vertical vibrations. The specifications of the six simulated waveforms are listed in the table on the right.

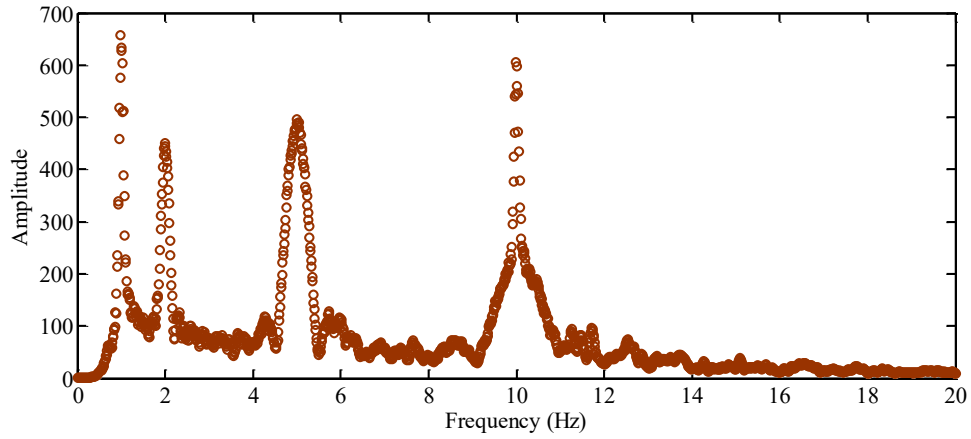
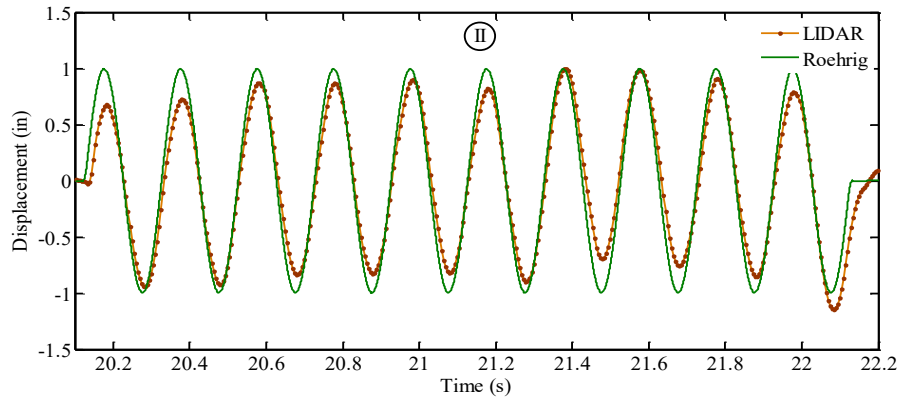
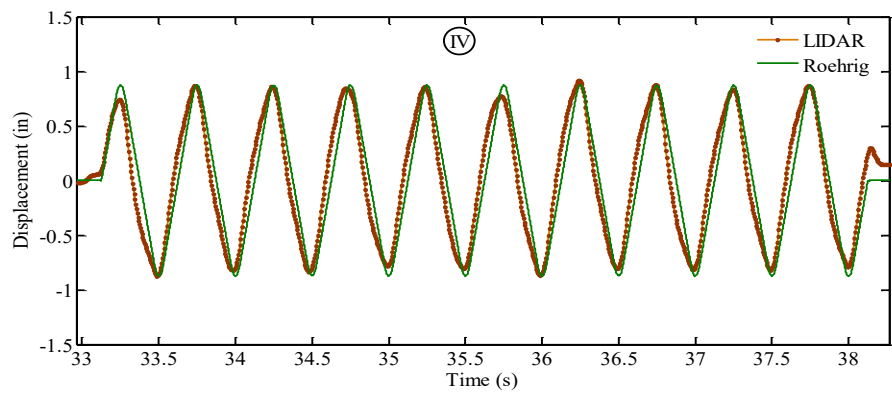


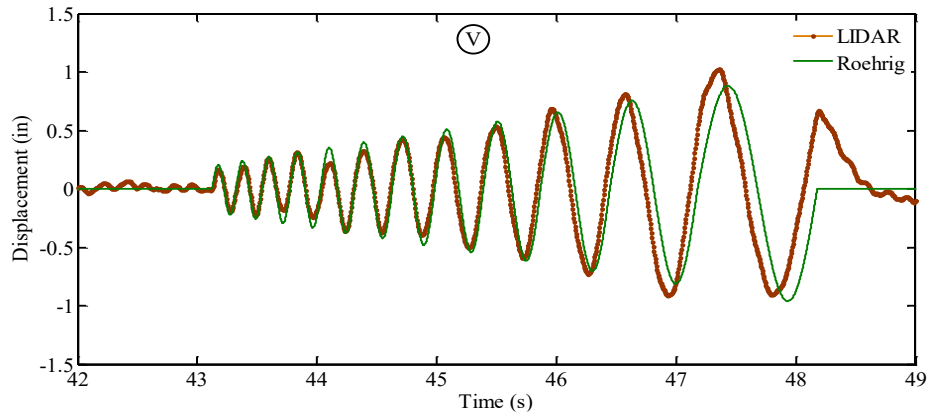
Figure 6-10. FFT response of LIDAR velocity measurement for the large amplitude vibrations depicted in Figure 6-9.



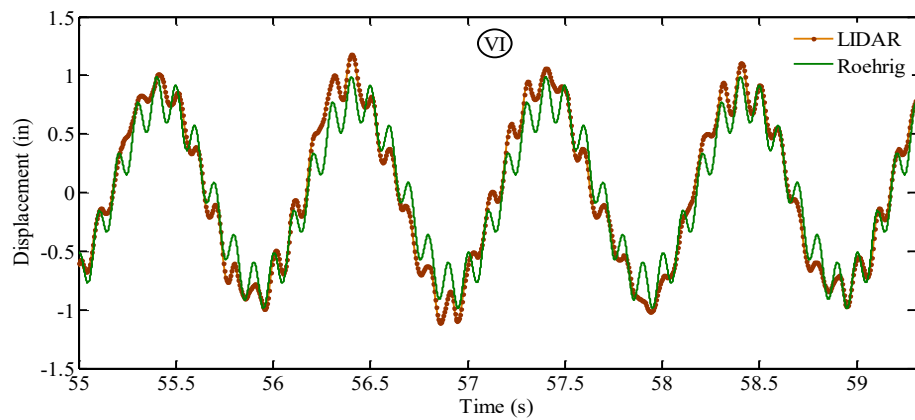
(a) 5 Hz sine wave



(b) 2 Hz triangle wave



(c) Frequency sweep



(d) Sine on sine wave

Figure 6-11. Displacement trajectories derived from LIDAR speed measurements are compared with four large amplitude excitation waveforms (as depicted in Figure 6-9) applied by the Roehrig actuator.

6.3.5 Velocity linearity and accuracy assessment

As shown in the last figure, there is a high correlation between LIDAR and Roehrig speed outputs. As an example, the correlation coefficient for the speed measurements shown in Figure 6-12 is 0.993. This remarkable level of correlation determines the applicability of the proposed approach in the detection of oscillatory speed from LIDAR speed data. It's worth noting that accuracy of the recorded speed data is strongly dependent on the sampling rate and data averaging performed by the LIDAR processor to produce the data output. Linearity of the velocity measurements depicted in Figure 6-12 is studied and plotted in Figure 6-13. According to the linear regression, there is 98% linearity in velocity measurements.

Theoretically, linearity should be $(1-1/FFT)$, which is 99.6% for this set of LIDAR measurements.

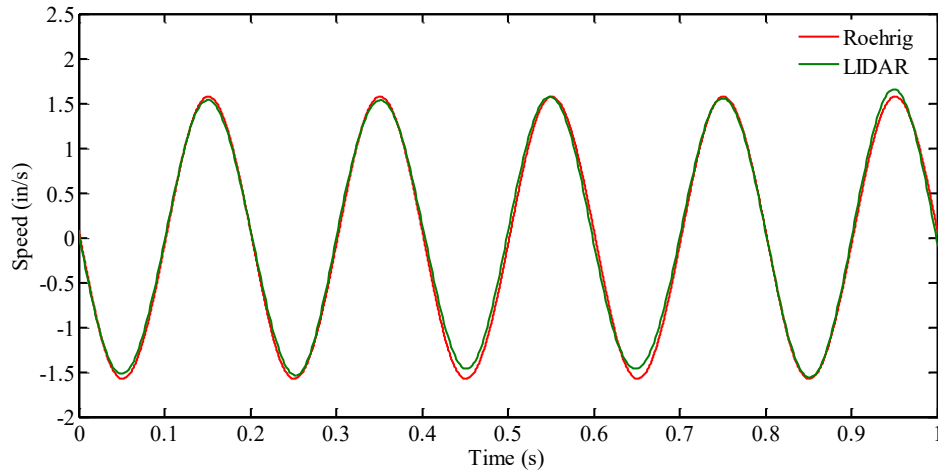


Figure 6-12. Oscillatory speed measurement for a sinusoidal displacement excitation with amplitude of $A=0.1$ in and frequency of $f=5$ Hz with the purpose of correlation analysis. Correlation coefficient is 0.993.

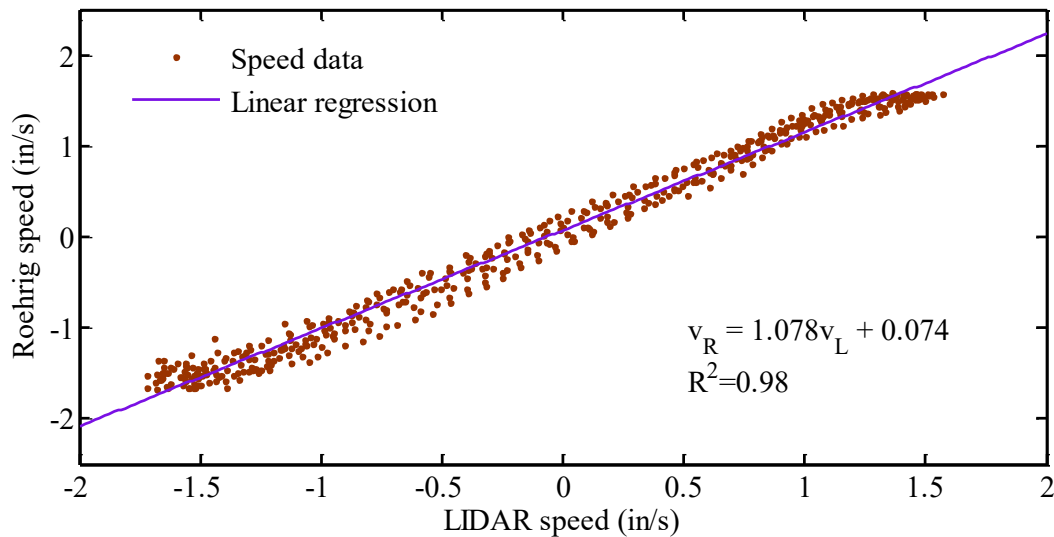


Figure 6-13. Roehrig speed recording vs. LIDAR speed measurement for the sinusoidal excitation shown in Figure 6-12. The slope of linear regression is expected to be 1.

6.3.6 Surface figure effect

A rough surface scatters more light, increasing the intensity of the returned signal, but an even surface scatters less light and decreases the received signal intensity. Despite the

changes in intensity, measured velocity remains unchanged since the measurement is only a function of Doppler frequency shift and not the signal intensity. For the LIDAR to be applicable for track measurements, it should be able to detect vibrations on polished surfaces. The effect of surface figure is studied in Figure 6-14, in which LIDAR measurements on a polished surface and a coarse surface are compared. Beams on a polished surface still scatter light due to the difference in the index of refraction between the air and the surface.

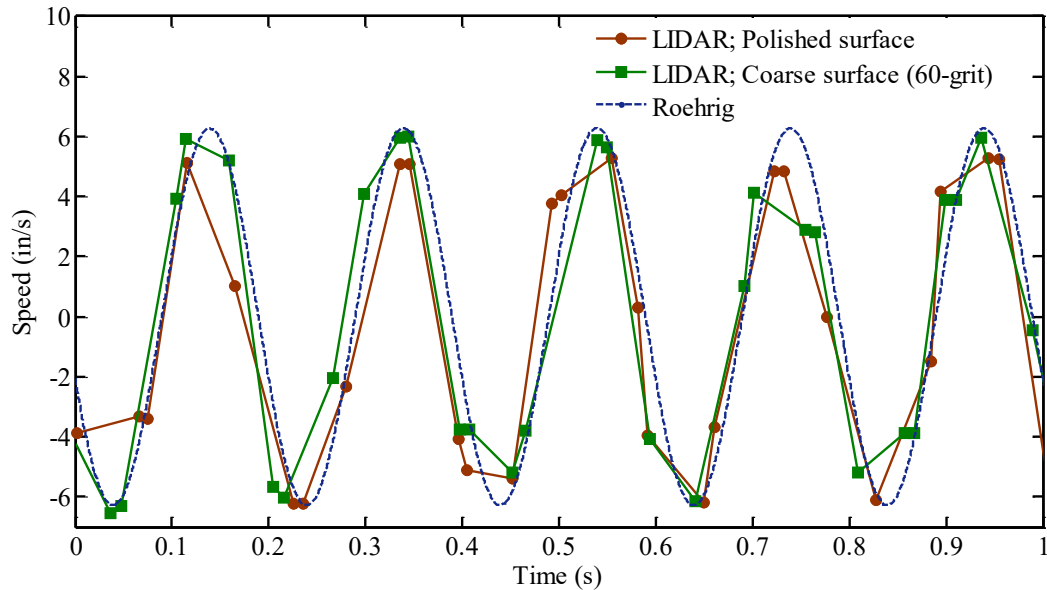


Figure 6-14. Effect of surface figure on the LIDAR speed measurement is investigated for a sinusoidal displacement excitation with amplitude of $A=0.2$ in and frequency of $f=5$ Hz. The rotary disk is polished as it is, and a stick-on 60-grit sandpaper is used to create a coarse surface figure.

6.3.7 LIDAR velocity self-normalizing and infrastructure detection

LIDAR velocity data can be used to detect and assess the track infrastructure elements. These elements include crossings, frogs, switches, and rail joints. LIDAR velocity measurement, when normalized by its driving velocity component (also referred to as off-set speed in this paper), provides an index for track vibration. Each element causes a distinct track deformation, which results in a specific spatial signature in the velocity index. This signature is independent of the train speed and can be used to evaluate the stability and health

condition of the infrastructure element, as well as its location and class. Although extensive field-tests are required to thoroughly collect, identify, and classify the track infrastructure LIDAR signatures, preliminary tests are conducted in RTL to investigate the applicability of the proposed approach.

Let's consider an infrastructure component with the deformation signature, which has the wavelength of 2 ft and the peak displacement of 2 in, as shown in Figure 6-15. This displacement profile is vertically applied to the rotary disk by the Roehrig actuator. The disk is rotated at four different speeds, causing linear speeds of 5.2 ft/s, 7.13 ft/s, 12.5 ft/s, and 17.75 ft/s at the measuring point. LIDAR speed data is then normalized by its offset velocity ($\frac{V_m}{v_x}$) to produce the signature index signal. The index signals are plotted in Figure 6-16 for

the different driving speeds. Although the signature is clearly captured at all speeds, it is necessary to investigate its uniformity. A signature must be uniform and consistent at different speeds. Maximum values of the normalized speeds are plotted versus their associated off-set speeds in Figure 6-17. Indicated by the linear regression, a maximum value of 1.1 is detected for the simulated signature at different driving speeds.¹

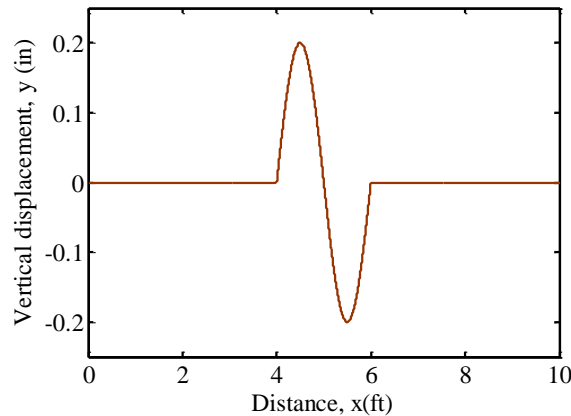


Figure 6-15. The displacement profile simulated by the Roehrig actuator as an example of infrastructure spatial signature.

¹ Theoretically, the peak value of the normalized speed caused by a sinusoidal excitation is calculated

$$\text{as } \frac{V_m}{v_x} = \frac{2\pi A + \lambda}{\lambda} \text{ where } A \text{ and } \lambda \text{ are the displacement amplitude and wavelength of the}$$

spatial signature.

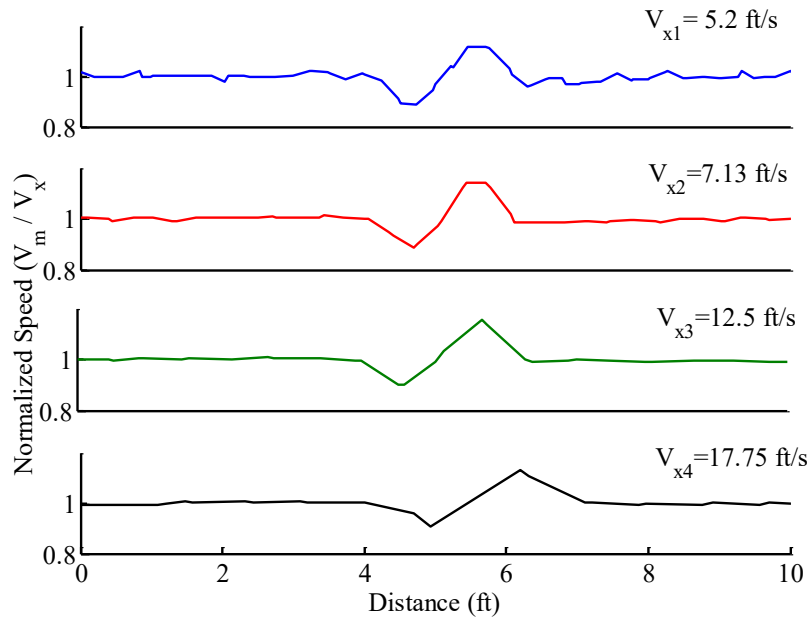


Figure 6-16. Normalized LIDAR speed plots for four different driving speeds, while a displacement signature waveform (Figure 6-15) is applied to the rotary disk.

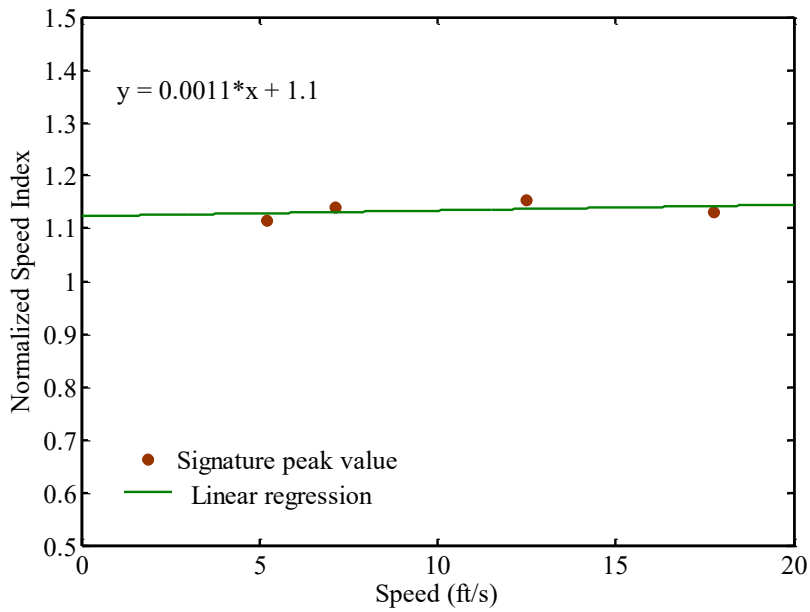


Figure 6-17. Peak values of the normalized speeds (Figure 6-16) as a function of off-set driving speeds. Linear regression shows that the simulated signature can be detected by a peak index of 1.1.

Chapter 7 Track Quality Evaluation and Prediction using LIDAR technology

A length-based track quality index (TQI) is established based on the speed measurements made by Virginia Tech's Light Detection and Ranging (LIDAR) system. The LIDAR system is capable of synchronously measuring the vehicle driving speed and track geometry variations, which offers LIDAR the capacity to derive TQIs in real-time. A novel data aligning method is used to spatially correlate the LIDAR track data with a reference spatial data. The newly-developed TQIs, when computed for the correct location of the track (using the proposed aligning approach), aid in the evaluation of track geometry measurements and track degradation. Based on the characteristics of changes in TQI, a novel track quality deterioration modelling technique is also developed. Degradation fraction is introduced to determine the extent of track deterioration, and maintenance events are modelled as drops in TQI. Equations are proposed to link the degradation fraction and TQI. Numerical studies show that the model can successfully predict the characteristics of TQIs.

7.1 Track Segmentation

The LIDAR system collects and outputs the track information in time domain. For the measurements to be beneficial for track administrators, LIDAR data must be located along the railroad. A new data aligning method is used to spatially correlate the LIDAR track geometry data with a reference spatial data. This approach is inspired by a data aligning method described in U.S. Pat. NO. 6,804,621.

The aligning method is shown in Figure 7-1. It includes steps for (a) obtaining signature track data in spatial domain for use as reference data; (b) constructing the LIDAR signature data in spatial domain to be aligned; (c) dividing the LIDAR track data into spatial segments; (d) comparing the reference data to the measured track data segments to identify the location of

segments; and (e) stretching/shrinking the LIDAR data to account for local deviation in calibration value(s).

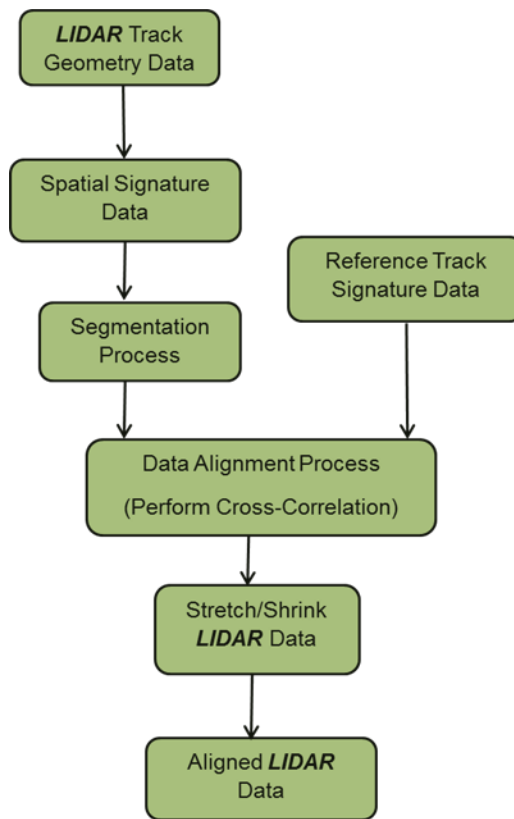


Figure 7-1. LIDAR data aligning algorithm; LIDAR spatial data is divided into segments of signature data to be aligned with a set of reference data.

The alignment signature can be any spatial data such as curvature data or crossing locations. However, it is important to choose a signature that can be captured repeatedly and constantly by the LIDAR system. Track curvature is readily distinguishable by the Doppler-based sensors; thus it is believed to be the most appropriate signature. The reference data must include the signature measurement. It can be either an old aligned set of LIDAR data, or the data collected by another monitoring unit. The segmentation process prepares the measured data for the aligning process. Each segment must contain at least one specific signature (i.e. curve). However, constraint shall also be applied on the length of segments if necessary.

7.2 LIDAR's Track Quality Index

A length-based TQI, inspired by the research conducted by El-Sibaie and Zhang [23], is adopted for the LIDAR. The LIDAR system is capable of synchronously measuring the vehicle driving speed and track geometry variations. This offers LIDAR the capacity to derive TQIs in real-time. Track is first divided into equal length segments (L_0) using the extracted driving speed. The overall LIDAR velocity measurement is then used to calculate the traced length L_s . For each segment, traced length is greater than the length of the segment since the overall LIDAR velocity is the sum of driving speed and the rate of track geometry variation. TQI is an explicit function of spatial resolution (Δx), and is defined as:

$$TQI(\Delta x, L_0) = \left(\frac{L_s}{L_0} - 1\right) \times 10^3 \quad (7-1)$$

where L_s is the traced length of space curve (ft), and L_0 is the fixed length of track segment (ft). These parameters are depicted in Figure 7-2 for lateral and vertical track irregularities.

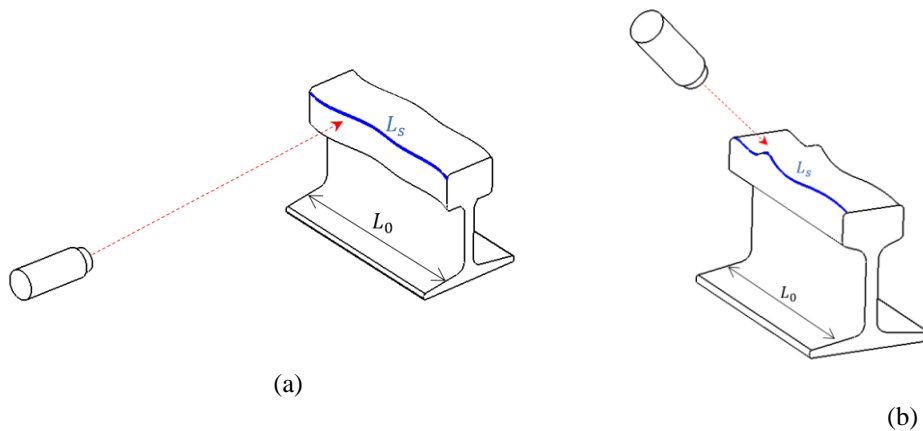


Figure 7-2. Schematic description of the length-based TQI measured by the LIDAR system for: (a) lateral irregularities, (b) vertical irregularities.

The proposed procedure for the calculation of track quality alignments (TQAs) is shown in Figure 7-3. The recorded raw velocities (V_{mR} and V_{mL}) contain both the vehicle forward speed and rail lateral irregularity variation. These velocities, when integrated, yield the traced

lengths of the section (L_{sR} and L_{sL}). Fixed lengths (L_{0R} and L_{0L}) are computed using the forward driving speeds (V_R and V_L). When extracting these velocity components, it is necessary to filter the raw data by the appropriate Nyquist frequency. By applying a low-pass filter, any information above the cut-off frequency of the filter (including the rail lateral displacement velocity) will be lost within this process. It is worth mentioning that the same method is applicable to gage and profile indices (TQG and TQP).

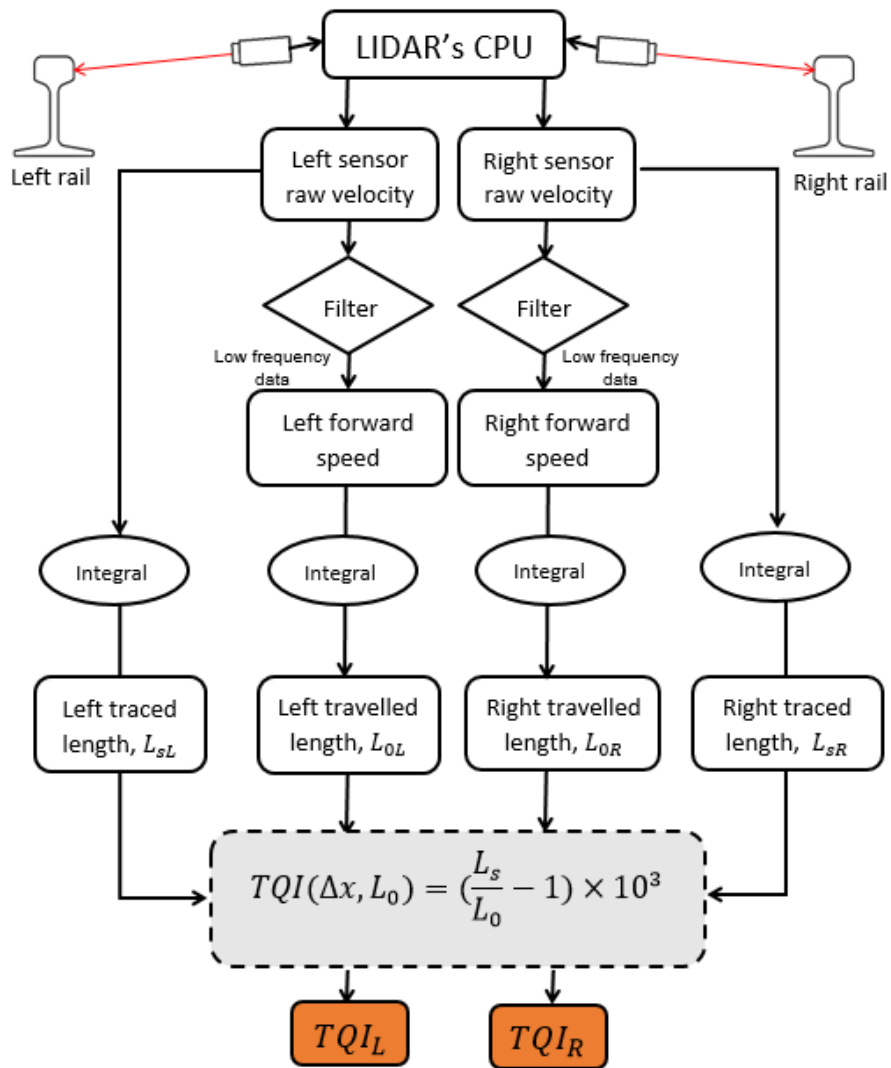


Figure 7-3. Calculation procedure of track quality alignment indices using the LIDAR system.

As mentioned earlier, TQI is an explicit function of the spatial resolution. Therefore, the capacity of TQI to capture track irregularities is largely dependent on the wavelength of the defects. The change in spatial resolution as a function of forward velocity for three given sampling rates is shown in Figure 7-4. As expected, increasing the sampling rate improves the sampling resolution. The range of spatial resolutions for various surveying speeds can also be extracted from this information. For instance, at an average walking speed of 3 mph, the spatial resolution varies between 0.04 ft and 0.09 ft, while at an average metrology car speed of 45 mph, the range of spatial resolution is from 0.5 ft to 1.3 ft.

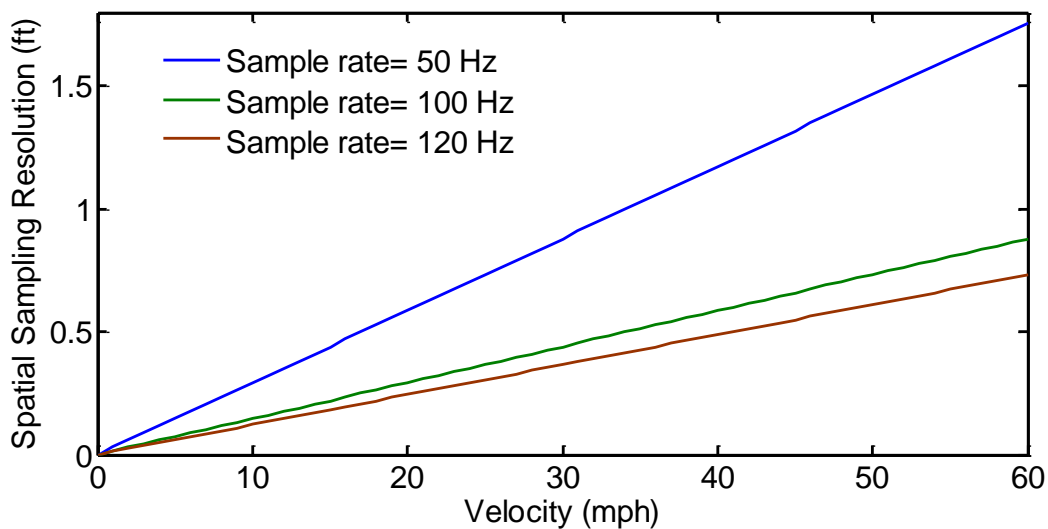


Figure 7-4. Spatial sampling resolution as a function of forward velocity for three given sampling rates.

7.3 Degradation Modeling

The modelling approach presented here is based upon the phenomenological behavior of a TQI depicted in Figure 7-5. The blue line shows the characteristic degradation of a track quality without maintenance. As explained in [9], an immediate deterioration occurs upon completion of renewal operation due to the initial settlements of the track. Since this period is quite short, it is common to disregard it in the analyses. In this work, this mode period is assumed to have a constant deterioration rate of D_a . The dominant deterioration period starts once the track is sufficiently stabilized, which is represented by the point when TQI

reaches Q_s . This phase of degradation occurs during most of the track's lifetime, and ends when TQI reaches Q_f . An internal parameter is introduced to numerically represent the state of deterioration for track quality. This parameter is called degradation fraction and varies from zero to one ($0 \leq d \leq 1$). Degradation is assumed to be zero at the beginning of the second phase ($d = 0$ when $Q = Q_s$), and one at the end of this phase ($d = 1$ when $Q = Q_f$). The second phase is followed by another rapid deterioration period, which can eventually lead to track failure. In a normal situation, this phase should never be allowed to happen. The rate of deterioration during this period is assumed constant (D_b).

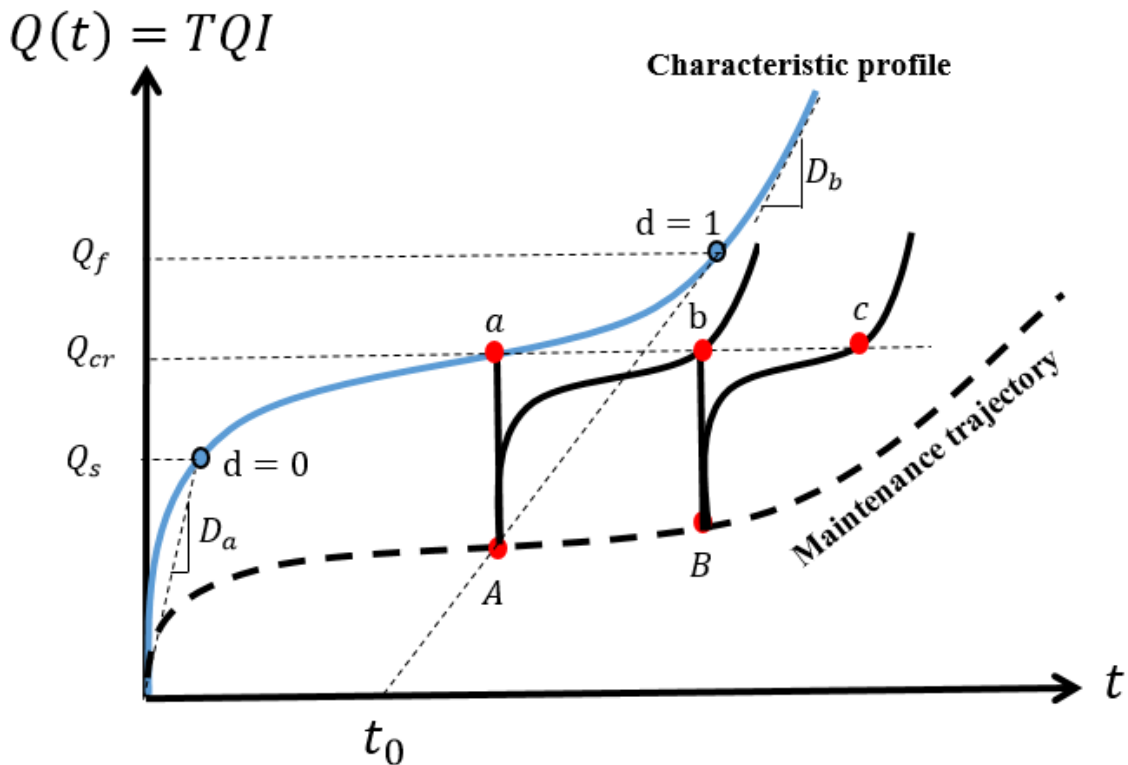


Figure 7-5. Track deterioration and restoration in terms of the Track Quality Index (TQI)

This model starts with the following classic fundamental equation:

$$t = \frac{Q(t)}{D(d)} + d(t)t_0 f(m) \quad (7-2)$$

where t is tonnage, $Q(t)$ is the predicted TQI, $d(t)$ is the degradation fraction, and t_0 is the tonnage accumulated during the second phase of deterioration. Quality tangent $D(d)$ is a function of the degradation fraction as:

$$D(d) = D_a + d(D_b - D_a) \quad (7-3)$$

$f(m)$ in Equation (7-2) determines the effect of maintenance operations on the rate of deterioration. This function is defined as the following exponential form:

$$f(m) = e^{(-mk)} \quad (7-4)$$

where m is the number of maintenance events and k represents the rate of deterioration. The link between the track quality and degradation fraction is called the deterioration rule. The following polynomial relation is assumed as the deterioration rule:

$$Q(t) - Q_s = \mu_1 d(t)^2 + \mu_2 d(t) \quad (7-5)$$

where μ_1 and μ_2 are the constant characteristic parameters. Considering the assumption of $d = 1$ when $Q = Q_f$, the following constraint must be satisfied:

$$\mu_2 = Q_f - Q_s - \mu_1 \quad (7-6)$$

As shown in Figure 7-5, a maintenance operation is followed by a vertical drop in the value of TQI. The amount of this drop depends on the type of maintenance work and track condition. Normally, the amount of vertical drop decreases with an increase in the number of maintenance operations. The vertical quality drop as a function of number of maintenance operations is simply defined as:

$$\Delta q(m) = \Delta q_0 - m\delta \quad (7-7)$$

where Δq is the quality drop, Δq_0 is the initial quality drop, and δ is the rate of change in quality drop.

7.4 Results and Discussion

7.4.1 LIDAR data correlation

The proposed alignment approach is evaluated over 12 miles of track, and IMU curvature is used as track reference data. Three LIDAR segments of different random lengths are constructed for the purpose of alignment, as depicted in Figure 7-6. The first segment contains a right curve in about 2 miles of the track. The second segment has two curves, including one right and one left curve over 1.5 miles. Segment 3 includes four curves of various radii. These three segments are successfully correlated with the IMU data, as shown in Figure 7-7.

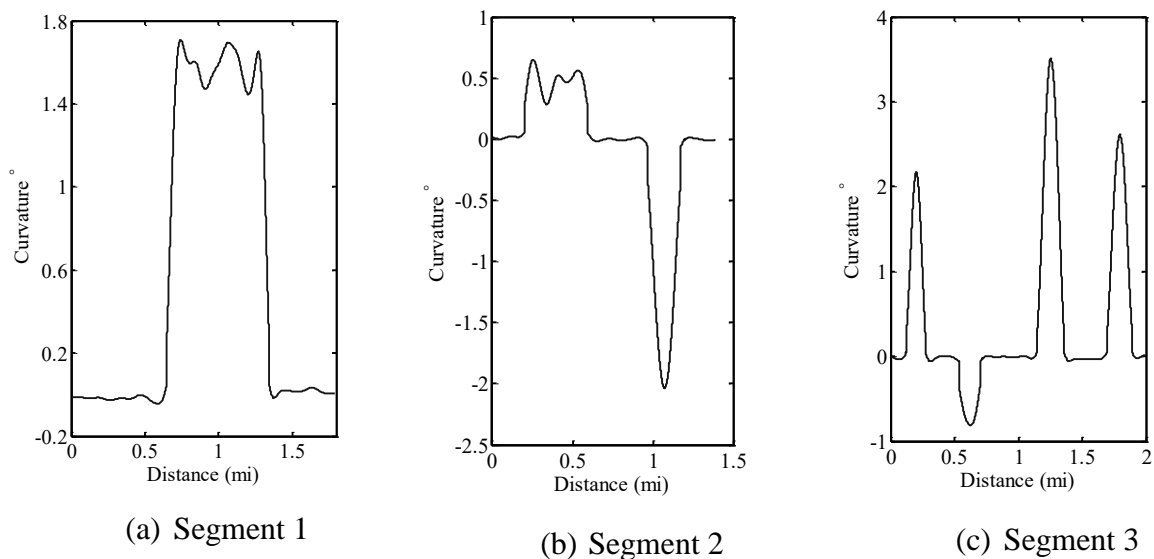


Figure 7-6. LIDAR spatial segments of various lengths and different number of curves.

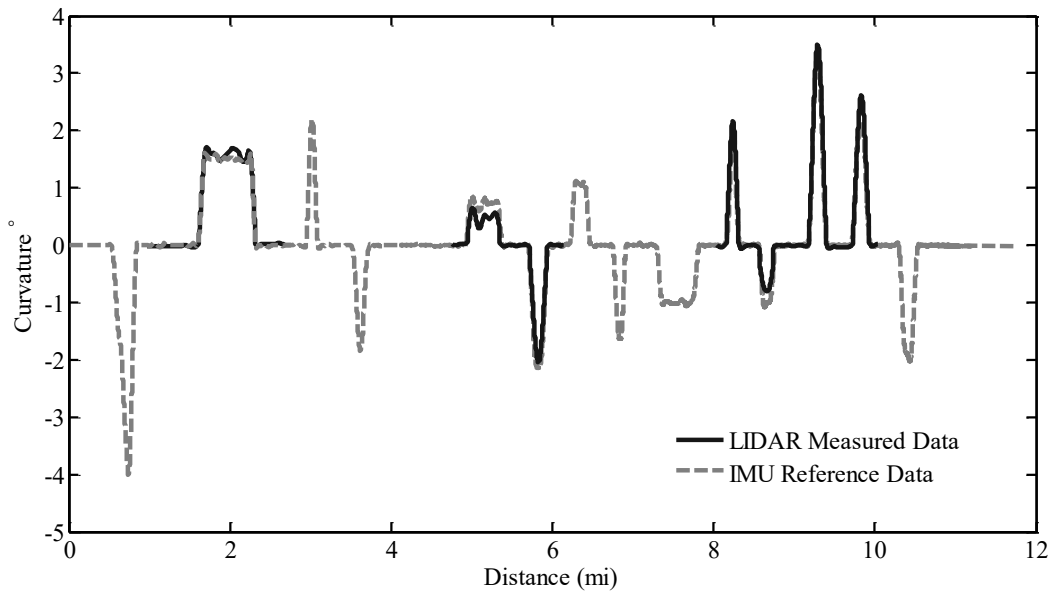


Figure 7-7. Alignment of LIDAR curvature segments with IMU reference data.

7.4.2 TQI results

Inertial measurement unit (IMU) geometry data was collected simultaneous to LIDAR measurements. Figure 7-8 and Figure 7-9 show left and right alignments made by LIDAR and IMU systems over 0.5 mi of the track. As expected, exact spatial correlation between the two measurements is not achieved due to different asynchronous measuring and calculation techniques. It is not possible to compute the length-based TQIs (Equation (7-1)) for the IMU data and compare them with LIDAR's TQIs. However, comparing the standard deviations of the two measurements is a suitable evaluation tool since it also represents the extent of irregularity. Figure 7-10 and Figure 7-11 show the standard deviation distribution of the LIDAR and IMU left and right alignment measurements calculated over 1000-ft-long segments.

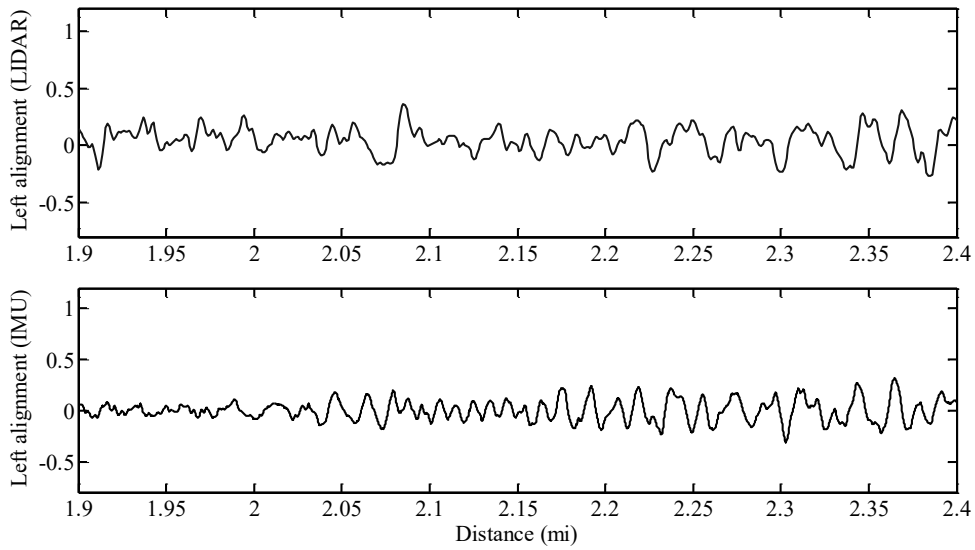


Figure 7-8. Left alignment measurements made by the LIDAR system and IMU for a 0.5 mi section of the track.

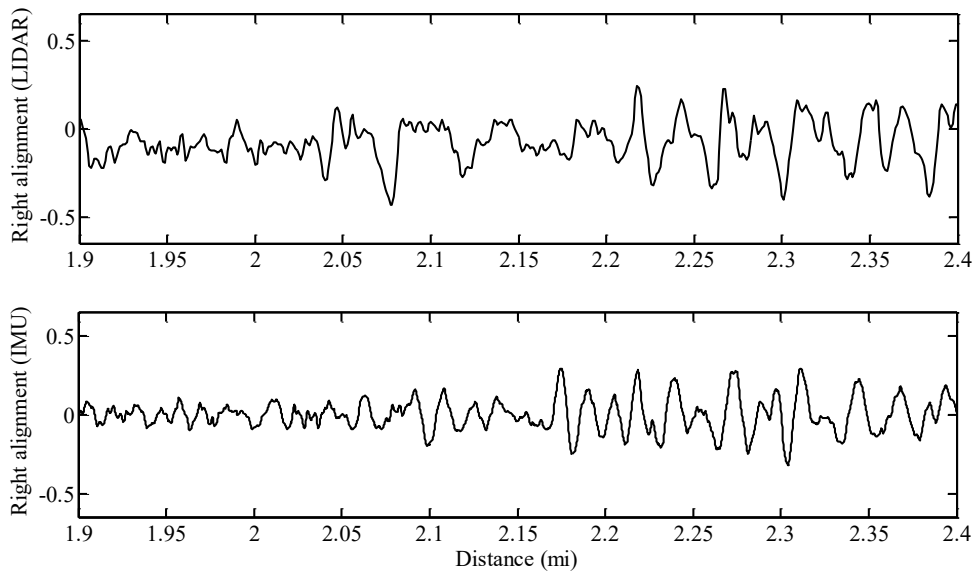


Figure 7-9. Right alignment measurements made by the LIDAR system and IMU for a 0.5 mi section of the track.

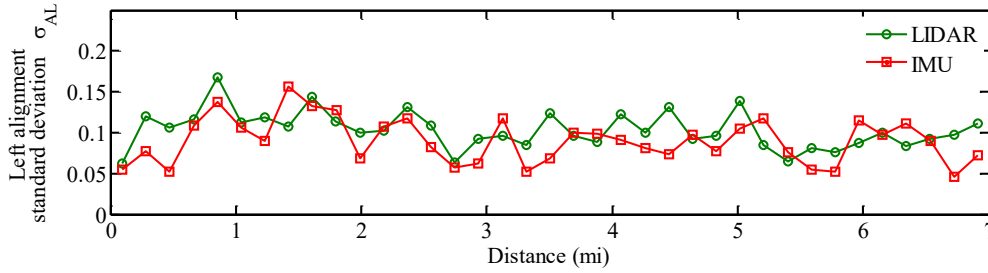


Figure 7-10. Standard deviation distribution of LIDAR and IMU left alignment measurements calculated over 1000-ft segments.

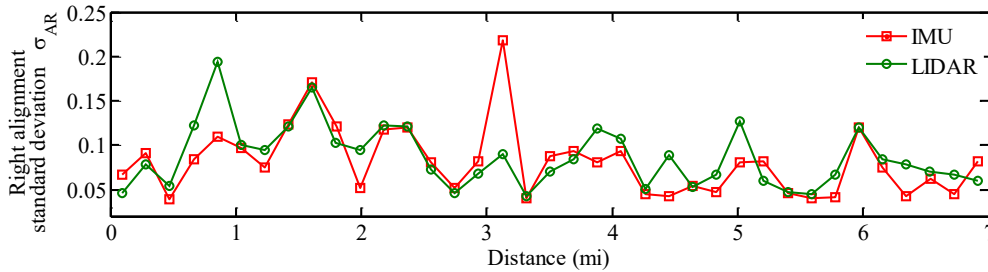


Figure 7-11. Standard deviation distribution of LIDAR and IMU right alignment measurements calculated over 1000-ft segments.

For the purpose of this research, L_0 is fixed at 1000 ft. This is an arbitrary value and shall be altered to achieve desired number and length of segments. TQIs are computed for lateral geometry parameters, including left alignment (TQA_L) and right alignment (TQA_R). These indices are plotted in Figure 7-12 and Figure 7-13 for 7 miles of track. Normally, when assessing the quality of track, a threshold is set on the mean value of TQI. When TQI of a unit section is above this threshold, the section has to be taken into consideration for planning track maintenance.

It is well-established that TQI mean value is different for different track classes and features [23]. Thus, TQI can potentially serve as a locator for track features such as tunnels, bridges, switches, curves, and tangents in addition to monitoring the track quality. As an example, Figure 7-14 shows the left alignment index (TQA_L) for curved and tangent segments. These segments are decoupled based on LIDAR’s curvature measurements.

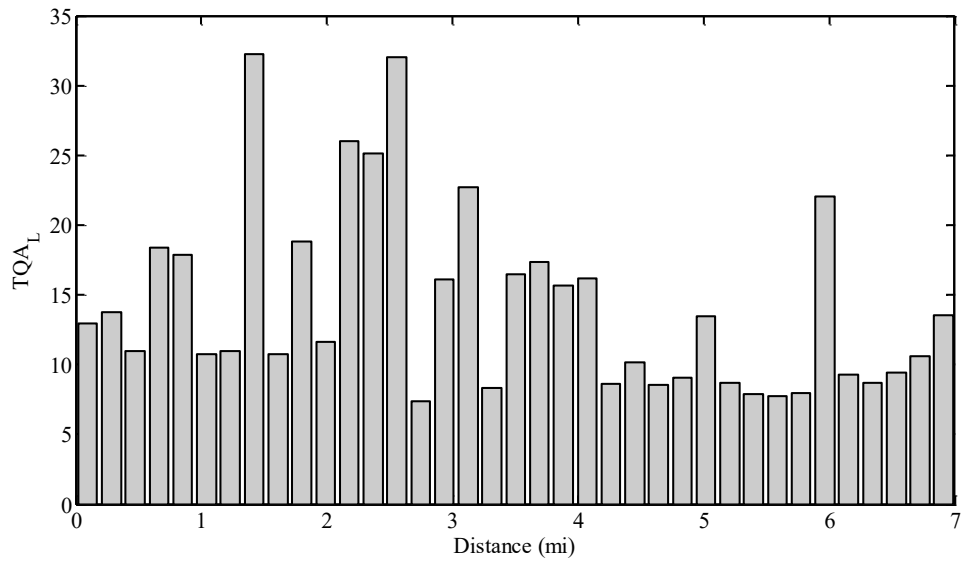


Figure 7-12. LIDAR's track quality left alignment index calculated over 1000-ft segments.

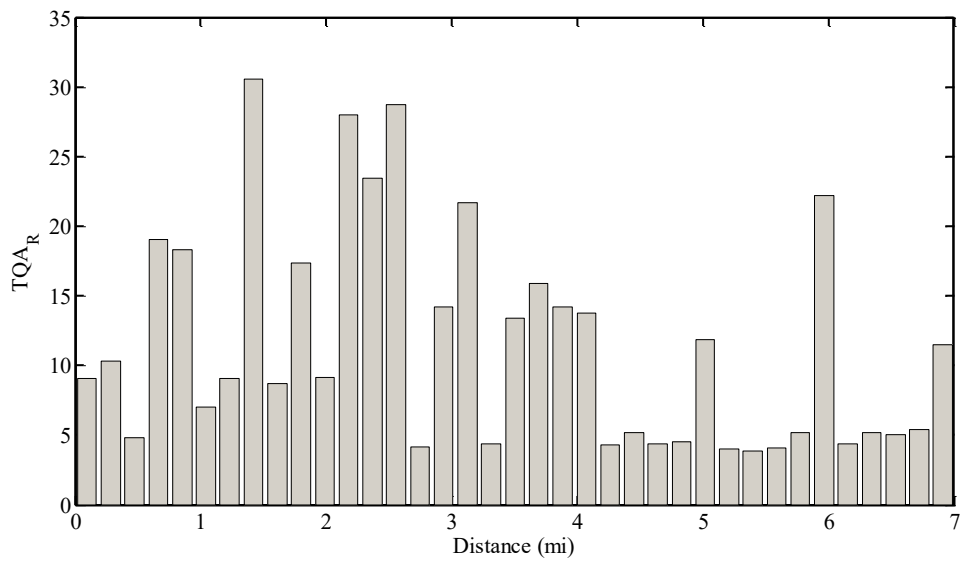


Figure 7-13. LIDAR's track quality right alignment index calculated over 1000-ft segments.

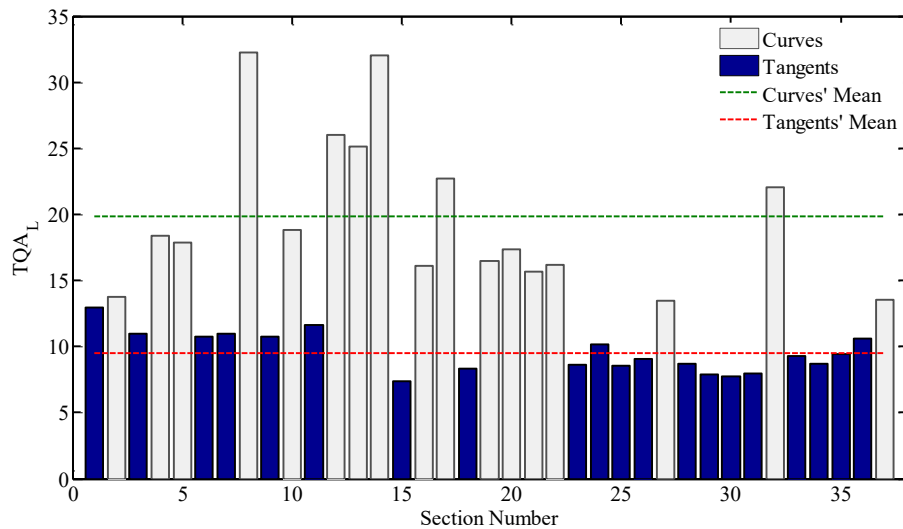


Figure 7-14. LIDAR's track quality left alignment index calculated over 1000-ft segments. Curved and tangent segments are decoupled.

7.4.3 Numerical example of model application

Since adequate experimental LIDAR TQI data is not available, a numerical study is performed to study the application of the proposed degradation model. An arbitrary set of model properties is adopted (as listed in Table 7-1), and quality degradation is predicted for a segment of track with the TQI threshold of $Q_{cr} = 35$ during 300 MGT. Figure 7-15 shows the predicted TQI. Vertical drops in this plot represent the maintenance events. As discussed above, changes in TQI correspond to those in degradation fraction d . The predicted response of d during 300 MGT is plotted in Figure 7-16. As expected, degradation fraction drops to zero upon maintenance, and the rate of deterioration increases after each maintenance operation. This leads to a rise in the frequency of maintenance, as clearly shown in Figure 7-17. The LIDAR measurements can be used to generate TQI maps for long corridors. For instance, Figure 7-18 shows the prediction of TQI for 3000 ft of track with 100-ft-long sections with random initial track quality.

Table 7-1-Model parameters used for the numerical evaluation of the proposed degradation model

PARAMETER	VALUE	PARAMETER	VALUE	PARAMETER	VALUE
Q_s	15	D_b	1.2	k	0.2
Q_f	50	t^*	80 MGT	δ	2
D_a	1	μ_1	2	Δq_0	32

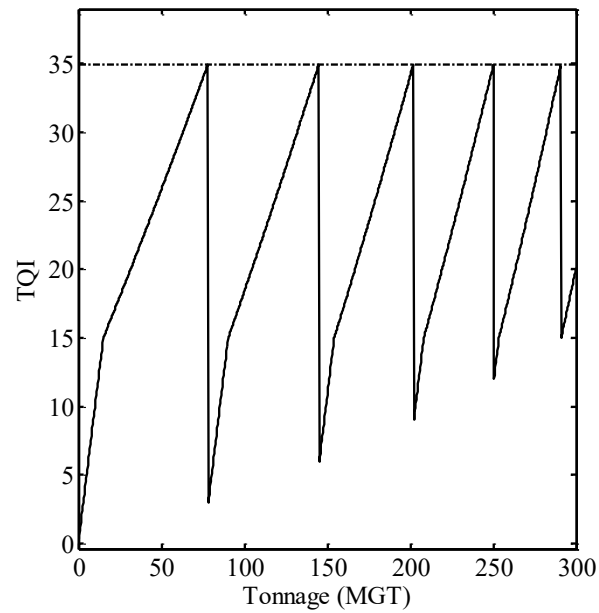


Figure 7-15. Prediction of TQI for a segment with the critical quality of $Q_{cr} = 35$ and 5 maintenance operations.

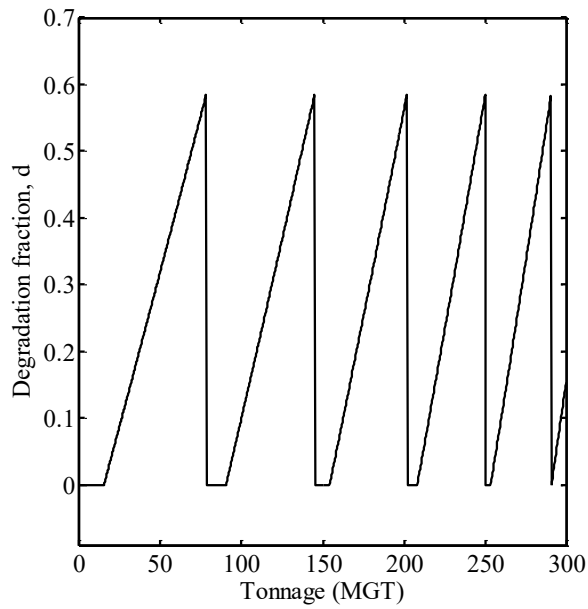


Figure 7-16. Prediction of degradation fraction (d) for a segment with the critical quality of $Q_{cr} = 35$ and 5 maintenance operations.

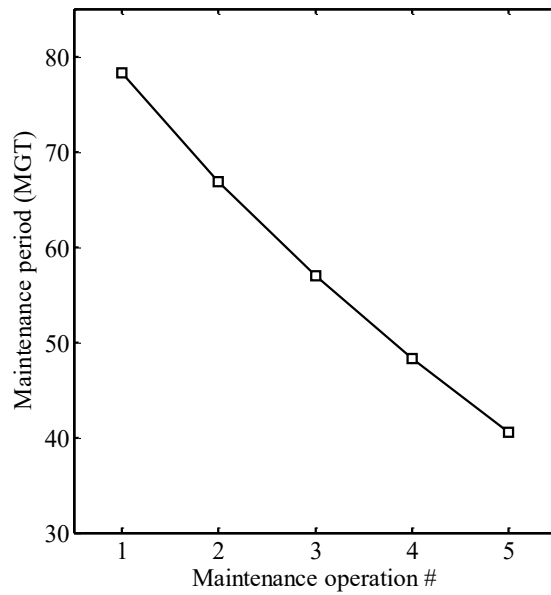


Figure 7-17. Prediction of reduction in the maintenance period as a function of maintenance operation number.

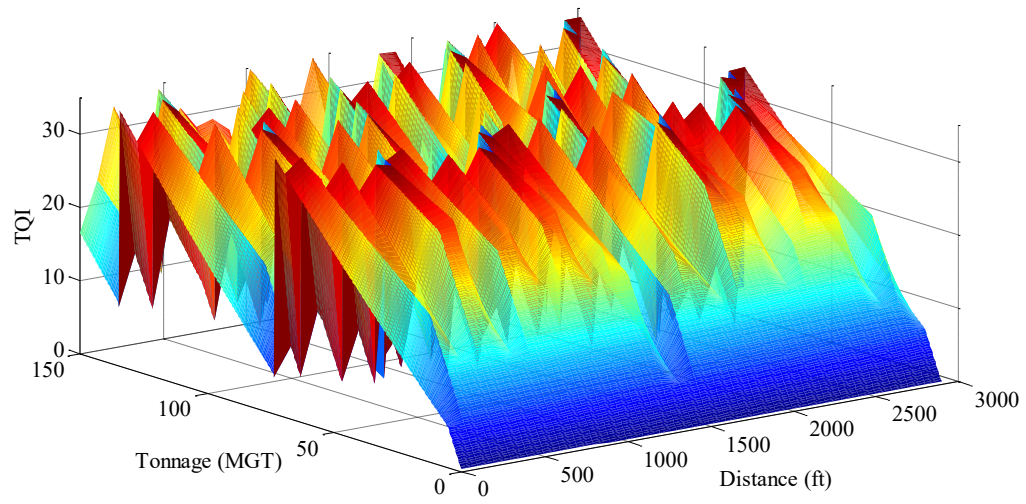


Figure 7-18. Prediction of TQI for 3000 ft of track with 100-ft-long sections (critical quality, $Q_{cr} = 35$).

Chapter 8 Application of LIDAR Technology for Rail Surface and Structural Integrity Monitoring

LIDAR applications in railroads are not limited to track speed, curvature, and track geometry measurements. A LIDAR system can also be used to monitor the rail surface structure and integrity. This is possible due to the fact that the Doppler shift on the LIDAR beam reflected from a moving surface has the Doppler bandwidth broadened in proportion to the height and width of the surface features. The relative spectral intensity of the collected LIDAR beam is also proportional to the scattering properties of the surface material. Therefore, Doppler bandwidth and laser intensity information can be used to detect different rail surface materials and conditions, including roughness, rail lubrication, Top of the Rail (ToR) friction modifiers, and leaf residues.

The LIDAR rail surface measurements may be further used to derive surface parameters such as friction, rail/wheel lubricity, and rail infrastructure integrity [50]. Additionally, the velocity signatures (as introduced in Chapter 6) may be used to simultaneously evaluate vehicle or surface dynamics and rail feature spectral characteristics.

8.1 LIDAR-based Rail Surface Feature Aspect Ratio

The bandwidth of a Doppler signal scattered from a moving surface is proportional to the forward velocity of the surface and the inherent geometric factors of the surface materials. The ratio of Doppler bandwidth to center frequency is characteristic of the surface geometry and material. In a Doppler shift spectrum, the Doppler shift frequency bandwidth is represented by the frequency (or velocity) range at half of the maximum spectral intensity ($0.5 I_m$). This frequency range is called Full Width at Half Maximum (FWHM) and is labelled on the Doppler shift spectrum plotted in Figure 8-1. Since FWHM is a speed variant parameter, it is normalized by the center velocity (V_c) to generate a speed-independent rail surface measure. This LIDAR-based Rail Surface Feature (RSF) ratio is defined as:

$$RSF = \frac{FWHM}{V_c} \quad (8-1)$$

For a given material representation, RSF ratio is believed to be a unique indicator of its surface material, integrity, and roughness.

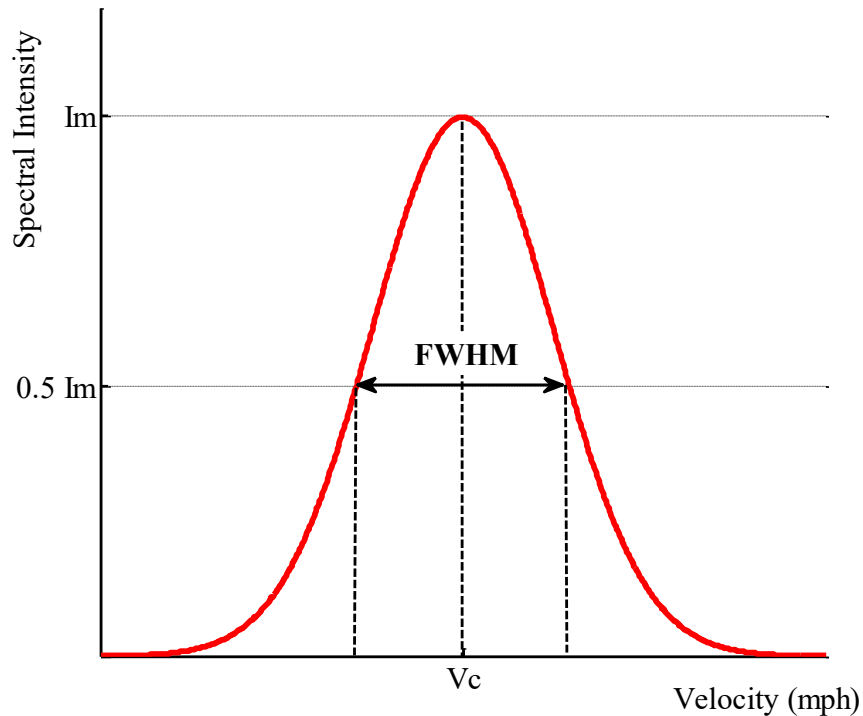


Figure 8-1. Doppler shift spectrum determines center Doppler velocity (V_c), collected LIDAR frequency bandwidth (FWHM), and maximum laser spectral intensity (I_m).

8.2 LIDAR Intensity Ratio

In addition to Doppler shift bandwidth, the spectral intensity of the received LIDAR beam is also affected by the surface condition. LIDAR Intensity Ratio (LIR) is defined as the ratio of the relative Doppler spectral intensity (I_m) to the center velocity (V_c), normalized by a reference intensity measure, (R_I) as:

$$LIR = R_I^{-1} \frac{I_m}{V_c} \quad (8-2)$$

where R_I is the reference surface intensity measure. LIR determines the relative scattering properties of the scanned surface with respect to a reference surface, independent of the forward speed. The value of LIR represents the extent of energy received by the LIDAR sensor through scattering.

For the rail surface monitoring application, the dry bare rail is selected as the reference surface and R_I is defined as:

$$R_I = \frac{I_r}{V_r} \quad (8-3)$$

where I_r is the relative Doppler intensity collected off the bare rail, and V_r is the forward velocity at which I_r is measured. Any deviation from the LIR value of the bare rail determines the variation in scattering characteristics of the surface material (or coating) with respect to the bare rail.

RSF and LIR computations are dependent on the LIDAR sensor orientation and focal distance, since they are extracted from the Doppler shift spectra. For a fixed LIDAR configuration, however, RSF and LIR are unique indicators of the surface material, and they can be used to detect and assess specific coatings and surface conditions.

Before implementation for rail monitoring, the system needs to be calibrated for the expected track surface conditions and rail coating situations. The calibration results will establish the necessary baselines required to identify and evaluate the field scanning RSF and LIR data. This technique allows for the rapid assessment of the rail surface and provides rail condition information for further maintenance operations.

8.3 Preliminary Testing and Technology Demonstration

Laboratory-scaled tests are conducted to demonstrate the feasibility of the introduced LIDAR-based approach for rail surface monitoring and evaluation. For this demonstration effort, the RTL rail panel is divided into two sections of 5ft, which are separated by a reflective tape, as shown in Figure 8-2. LIDAR optics are mounted to the RTL rail trolley (Figure 8-3). The rail cart is driven by a remotely-controlled DC motor for a constant speed and consistent data collection. A LIDAR sensor with focal length of 23 in is oriented to target the top of the rail surface, as depicted in Figure 8-4.

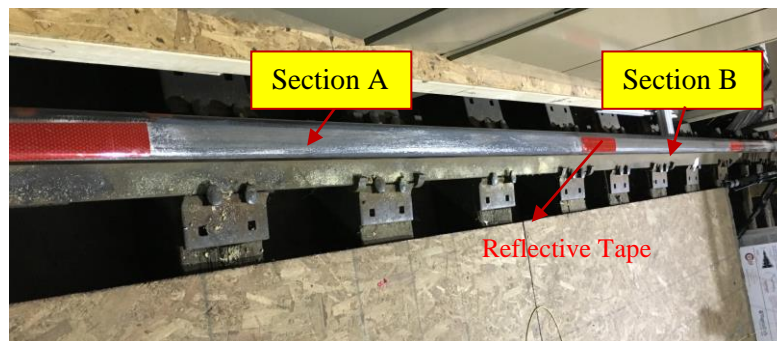


Figure 8-2. RTL rail panel is divided into two sections of 5ft for lab testing. The reflective tape separates the two sections for easier detection of the sections upon data processing.

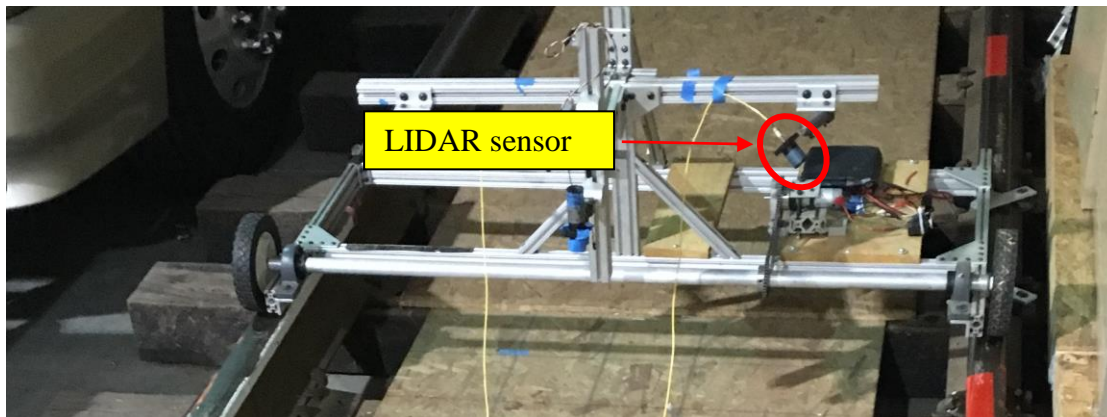


Figure 8-3. LIDAR sensors are mounted to the RTL rail trolley for rail surface feature lab testing. The cart is driven by a remotely-controlled DC motor for a constant speed and consistent data collection.

The marked track sections are coated with different materials, as listed in Table 8-1, to simulate various rail surface conditions. Section B is kept dry in all cases to provide a direct comparison with the coated segment in all five testing configurations. The trolley is then operated over the panel. LIDAR data is outputted at 33 Hz to compute RSF and LIR indices. The LIDAR track speed measurements are used to calculate the traveled distance of the cart. The RSF and LIR values of the coated segments are compared with the bare rail data to identify the surface aspect ratio at different rail conditions. The comparisons are discussed in the following section.

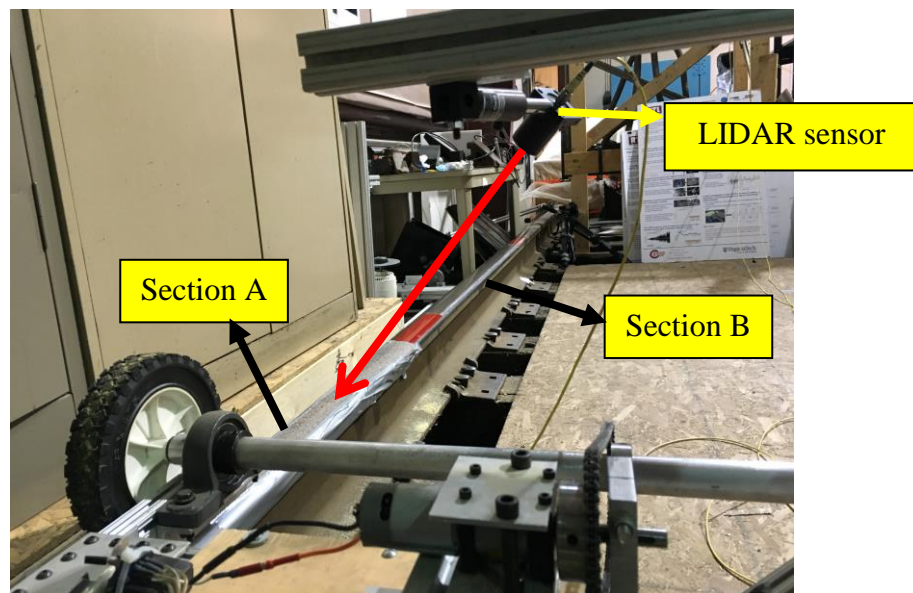


Figure 8-4. LIDAR laser beam targets top of the rail. Section A is coated with different materials and Section B is kept dry.

Table 8-1. The testing protocol designed to evaluate the LIDAR system application for rail surface monitoring.

Test #	Section A coating	Section B coating
1	Bare rail	Bare rail
2	ToR friction modifier	Bare rail
3	Sawdust	Bare rail
4	Coarse sandpaper	Bare rail
5	Coarse sandpaper	Bare rail

8.4 Data Processing and Results

Test 1 is carried out to scan the dry bare rail and establish the baseline for the coating detection. FWHM and track speed (V_c) are needed in order to calculate the RSF ratio. FWHM measurements are plotted in Figure 8-5. A moving average with the window size of 15 data points is applied to the raw FWHM measurements to remove the instantaneous deviations. The averaged vector is also shown in Figure 8-5. The same averaging function is applied to the speed measurements as plotted in Figure 8-6.

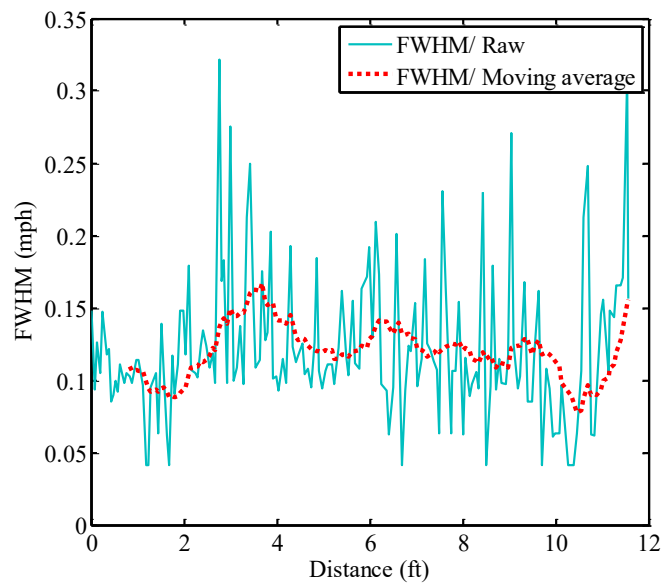


Figure 8-5. LIDAR FWHM measurements collected over bare rail in Test 1. A moving average with a window size of 15 data points is applied to the raw FWHM data.

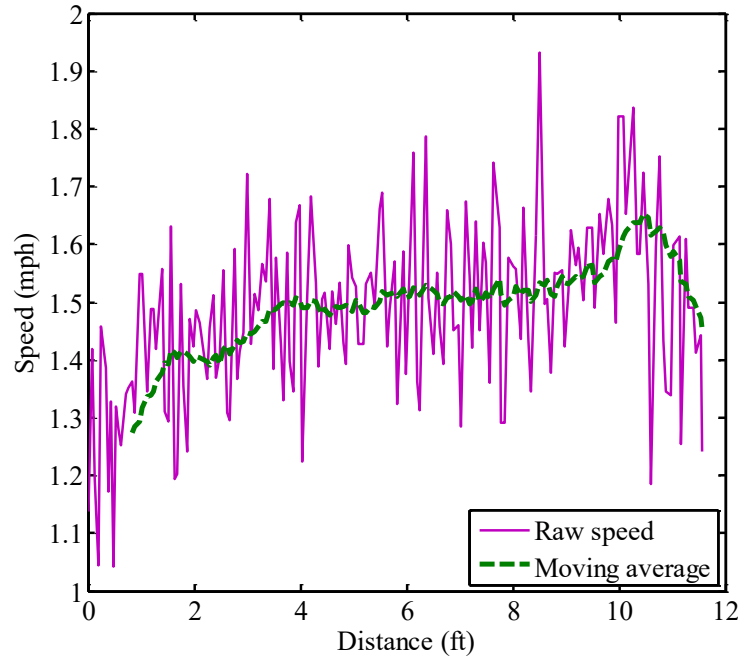


Figure 8-6. LIDAR track speed measurements during Test 1. The average speed of the cart during test was 1.5 mph ($V_r=1.5$ mph).

The averaged FWHM and track speed vectors are then used to calculate the RSF ratio according to Equation (8-1). Figure 8-7 shows the RSF measurements over the bare rail. Although the average RSF ratio is 0.08, there are slight deviations in RSF ratios for the bare rail. These variations are believed to be mainly due the dynamics of the rail trolley, and consequently the changes in the laser point position. Also, the testing track segments are short and they may have some coating residues remaining on the rail from prior surface testing attempts.

LIDAR spectral intensity data collected during Test 1 is plotted versus track distance in Figure 8-8. The average spectral magnitude for Sections A and B are calculated to be 0.15 w/Hz and 0.1 w/Hz, respectively. The average of these two values is used as the bare rail Doppler intensity ($I_r=0.125$ w/Hz) along with the average velocity ($V_r=1.5$ mph) to calculate the reference intensity measure as $R_I=0.057$ w/ft.

Using Equation (8-2) and the designated reference intensity (I_r), LIR is calculated for Sections A and B as depicted in Figure 8-9. Average LIR values calculated for the two sections are slightly different. This deviation might be due to coating residues on the rails

and/or different rail surfacing histories. Due to its substantial reflectivity, the reflective tape yields a significantly large LIR value ($\gg 50$).

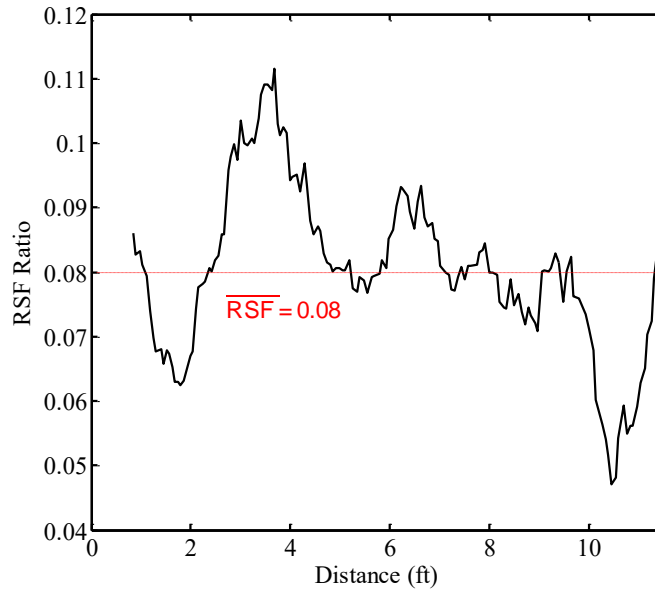


Figure 8-7. RSF measurements for bare rail in Test 1. The average RSF ratio for the dry bare rail is 0.08.

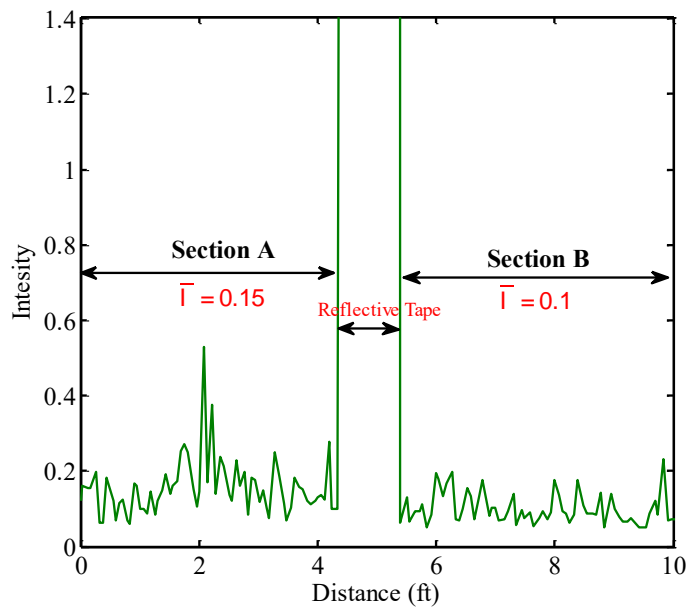


Figure 8-8. LIDAR spectral intensity measurements for bare rail in Test 1. Sections A and B are both dry. The average intensities for Sections A and B are 0.15 and 0.1, respectively.

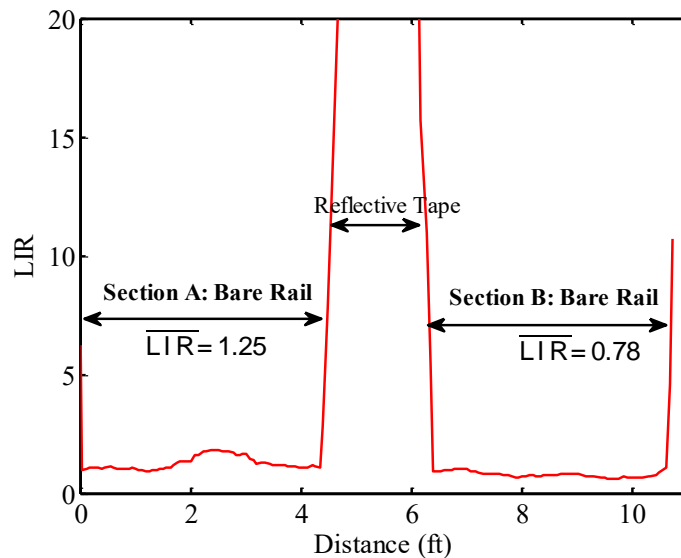


Figure 8-9. LIR measurements for bare rail in Test 1. The reference intensity (RI) is calculated from the ratio of the average bare rail intensity (Figure 8-8) to the average velocity (Figure 8-6) to be $R_I=0.057$ w/ft. The reflective tape has a very large LIR value (>50).

To prepare the rail for Test 2, Section A is lubricated by a commercially-available, water-based ToR friction modifier, as shown in Figure 8-10. The rail is scanned with the LIDAR sensor and the Doppler shift spectra are collected. FWHM measurements for this test are shown in Figure 8-11. Similar to Test 1, a moving average is applied to the raw measurements. The average FWHM drops when the trolley travels from the lubricated segment (Section A) to the dry segment (Section B). The FWHM values are then normalized by the LIDAR track speed data (Figure 8-12) to calculate the RSF ratios. As plotted in Figure 8-13, the lubricated segment yields a lower average RSF value, as compared with the dry section. A significant 53% variation in average RSF ratio is observed for the coated segment, with respect to the dry RSF value. Using the dry rail intensity measure ($R_I=0.057$ w/ft), LIR values are computed for both lubricated and dry sections. As shown in Figure 8-14, the average LIR for Section A with friction modifier is 9.2 times greater than the average LIR for bare Section B.



Figure 8-10. A water-based ToR friction modifier is applied on Section A for Test 2.

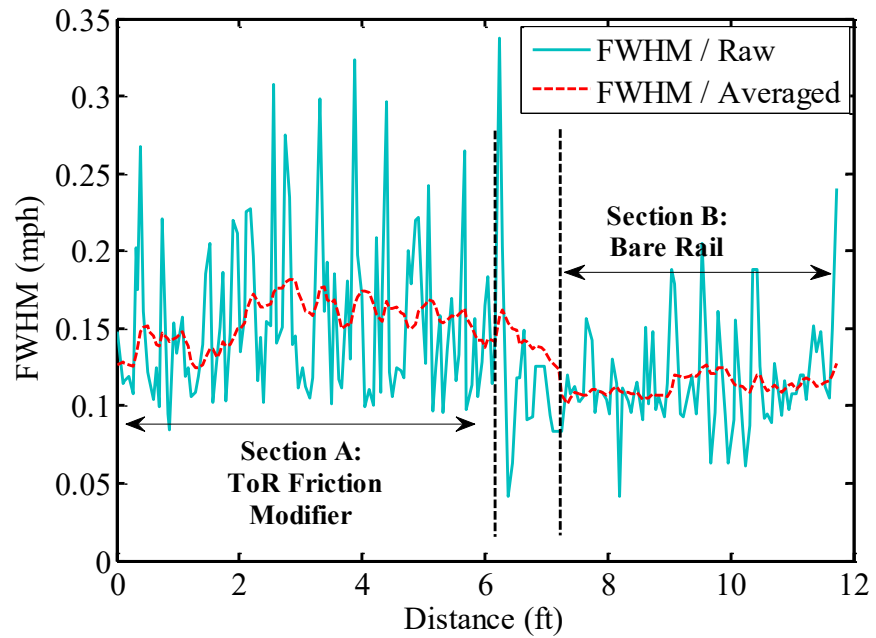


Figure 8-11. LIDAR FWHM measurements collected over the lubricated Section A and bare Section B in Test 2. A moving average with a window size of 15 data points is applied to the raw FWHM data.

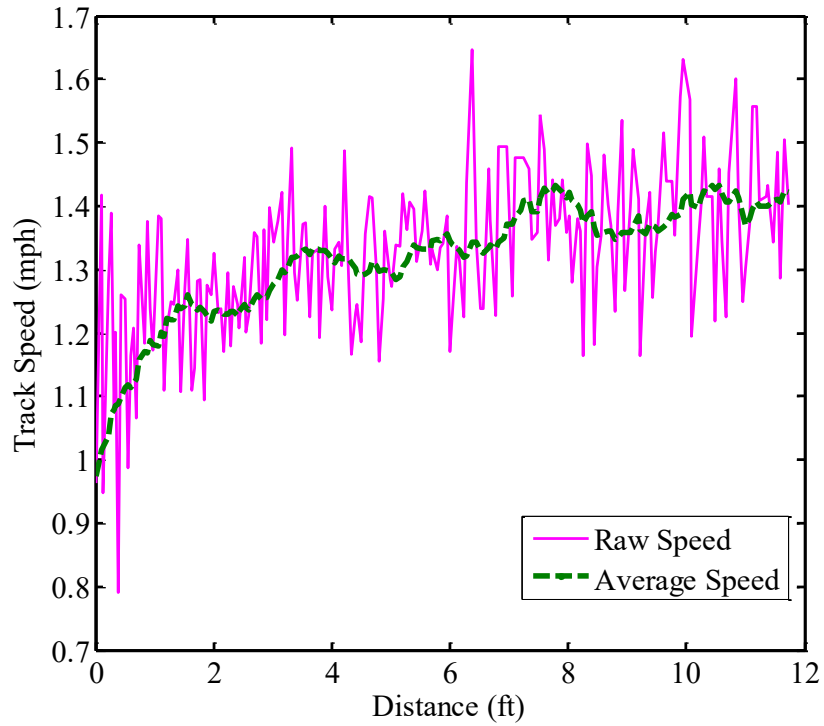


Figure 8-12 LIDAR track speed measurements during Test 2. A moving average is applied to the raw speed data to remove the high frequency variations.

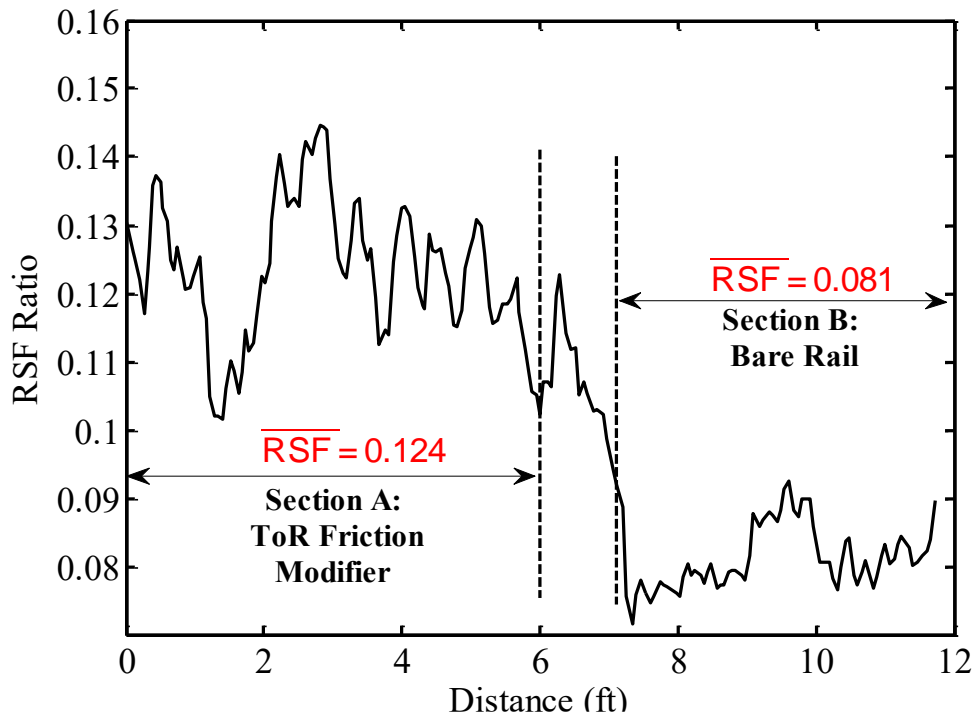


Figure 8-13. RSF measurements for the lubricated Section A and bare Section B in Test 2. There is a 53% variation between the average RSF ratios for these two coating conditions.

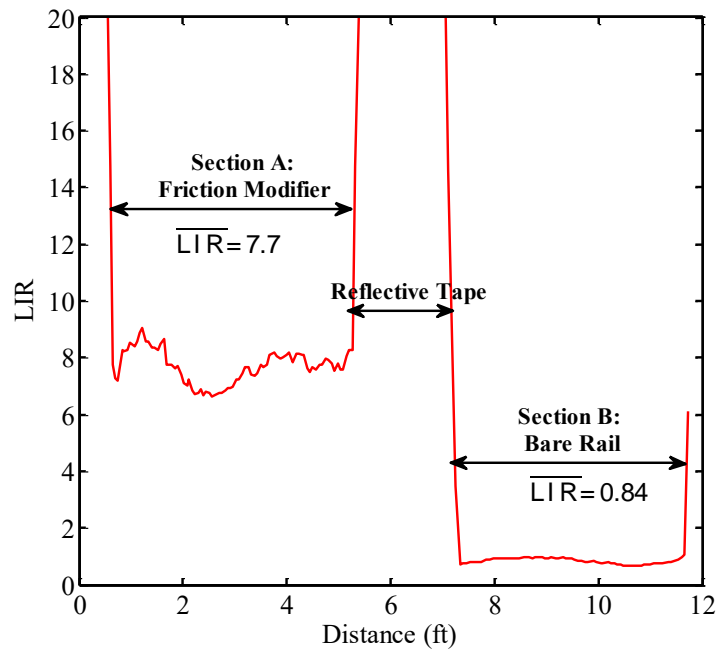


Figure 8-14. LIR results for Test 2 ($R_f=0.057$ w/ft). The average LIR for Section A with friction modifier is 9.2 times greater than the average LIR for bare Section B.

Because leaf residues affect the rail coefficient of friction, it is advantageous for the railroads to provide a reliable technique to automatically detect the rails covered by leaves. In order to simulate a rail with leaf residues, sawdust is manually dispensed on Section A as illustrated in Figure 8-15. Figure 8-16 and Figure 8-17, respectively, show the RSF ratios and LIR measurements extracted from the LIDAR data. A 45% increase in the average RSF ratio is observed over Section A (coated with sawdust), with respect to the bare Section B. Additionally, the average LIR of Section A is 9 times greater than the average LIR of the bare Section B.



Figure 8-15. Sawdust is applied on Section A to simulate leaf residues on the rail for Test 3.

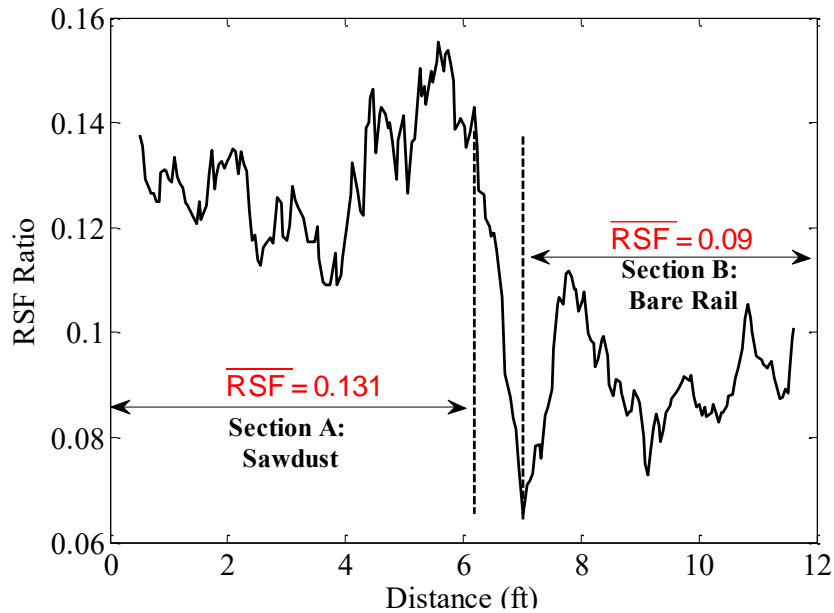


Figure 8-16. RSF measurements for Section A with sawdust coating and bare Section B in Test 3. There is a 45% variation between the average RSF ratios for these two coating conditions.

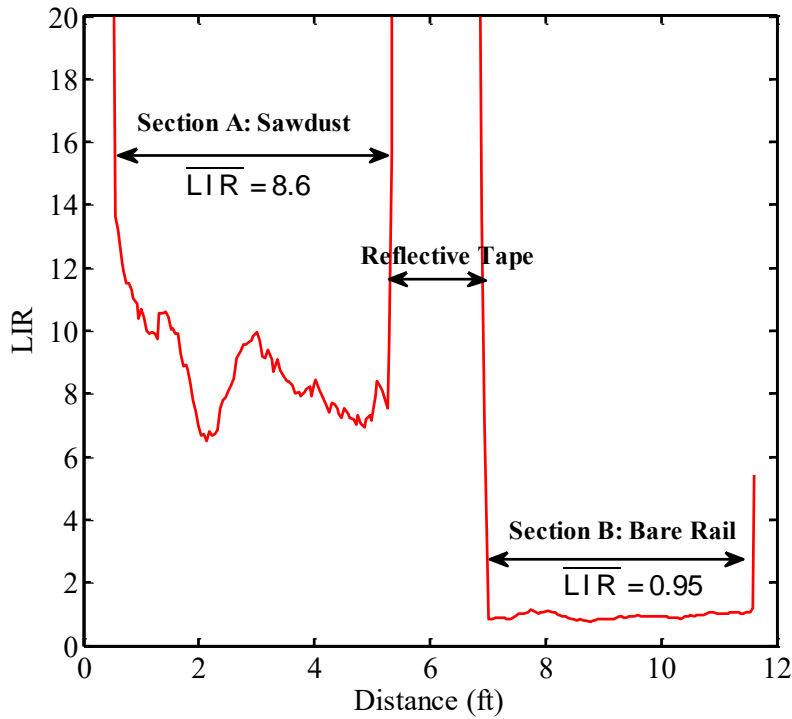


Figure 8-17. LIR results for Test 3 ($R_I=0.057$ w/ft). The average LIR for Section A with sawdust is 9 times greater than the average LIR for bare Section B.

The ideal testing environment for rail roughness monitoring is a rail panel with various ToR surface finish properties, but similar ToR surface material. To avoid damaging the RTL rail panel, however, the demonstration experiments are conducted by covering the rail with sandpaper.

Figure 8-18 shows the rail when it is covered by 40-grit coarse sandpaper. The RSF results shown in Figure 8-19 indicate that there is a significant 80% difference between the average in RSF ratios of the coated surface and bare rail. Moreover, as shown in Figure 8-20, the LIR of the coated surface is approximately 5.4 times greater than the average LIR of the bare rail.



Figure 8-18. Top of the rail in Section A is covered by 40-grit sandpaper to simulate a coarse rail surface (Test 4).

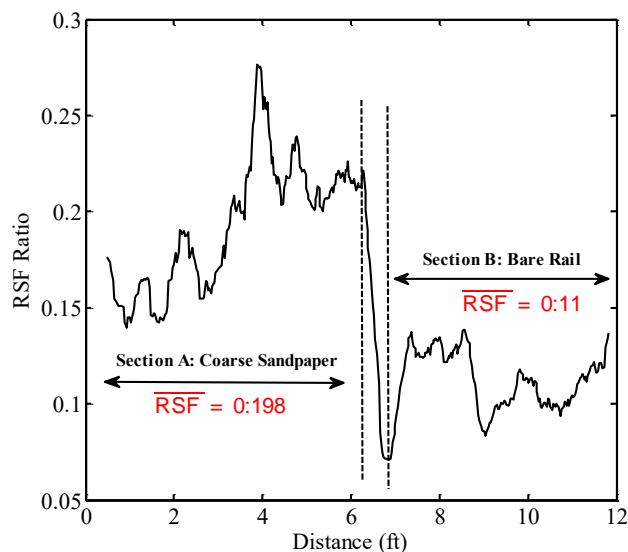


Figure 8-19. RSF measurements for Section A with sandpaper coating and bare Section B in Test 4. There is an 80% variation between the average RSF ratios for these two coating conditions.

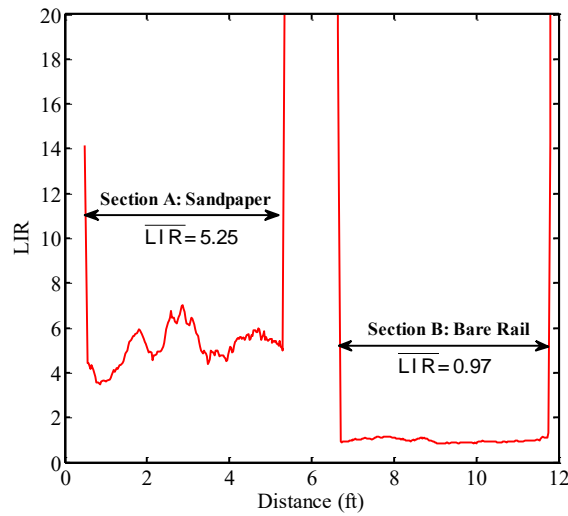


Figure 8-20. LIR results for Test 4 ($R_I=0.057$ w/ft). The average LIR for Section A with sandpaper is 5.4 times greater than the average LIR for bare Section B.

Test 5 is a repetition of Test 4, and it is intended to evaluate the repeatability and precision of the rail surface assessment technique. Figure 8-21 and Figure 8-22 show the RSF and LIR measurements for this coating condition. Comparing these graphs with the results of Test 4 indicates an 8% variation in RSF measurements, and a 2% deviation in LIR values. It is worth noting that the variations observed in RSF and LIR measures are caused by both the roughness and reflectivity of the sandpaper, not purely the roughness variation with the bare rail.

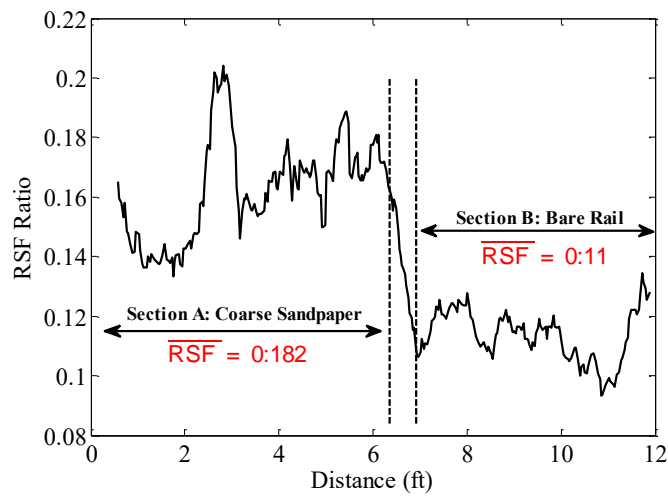


Figure 8-21. RSF measurements for Section A with sandpaper coating and bare Section B in Test 5.

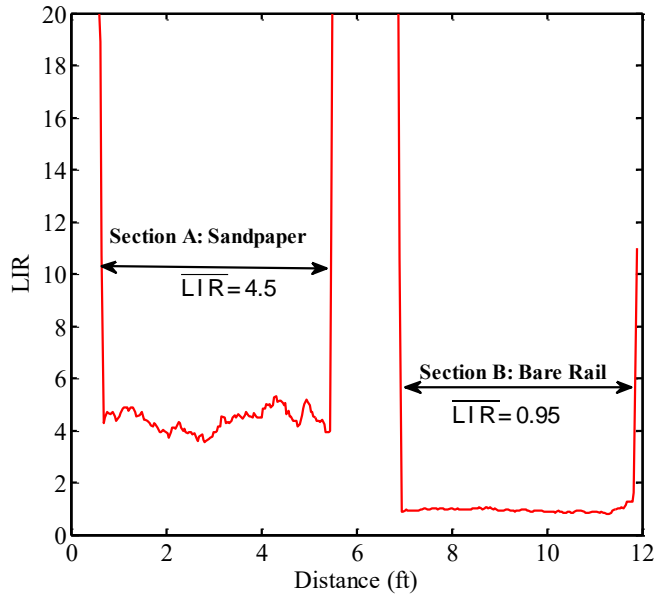


Figure 8-22. LIR results for Test 5 ($R_t=0.057$ w/ft). The average LIR for Section A with sandpaper is 4.7 times greater than the average LIR for bare Section B.

RSF ratio and LIR measurements made for different rail surface conditions over Section A are compared in Figure 8-23 and Figure 8-24, respectively. Although local spontaneous variations are observed, different rail surface conditions yield various RSF and LIR measures.

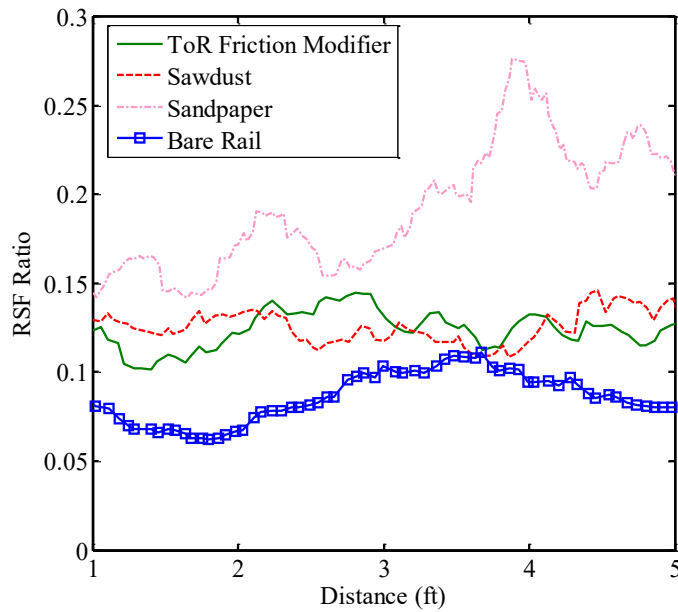


Figure 8-23. Comparison of RSF ratio measurements made for different rail surface conditions over Section A.

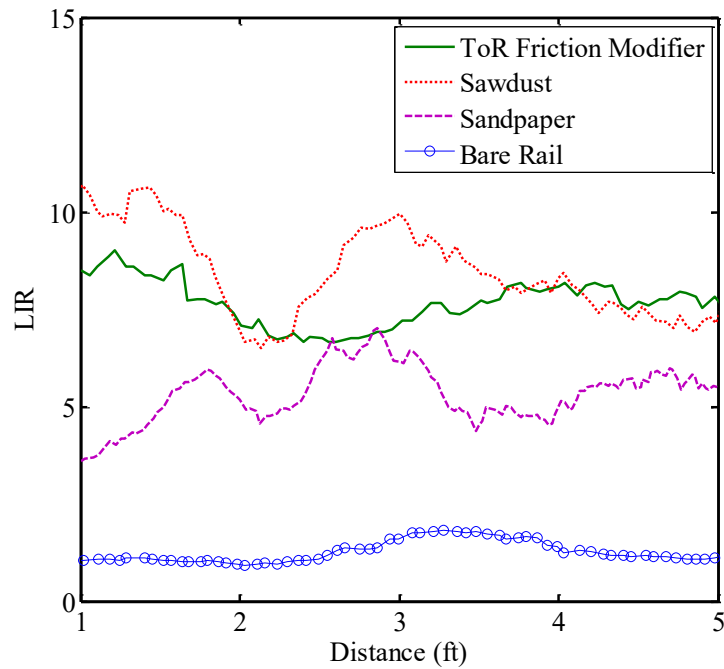


Figure 8-24. Comparison of LIR measurements made for different rail surface conditions over Section A.

Surface ratio computations of the tested rail surface conditions are summarized in Table 8-2. In addition to the average LIR and RSF ratios for each surface, the relative percentage differences of the coated (wet) surface ratios to the dry surface ratios, represented by d_{RSF} and d_{LIR} for the RSF and LIR, are calculated and listed in the table.

Table 8-2. A summary of the surface ratio calculations for Section A with various rail surface conditions.

Test #	Surface	RSF	d_{RSF} (%)	LIR	d_{LIR} (%)
1	Bare rail	0.08	0	1.25	0
2	ToR friction modifier	0.124	55	6.5	420
3	Sawdust	0.131	64	8.5	580
4	Coarse sandpaper	0.198	147	4.7	276
5	Coarse sandpaper	0.182	127	4.8	284

The primary limitation of the LIDAR-based surface monitoring technique is the measurement ambiguity when unknown materials are targeted. In other words, two different surfaces could yield very similar LIR and/or RSF ratios, depending on their compositions and scattering properties. The technique, however, is reliably applicable to known surface and material environments such as rails, where only specific surface conditions are expected to appear. In order to be able to make reliable measurements of the rail surface condition, the inspection system must be calibrated. Extensive calibration test-runs are required to generate adequate numerical reference patterns for the surface ratios, either in the form of simple lookup tables or more sophisticated empirical models. The calculated surface ratios during track monitoring will then be correlated with the patterns to recognize the surface material and/or roughness. It is important to mention that the proposed technique is not able to detect incipient cracks, but can detect full separations, including such as those at the loose rail joints and broken weldments.

Chapter 9 Development of a Bipolar LIDAR System for Track Curvature Measurements

The ability of a two-channel research LIDAR system to record rail speed, track centerline speed, and curvature was recently demonstrated by Virginia Tech's Railway Technology Laboratory (RTL) [67]. The LIDAR system was configured to measure track speed and curvature using a set of two lenses, while installed onboard a geometry car and operated by a class I railroad. The test results, as extensively discussed in previous chapters, indicated that the Doppler LIDAR system can be used as a multifunctional non-contact sensor for rail monitoring at speeds as low as 0.5 MPH and upwards into typical speeds of revenue service trains. Compared to the wheel-mounted encoder, the LIDAR system provides speed measurements with higher fidelity due to the absence of mechanical failures and periodic recalibration. Unlike the inertial measurement unit (IMU), the LIDAR system is not restricted to an acceleration and yaw rate sensitivity floor, and can detect train motion and track curvature at far lower speeds. Moreover, a foot-pulse generator was successfully added to the system in order to express data on a per-foot basis [66]. The ground-truth curvature measurements were also carried out by manual string-line tests for a set of selected curves. Curvature measured by the LIDAR system showed a close correlation with ground-truth measurements, in terms of any variations in alignment and track. Comparison with ground-truth curvature increases the fidelity of genuine curvature estimation, as opposed to comparison with IMU curvature data that presents its own inaccuracies in measurement.

The detection and computation techniques in previous works, however, required implementation of at least two body-mounted LIDAR sensors with fixed laser beams. A critical issue for railroad adoption of LIDAR speed sensing technologies is the question of the per-channel cost of the sensor. The proposed concept is intended to establish the means for measuring track centerline speed and instantaneous curvature through an effective, low-cost, single-channel, digitally-processed LIDAR system. A bipolar LIDAR system, as described in the following section, can be mechanically developed by shifting the laser beam

between the left and right rails using an optical mirror that is actuated in a saturated switching mode.

9.1 Single Channel Bipolar LIDAR System

The curvature detection technique developed and evaluated at RTL in the past few years is extended to further investigate the application of LIDAR speed sensing technologies for railroad applications of interest to the U.S. railroads. As described in the following, in a concept evaluation attempt, the feasibility and applicability of using a single-channel, bipolar Doppler LIDAR system for accurate rail speed measurement and instantaneous track curvature detection are studied.

9.1.1 Description of the concept

The proposed speed scanning configuration consists of a fiber optic LIDAR sensor to capture the Doppler shift, an optical mirror to guide the laser beam, and a saturated switch to actuate the mirror and determine the mode of speed detection. A graphical representation of the scanning setup is shown in Figure 9-1. The LIDAR system measures the left rail speed when the switch is in mode I, and it surveys the right rail when shifted to mode II. The speed measurements are then processed to extract centerline speed and instantaneous curvature.

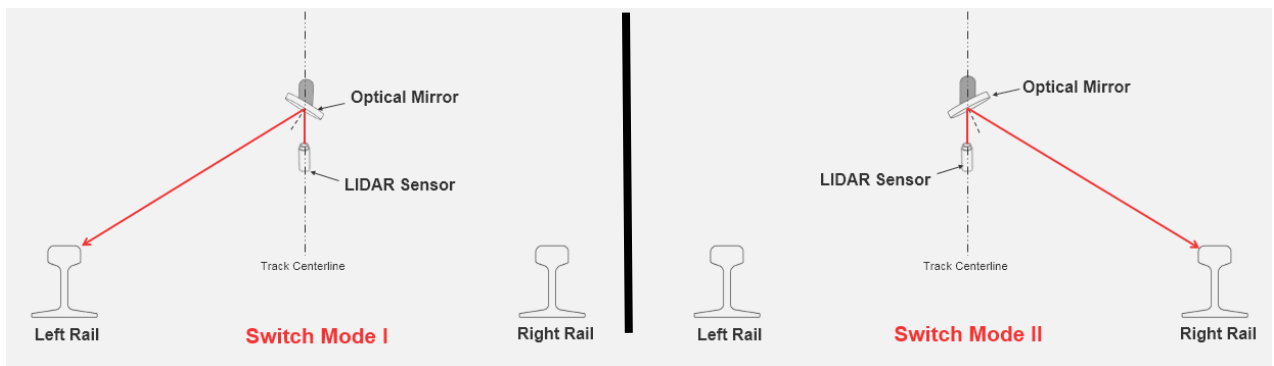


Figure 9-1. Proposed setup of a single-channel optic LIDAR system and bipolar switching mechanism: the LIDAR system measures the left rail speed when the switch is in mode I, and it surveys the right rail when shifted to mode II.

Different scanning configurations are possible for the bipolar LIDAR setup. In the 2-points embodiment, as depicted in Figure 9-2(a), the scanning actuator (motor) provides 120° steps. In this case, the LIDAR beam switches between points A and B, and thus each rail is surveyed once during a scanning cycle. If the scanning cycle starts from point A at data-point k , then the right and left track speeds will be $V_R(x) = V(k)$ and $V_L(x) = V(k+1)$, respectively. A scanning instrument with finer steps yields more accurate curvature measurements by surveying each rail at multiple points. As an example, Figure 9-2(b) shows an embodiment with 60° scanning steps. This 4-points system provides 2 scanning spots on each rail. Figure 9-2(b) shows a counterclockwise rotating survey that starts from point A on the right rail at data-point k . In this case, the measurements taken at A and B (data-points k and $k+1$) define the right track speed as $V_R(x) = 0.5[V(k) + V(k+1)]$, while the measurement spots D and E (data-points $k+4$ and $k+5$) represent the left track speed as $V_L(x) = 0.5[V(k+4) + V(k+5)]$. The data taken at spots C and F (data-points $k+2$ and $k+6$) are then redundant and should be ruled out from the computations.

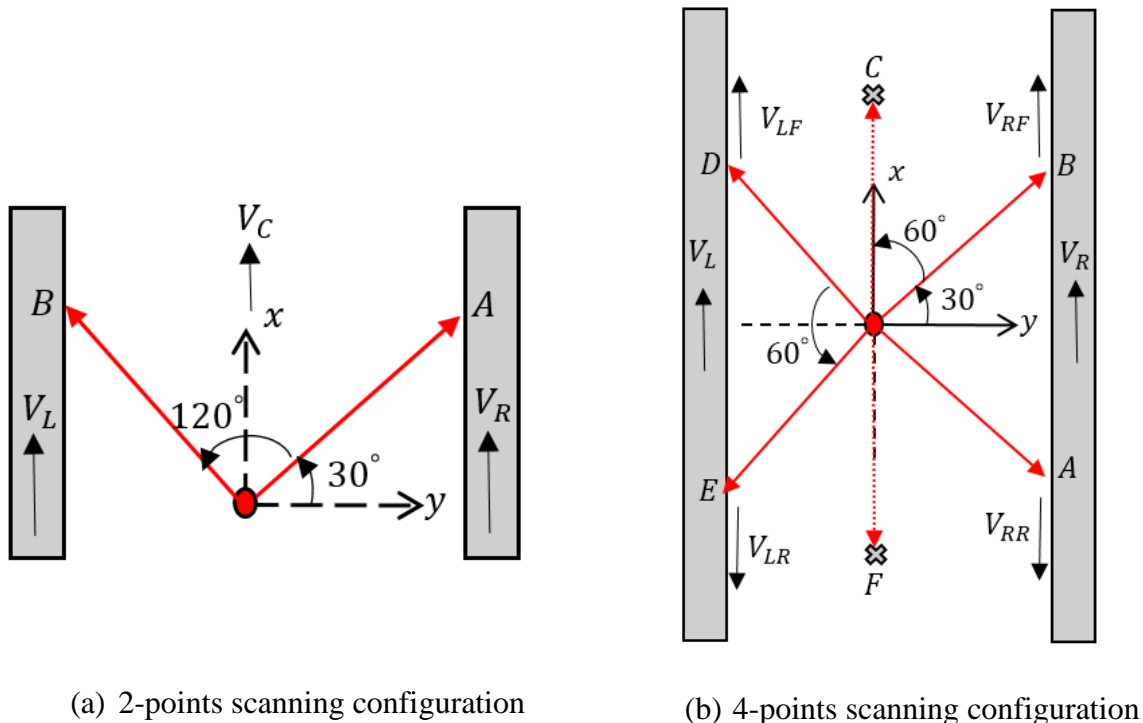


Figure 9-2. Different scanning configurations are possible for the bipolar LIDAR setup. In the 2-points embodiment, each rail is surveyed at one point, while the 4-points system provides 2 scanning points for each rail.

Left and right track speeds vary as the vehicle negotiates a curve. Track curvature is calculated based on the difference between the left and right track speeds. Figure 9-3 shows a track panel that consists of a left curve, a tangent segment, and a right curve, respectively, from the bottom to the top. Forward components are shown by V_{Rx} and V_{Lx} , and lateral components are labelled as V_{Ry} and V_{Ly} . The forward components are used to derive the centreline speed as well as track curvature, while the lateral components are used to extract the lateral track variations. Starting from the bottom, the vehicle enters the left curve with the $+x$ forward direction. For the vehicle to negotiate the left curve, the right rail forward speed must be greater than the left rail forward speed $V_{Rx} > V_{Lx}$. The two forward speeds become identical as the vehicle passes over the tangent segment ($V_{Rx} = V_{Lx}$). As the vehicle starts to negotiate the right curve, the left rail forward speed exceeds the right rail forward speed ($V_{Lx} > V_{Rx}$). Therefore, the left and right forward track speed difference represents the track instantaneous curvature. The sign of the forward speed variance determines the direction of the curvature (left or right), while the magnitude represents the degree of curvature.

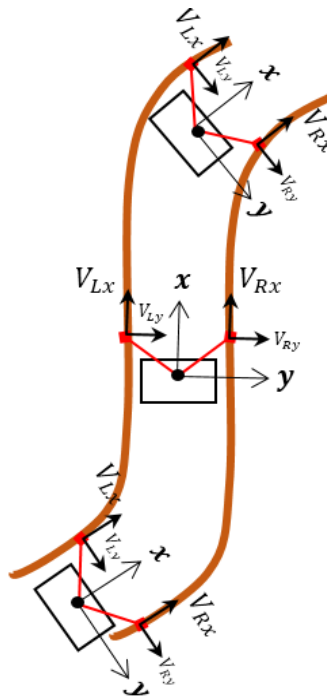


Figure 9-3. Illustration of left and right track speed variation over a track panel that consists of a left curve, a tangent segment, and a right curve.

Figure 9-4 shows the instantaneous left and right forward track travels (d_L and d_R) over a right curve. For a given nominal gage (G), degree of curvature (θ) is represented by the ratio of the instantaneous left and right forward travel difference during a specific time period (dt) to the nominal gage as:

$$\theta \approx \frac{d_L - d_R}{G} = \frac{(V_L - V_R)dt}{G} \quad (9-1)$$

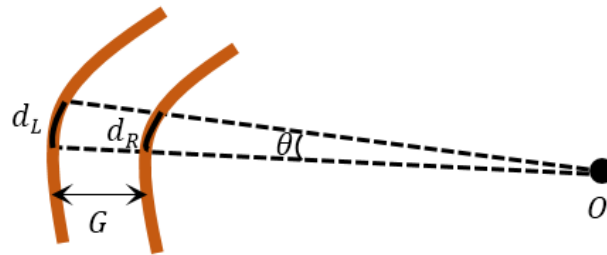


Figure 9-4. Track degree of curvature is calculated based on the left and right track forward speed difference.

9.1.2 Prototype development and testing

Lab tests are conducted to qualitatively demonstrate the bipolar track speed sensing concept. For this demonstration effort, only the parts in hand are utilized, which do not include a robust saturated switch with position feedback. The test setup configured for this purpose is shown in Figure 9-5. An optical mirror is mounted to a servo motor with an adjustable inclination angle. Employing a saturated switch (unlike a rotating mechanism) does not interfere with the Doppler shift raised by the rail speed. The optical mirror is oriented at a specific inclination angle to guide the laser beam toward the rails with a designated strike angle. The fiber optic sensor is installed co-axially underneath the mirror, and the mirror is oriented so that the LIDAR beam targets the gage corner of the rails.

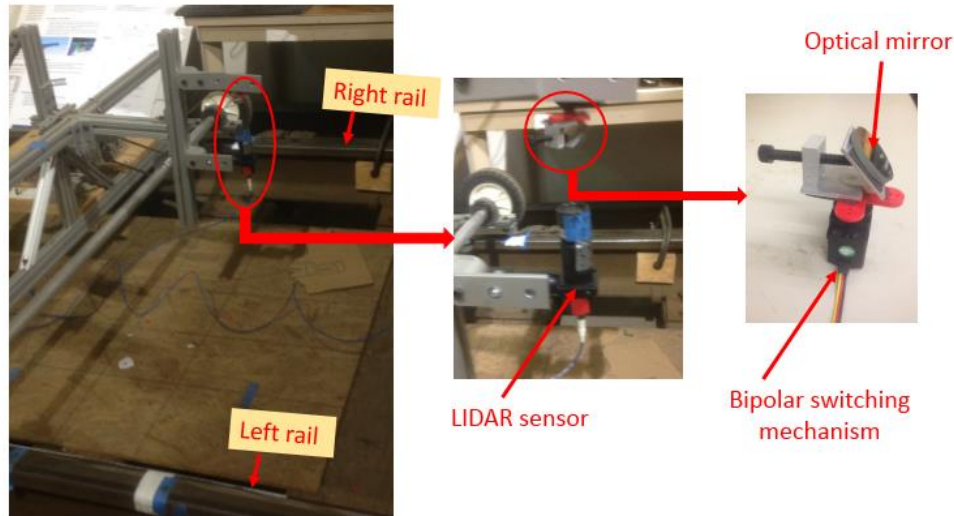


Figure 9-5. The testing setup configured to collect preliminary data for proof of concept of the bipolar LIDAR scanning system.

Using the test setup shown in Figure 9-5 and connecting the single-channel laser sensor to the PXI system (which collects and processes the Doppler shift data in real-time) preliminary tests are performed on RTL track panel. The servo is programmed to provide a 2-points bipolar switching pattern as depicted in Figure 9-2(a) with a scanning period of $T=4$ s. Figure 9-6 shows the speed measurement results for two consecutive switching cycles. As the plots show, the LIDAR laser beam is maintained on each rail for 40% of the survey period ($0.4 T=1.59$ s) in order to provide adequate velocity data bins. The scanning frequency can be adjusted based on the system requirements, LIDAR data rate, and train forward speed.

The LIDAR speed measurement results for one of the test runs are shown in Figure 9-7. In addition to raw speed data, the extracted left and right speed data after filtering and interpolation processes are also plotted in this figure. Results verify the functionality of the proposed bipolar speed sensing technique. Note that the difference between the two speed plots (left and right rails) is due to unequal strike angles and asymmetric setup. The final prototype requires the development of robust and accurate fixtures that secure identical angles of attack for the two detection modes. A closer view of the raw data for one switching cycle is shown in Figure 9-8. As this figure suggests, the velocity on each rail is assumed unchanged once the LIDAR laser is directed to the other rail.

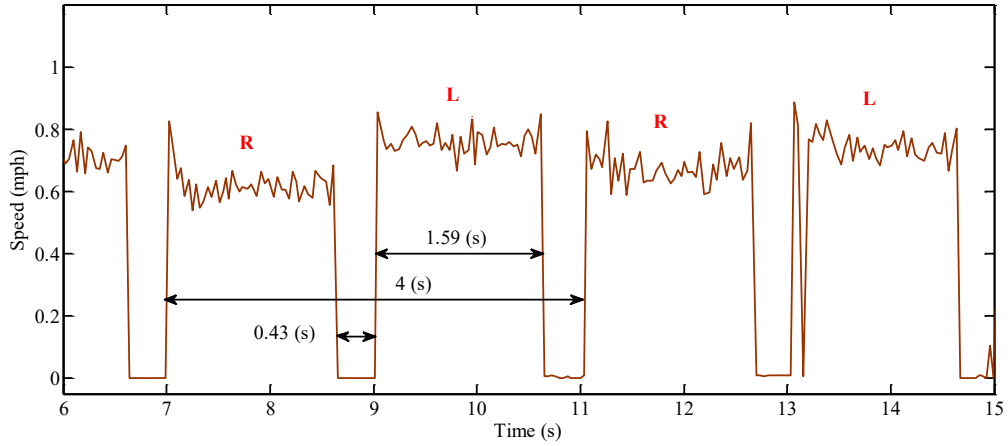


Figure 9-6. Speed measurement results for two switching cycles; R represents the scanning duration of the right rail, and L shows the surveying duration of the left rail. The scanning frequency is 0.25 Hz, and 40% of the survey is allocated to each rail.

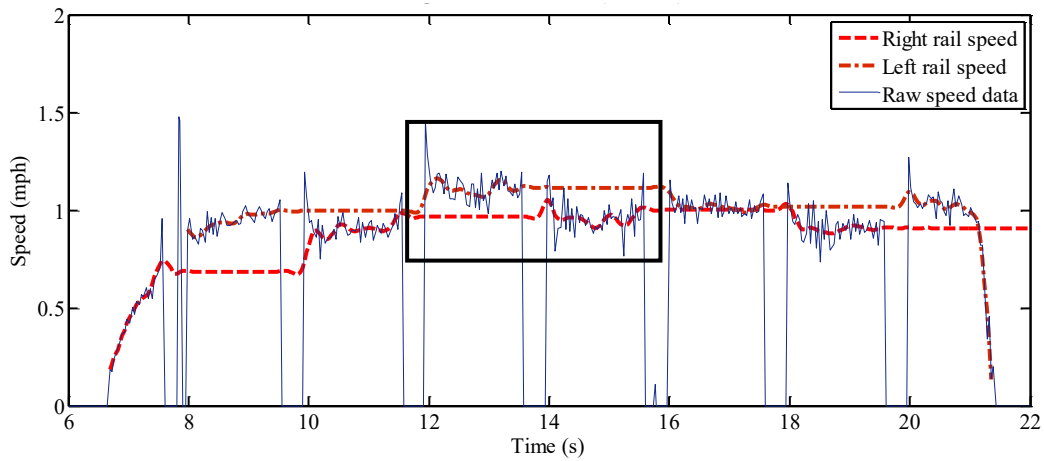


Figure 9-7. The bipolar LIDAR system speed measurements are used to calculate the left and right track speeds. The velocity on each rail is assumed unchanged once the LIDAR laser is directed to the other rail.

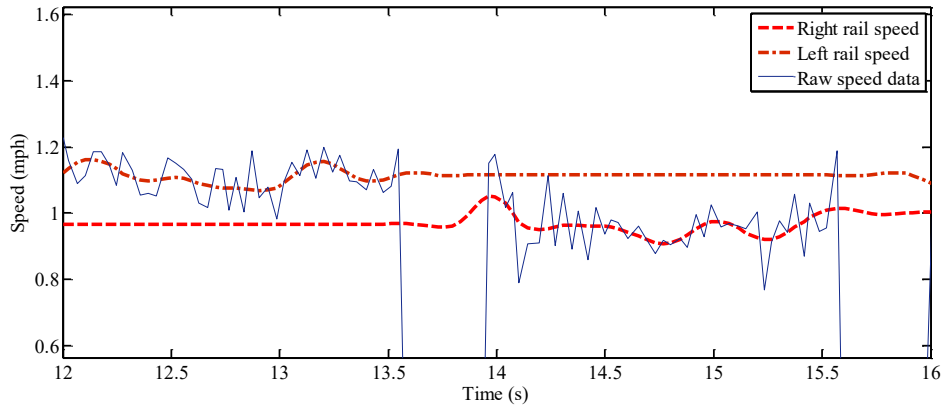


Figure 9-8. A close-up view of the speed measurements for one scanning cycle. A 3rd order low-pass filter is applied to the raw speed. The left and right track speed variation determines the track curvature.

The prototype shown in Figure 9-5 is developed for the concept demonstration purpose only. Additional efforts are required to develop a more robust setup for further testing and evaluation. A robust switching mechanism with suitable switching frequency should be implemented in order to collect adequate data bins from each rail required for an effective curvature measurement. Additionally, the hardware required for system installation onboard a track geometry car should be developed. This hardware must protect the laser and mirror setup while maintaining the geometry adjustments, specifically the laser beam angle of attack and mirror axis-alignment.

For the geometry calculations to be accurate, the LIDAR speed measurements should be synchronized with the scanning mode. An appropriate position detection technique must be developed to detect the laser beam location (left/right rail or none) and integrate it with the LIDAR measurements. Signal processing algorithms, including filtering, averaging, and interpolation processes, should be established to derive the measurements of interest from the raw data.

The prototype system was tested on the short, tangent RTL track panel. It is, however, suggested that the system be field-tested over multiple tangent and curved tracks in order to identify the strengths and limitations of the proposed detection technique. Various parameters and scanning conditions should be studied, including the track speed, strike angle, and switching frequency.

Chapter 10 Summary and Recommendations

10.1 Summary

The applicability of non-contact, optical fiber Light Detection And Ranging (LIDAR) technology for measuring track speed, curvature, and track geometry irregularities (lateral and vertical rail geometry variations) with high accuracy has been evaluated, using extensive tests onboard a track geometry car. The LIDAR system was configured to measure track speed and profile using a set of two lenses, while evaluating lateral track geometry variations (alignment and gage) using two additional low-elevation lenses that are properly oriented for such measurements. The measured geometry data was compared with the data from onboard conventional instruments in order to assess and contrast the LIDAR system's accuracy. The results of the successful tests indicate that the Doppler LIDAR velocimetry system implementations can be used as a multifunctional non-contact sensor for rail monitoring at speeds as low as 0.5 MPH and beyond typical speeds of revenue service trains. The field-testing conducted during this study indicates that LIDAR sensors could provide a reliable, non-contact track-monitoring instrument for field use, in various weather and track conditions, potentially in a semi-autonomous or autonomous manner.

A spatial track quality index was introduced to quantify the railroad track geometry conditions using LIDAR speed measurements. Due to the high accuracy of LIDAR speed data, the established indexing approach was shown to provide a reliable localized measure for geometry quality assessment. A phenomenological deterioration modelling platform was also established to estimate the track degradation based on the LIDAR TQI records and predict the overall geometry quality of a rail segment over time. Precise deterioration prediction is critical for an effective track maintenance planning. The experimental results and numerical assessments indicate that a body-mounted LIDAR system can provide precise, non-contact track monitoring equipment that could be used for both real-time track geometry detection as well as for overall track quality assessment purposes. LIDAR velocity systems

can be effectively implemented in research cars for various track geometry measurements as well as track deterioration assessment.

The application of LIDAR technology for rail surface monitoring was investigated in this study. Two rail surface measures were introduced based on the Doppler shift spectrum characteristics of the laser radiation reflected from the rails. These two indices provide relative indications of the rail surface condition. Lab tests indicated that the relative spectral intensity and Doppler bandwidth of the collected LIDAR beam can be used to detect different rail surface materials and conditions, including roughness, rail lubrication, ToR friction modifiers, and leaf residues. The LIDAR rail surface measurements may be further used to derive surface parameters such as friction, rail/wheel lubricity, and rail infrastructure integrity.

The ability of a single-channel, bipolar system to measure track speed and curvature was studied. The proposed concept is intended to establish the means for measuring track centerline speed and instantaneous curvature through an effective, low-cost, single-channel, digitally-processed LIDAR system. A bipolar LIDAR system can be mechanically developed by shifting the laser beam between the left and right rails using an optical mirror that is actuated in a saturated switching mode. A prototype system was configured for laboratory-scaled demonstration testing. The test results indicated that with proper processing, the speed data collected by a single-channel LIDAR system can be used to calculate centerline track speed and curvature.

10.2 Recommendations for Future Studies

The study indicates that the LIDAR system can 1) measure track geometry variations, and 2) provide a relative indication of track quality (TQI measurements). These functions need to be further verified against a calibrated track, such as the recently developed test facility at the Transportation Technology Center, Inc., in order to determine the exact accuracy of the measurements.

Ground-truth distance measurements were performed during the study. It was not possible, however, to perform similar field measurements for track geometry. The recent construction of a finely-calibrated track by FRA at the Transportation Technology Center, Inc., in Pueblo, CO, provides an excellent test facility to verify the LIDAR measurements against the geometries designed into the track, using one of the FRA geometry cars. This will not only verify the accuracy and repeatability of the track geometry measurements by LIDAR, but also provide for the implementation of any additional signal processing improvements that may be needed.

In addition to collecting the repeatability data on a calibrated track, it is recommended that a series of repeatability studies be conducted in a controlled laboratory environment, such as the RTL rail panel and/or the shock dyno. It is suggested that the rail cart be run over the same stretch of the rail panel multiple times. The collected data should then be used to examine the repeatability of the track geometry measurements made by the LIDAR system. For the results to be more useful, it is recommended to resolve the stability issues of the RTL rail cart or possibly design and fabricate a more robust cart. In addition to cart testing and in order to have a more controlled testing setup, it is recommended that further repeatability tests be performed on the dyno (similar to the testing configuration discussed in Chapter 6). Using the shock dyno, specific tests can be repeated precisely with minimal unwanted motion. Therefore, the results will provide a better assessment of the repeatability.

Another topic that deserves further research is the applicability of a LIDAR system for rail surface monitoring. Preliminary lab tests indicate that Doppler laser sensors can be used to monitor the rail surface material and condition. Extensive calibration test-runs are, however, required to generate adequate reference patterns for the proposed rail surface ratios. The applicability of the LIDAR measurements for detecting RCF damages should also be verified against a calibrated track. Moreover, it is recommended that a rail cover be fabricated with multiple sections that have different surface finish properties. The cover should then be mounted on the rail, and the ToR surface feature ratios should be measured and compared.

It is also recommended that the study be extended to evaluate the LIDAR system's sensitivity to car body motion. Although laboratory tests have already verified that onboard vibrations

do not have a significant effect on the intended uses of the LIDAR system, having access to a field facility that better represents the end-user environment will significantly advance the technology readiness.

Lastly, it is recommended that the single-channel LIDAR setup discussed in Chapter 9 for track speed and curvature measurement be further studied. Additional efforts are needed to develop a more robust system for field testing and performance evaluation. An effective switching mechanism with suitable switching frequency should be implemented in order to collect adequate data bins from each rail depending on the desired precision of the track curvature measurements. Additionally, the hardware required for system installation onboard a track geometry car should be developed. The mounting fixtures must protect the laser and mirror setup while maintaining the geometry adjustments, specifically, the laser beam angle of attack and mirror axis-alignment.

References

- [1] S. Bruni, R. Goodall, T. X. Mei, and H. Tsunashima, "Control and monitoring for railway vehicle dynamics," *Vehicle System Dynamics*, vol. 45, pp. 743–779, 2007.
- [2] J. Madejski, "Autonomous track geometry diagnostics system," *J. Mater. Process. Technol.*, vol. 157, pp. 194–202, 2004.
- [3] G. W. J. Heynen, "Railway induced vibrations," 1987.
- [4] R. A. Smith, "Railway fatigue failures: an overview of a long standing problem," *Materwiss. Werksttech.*, vol. 36, no. 11, pp. 697–705, 2005.
- [5] M. Dembosky, "Rolling contact fatigue (RCF) in the UK system- the emerging solution.," in *Permanent Way Institution Journal and Report of Proceedings*, 2004, vol. 122, no. 3, pp. 121–129.
- [6] E. E. Magel, "Rolling contact fatigue: a comprehensive review," 2011.
- [7] M. El-Sibaie, D. Jamieson, B. Mee, B. Whitten, K. Kesler, D. Tyrell, and J. Dorsey, "Engineering studies in support of the development of high-speed track geometry specifications," in *IEEE/ASME Joint Railroad Conference. Boston, Massachusetts*, 1997.
- [8] S. Saadat, C. Stuart, G. Carr, and J. Payne, "Development and Use of FRA Autonomous Track Geometry Measurement System Technology," in *AREMA*, 2014.
- [9] C. Esveld, "Modern railway track," 2001.
- [10] J. Kawasaki and K. Youcef-Toumi, "Estimation of rail irregularities," in *American Control Conference, 2002*, 2002, vol. 5, pp. 3650–3660.
- [11] P. Westeon and C. Ling, "Monitoring vertical track irregularity from in-service railway vehicles," *Proc. Inst. Mech. Eng. Part F J. Rail Rapid Transit*, vol. 221, no. 1, pp. 75–88, 2007.
- [12] S. Alfi and S. Bruni, "Estimation of long wavelength track irregularities from on board measurement," in *Railway Condition Monitoring, 2008 4th IET*, 2008, pp. 1–6.
- [13] H. Tsunashima, "Track geometry estimation from car-body vibration," *Veh. Syst. Dyn.*, pp. 1–13, 2014.
- [14] H. Tsunashima, T. Kojima, A. Matsumoto, and T. Mizuma, "Condition monitoring of railway track using in-service vehicle," *Japanese Railw. Eng.*, vol. 161, pp. 333–356, 2008.
- [15] J. A. Zakeri, H. Xia, and J. J. Fan, "Dynamic responses of train-track system to single

- rail irregularity,” *Lat. Am. J. Solids Struct.*, vol. 6, no. 2, pp. 89–104, 2009.
- [16] E. G. Berggren, M. X. D. Li, and J. Spännar, “A new approach to the analysis and presentation of vertical track geometry quality and rail roughness,” *Wear*, vol. 265, no. 9, pp. 1488–1496, 2008.
- [17] A. B. Stanbridge and D. J. Ewins, “Measurement of translational and angular vibration using a scanning laser Doppler vibrometer,” *Shock Vib.*, vol. 3, no. 2, pp. 141–152, 1996.
- [18] D. Kim, H. Song, H. Khalil, J. Lee, S. Wang, and K. Park, “3-D Vibration Measurement Using a Single Laser Scanning Vibrometer by Moving to Three Different Locations.”
- [19] A. E. Fazio and J. L. Corbin, “Track quality index for high speed track,” *J. Transp. Eng.*, vol. 112, no. 1, pp. 46–61, 1986.
- [20] W. Ebersohn, “Implementing a railway infrastructure maintenance system,” in *Conference on Railway Engineering Proceedings: Engineering Innovation for a Competitive Edge*, 1998, p. 395.
- [21] J. Madejski and J. Grabczyk, “Continuous geometry measurement for diagnostics of tracks and switches,” in *International Conference on Switches: Switch to Delft*, 2002.
- [22] P. Xu, Q. Sun, R. Liu, and F. Wang, “A short-range prediction model for track quality index,” *Proc. Inst. Mech. Eng. Part F J. Rail Rapid Transit*, vol. 225, no. 3, pp. 277–285, 2011.
- [23] M. El-Sibaie and Y.-J. Zhang, “Objective track quality indices,” *Transp. Res. Rec. J. Transp. Res. Board*, vol. 1863, no. 1, pp. 81–87, 2004.
- [24] A. Andrade, “Renewal decisions from a Life-cycle Cost (LCC) Perspective in Railway Infrastructure: An integrative approach using separate LCC models for rail and ballast components.” M. Sc Thesis (Supervisor: Paulo Fonseca Teixeira), Technical University of Lisbon (IST), Lisbon, Portugal, 2008.
- [25] J. P. Hyslip, “Fractal analysis of track geometry data,” *Transp. Res. Rec. J. Transp. Res. Board*, vol. 1785, no. 1, pp. 50–57, 2002.
- [26] R. Clark, “Rail flaw detection: overview and needs for future developments,” *NDT E Int.*, vol. 37, no. 2, pp. 111–118, 2004.
- [27] Z. Li, X. Zhao, C. Esveld, R. Dollevoet, and M. Molodova, “An investigation into the causes of squats—Correlation analysis and numerical modeling,” *Wear*, vol. 265, no. 9, pp. 1349–1355, 2008.
- [28] M. P. Papaalias, C. Roberts, and C. L. Davis, “A review on non-destructive evaluation of rails: state-of-the-art and future development,” *Proc. Inst. Mech. Eng. Part F J. Rail rapid transit*, vol. 222, no. 4, pp. 367–384, 2008.

- [29] R. Pohl, R. Krull, and R. Meierhofer, “A new eddy current instrument in a grinding train,” in *Proceedings of ECNDT*, 2006.
- [30] J. Stanford, E. Magel, and P. Sroba, “Transitioning from corrective to preventive grinding on the BNSF railroad,” in *Proceedings of the Seventh International Heavy Haul Railway Conference, Brisbane*, 2001, pp. 493–501.
- [31] P. Sroba, M. Roney, R. Dashko, and E. Magel, “Canadian Pacific Railway’s 100% effective lubrication initiative,” in *Proceedings of the Presentation for AREMA 2001 Conference & Exhibition, Chicago, Illinois*, 2001, pp. 9–12.
- [32] U. Olofsson and R. Nilsson, “Surface cracks and wear of rail: A full-scale test on a commuter train track,” *Proc. Inst. Mech. Eng. Part F J. Rail Rapid Transit*, vol. 216, no. 4, pp. 249–264, 2002.
- [33] D. I. Fletcher and J. H. Beynon, “The effect of intermittent lubrication on the fatigue life of pearlitic rail steel in rolling-sliding contact,” *Proc. Inst. Mech. Eng. Part F J. Rail Rapid Transit*, vol. 214, no. 3, pp. 145–158, 2000.
- [34] E. Magel, P. Sroba, K. Sawley, and J. Kalousek, “Control of rolling contact fatigue of rails,” *Cent. Surf. Transp. Technol. Natl. Res. Counc. Canada*, 2005.
- [35] R. Stock, D. T. Eadie, D. Elvidge, and K. Oldknow, “Influencing rolling contact fatigue through top of rail friction modifier application—A full scale wheel–rail test rig study,” *Wear*, vol. 271, no. 1, pp. 134–142, 2011.
- [36] D. T. Eadie, M. Santoro, and W. Powell, “Local control of noise and vibration with KELTRACK™ friction modifier and Protector® trackside application: an integrated solution,” *J. Sound Vib.*, vol. 267, no. 3, pp. 761–772, 2003.
- [37] D. T. Eadie, J. Kalousek, and K. C. Chiddick, “The role of high positive friction (HPF) modifier in the control of short pitch corrugations and related phenomena,” *Wear*, vol. 253, no. 1, pp. 185–192, 2002.
- [38] D. T. Eadie, B. Vidler, N. E. Hooper, and T. W. Makowsky, “Top of rail friction control: lateral force and rail wear reduction in a freight application,” in *Proceeding of International Heavy Haul Association (IHHA) Conference*, 2003, pp. 5–9.
- [39] S. Kumar, G. Chattopadhyay, V. Reddy, and U. Kumar, “Issues and challenges with logistics of rail maintenance,” in *Proceedings of the Second International Logistics Sections Conference*, 2006, pp. 22–23.
- [40] A. M. Hasan, “Quantitative Laser-based Assessment of Top of Rail Friction Modifiers for Railroad Application,” Virginia Tech, 2016.
- [41] A. M. Hasan, M. T. Andani, and M. Ahmadian, “On the Application of Laser Technology for the Rail Lubricity Detection,” in *2016 Joint Rail Conference*, 2016.
- [42] M. Malvezzi, B. Allotta, and M. Rinchi, “Odometric estimation for automatic train protection and control systems,” *Veh. Syst. Dyn.*, vol. 49, no. 5, pp. 723–739, 2011.

- [43] A. Mirabadi, N. Mort, and F. Schmid, "Application of sensor fusion to railway systems," in *Multisensor Fusion and Integration for Intelligent Systems, 1996. IEEE/SICE/RSJ International Conference on*, 1996, pp. 185–192.
- [44] S. S. Saab, G. E. Nasr, and E. A. Badr, "Compensation of axle-generator errors due to wheel slip and slide," *Veh. Technol. IEEE Trans.*, vol. 51, no. 3, pp. 577–587, 2002.
- [45] M. Ikeda, "Characteristic of position detection and method of position correction by rotating axle," *Railw. Tech. Res. Institute, Q. Reports*, vol. 34, no. 4, 1993.
- [46] B. Allotta, V. Colla, and M. Malvezzi, "Train position and speed estimation using wheel velocity measurements," *Proc. Inst. Mech. Eng. Part F J. Rail Rapid Transit*, vol. 216, no. 3, pp. 207–225, 2002.
- [47] W. C. Vantuono, "Do you know where your train is?," *Railw. Age*, 1996.
- [48] S. Iwnicki, *Handbook of railway vehicle dynamics*. CRC press, 2006.
- [49] T. Ando, S. Kameyama, and Y. Hirano, "All-fiber coherent Doppler lidar technologies at Mitsubishi Electric Corporation," in *IOP Conference Series: Earth and Environmental Science*, 2008, vol. 1, no. 1, p. 12011.
- [50] C. Holton and M. Ahmadian, "Doppler sensor for the derivation of torsional slip, friction and related parameters." Google Patents, 27-Apr-2010.
- [51] J. Rosen and L. Q. Gothard, *Encyclopedia of physical science*. Infobase Publishing, 2010.
- [52] L. N. Ridenour, *Radar system engineering*, vol. 1. Dover Publications, 1965.
- [53] J. Zhou and X. Long, "Laser Doppler velocimeter using a single longitudinal mode solid-state laser source," *Opt. Laser Technol.*, vol. 42, no. 7, pp. 1167–1171, 2010.
- [54] L. Solomon, "Lidar: The Speed Enforcement Weapon of Choice," *Law Enforc. Technol.*, vol. 33, no. 10, pp. 70–72, 2006.
- [55] H. Inokuchi, H. Tanaka, and T. Ando, "Development of an onboard doppler lidar for flight safety," *J. Aircr.*, vol. 46, no. 4, pp. 1411–1415, 2009.
- [56] C. M. Shun and P. W. Chan, "Applications of an infrared Doppler lidar in detection of wind shear," *J. Atmos. Ocean. Technol.*, vol. 25, no. 5, pp. 637–655, 2008.
- [57] G. J. Koch, J. Y. Beyon, E. A. Modlin, P. J. Petzar, S. Woll, M. Petros, J. Yu, and M. J. Kavaya, "Side-scan Doppler lidar for offshore wind energy applications," *J. Appl. Remote Sens.*, vol. 6, no. 1, pp. 63561–63562, 2012.
- [58] Y. L. Pichugina, R. M. Banta, W. A. Brewer, S. P. Sandberg, and R. M. Hardesty, "Doppler lidar-based wind-profile measurement system for offshore wind-energy and other marine boundary layer applications," *J. Appl. Meteorol. Climatol.*, vol. 51, no. 2, pp. 327–349, 2012.

- [59] D. Pierrottet, F. Amzajerjian, L. Petway, B. Barnes, and G. Lockard, “Flight test performance of a high precision navigation Doppler lidar,” in *SPIE Defense, Security, and Sensing*, 2009, p. 732311.
- [60] S. Wrobel, M. Ahmadian, M. Craft, and J. Munoz, “Multifunction LIDAR Sensors for Non-Contact Speed Measurement in Rail Vehicles: Part 2-Data Collection and Analysis,” in *2013 Joint Rail Conference*, 2013, pp. V001T02A008–V001T02A008.
- [61] J. Muñoz, M. Craft, M. Ahmadian, and S. Wrobel, “Multifunction LIDAR Sensors for Non-Contact Speed Measurement in Rail Vehicles: Part I-System Installation and Implementation,” in *2013 Joint Rail Conference*, 2013, pp. V001T02A009–V001T02A009.
- [62] G. Carr, A. Tajaddini, and B. Nejikovsky, “Autonomous Track Inspection Systems—Today and Tomorrow,” in *AREMA 2009 Annual Conference and Exposition*, 2009.
- [63] S. Saadat, C. Stuart, G. Carr, and J. Payne, “FRA Autonomous Track Geometry Measurement System Technology Development: Past, Present, and Future,” in *2014 Joint Rail Conference*, 2014, pp. V001T05A002–V001T05A002.
- [64] M. J. M. M. Steenbergen, *Wheel-rail interaction at short-wave irregularities*. TU Delft, Delft University of Technology, 2008.
- [65] P. Xu, Q. Sun, R. Liu, R. R. Souleyrette, and F. Wang, “Optimizing the alignment of inspection data from track geometry cars,” *Comput. Civ. Infrastruct. Eng.*, vol. 30, no. 1, pp. 19–35, 2015.
- [66] T. O’Connor, M. T. Andani, J. Muñoz, and M. Ahmadian, “Conversion of Non-Contact LIDAR Velocity Measurements to Spatial Markings and Indication Signals for Commercial Train Systems,” in *2015 Joint Rail Conference*, 2015, pp. V001T02A003–V001T02A003.
- [67] J. Muñoz, M. T. Andani, and M. Ahmadian, “Accuracy Analysis of Car Body-Mounted Doppler LIDAR Technology Used to Measure Track Speed and Curvature,” in *2015 Joint Rail Conference*, 2015, pp. V001T01A002–V001T01A002.
- [68] J. Munoz, “Application of Multifunctional Doppler LIDAR for Non-contact Track Speed, Distance, and Curvature Assessment,” Virginia Tech, 2016.
- [69] S. A. Wrobel, “Multi-function LIDAR Sensors for Non-contact Speed and Track Geometry Measurement in Rail Vehicles.” Virginia Tech, 2013.

Appendix A. Specifications of the Inertial Measurement Unit (IMU) used on the research car

The IMU that is used on the research car is an LN-200 made by Northup Grumman. Below are the basic details about this system. This unit is heavily regulated by the US Government since it is commonly employed in aircraft/military equipment.

SYSTEM DESIGNATION		LN-200	
	Units		
		-2	-1
Performance			
Heading Accuracy (AHRS)	Deg	2.4	0.8
Accel Channels			
Range	g	±40	
Bias Stability	ug	1500	300
Scale Factor Stability	ppm	1000	300
Gyro Channels			
Rate Input Maximum	deg/sec	>1000	
Bias Stability	deg/hr	3	1
Scale Factor Stability	ppm	100	100
Angle Random Walk (ARW)	deg/rt-hr	0.15	0.1
Physical Characteristics			
Volume	cu in	32	
Weight	lbs	1.7	
Power (typical)	Watts	12	
Input Voltage	V	+5/±15	

Figure A.1. Details of the IMU system used on the research car.

Appendix B. H/D Ratio for Rail Surface Assessment

LIR and RSF ratios were introduced and discussed in Chapter 8 as LIDAR-based measures to describe the rail surface material and condition. Another parameter that is believed to be useful for rail surface measurements is the ratio of the Doppler bandwidth to the Doppler signal intensity. This index is called H/D and is equal to the ratio of Doppler shift FWHM to the spectral intensity of the received LIDAR.

Laboratory-scaled tests are conducted to demonstrate the feasibility of the H/D aspect ratio application for the rail surface assessment. Track data are collected over the same track section that was used for RSF and LIR evaluations (Chapter 8) with similar testing protocol (Table 8-1).

Figure B-1 shows the H/D ratio, calculated over the bare segments (Test 1). The average H/D values for each section are also shown in the figure. Since the testing track segments are short and they may have some coating residues remaining on the rail from prior tests, the average H/D ratios are slightly different.

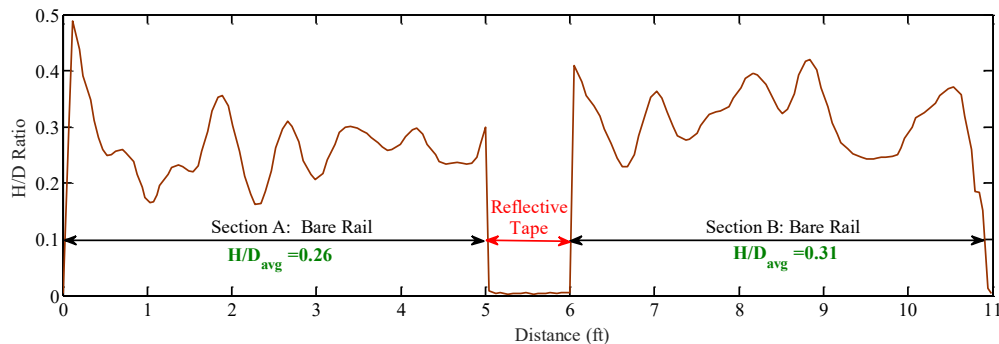


Figure B-1. Surface feature aspect ratio measurements for bare rail in Test 1. The average H/D ratios for Sections A and B are 0.26 and 0.31, respectively.

The H/D measurements for Test 2 (ToR friction modifier) are plotted in Figure B-2. The lubricated segment yields a lower H/D value, as compared with the dry section. A significant 76% reduction in average H/D ratio is observed for the coated segment, with respect to the dry H/D average value.

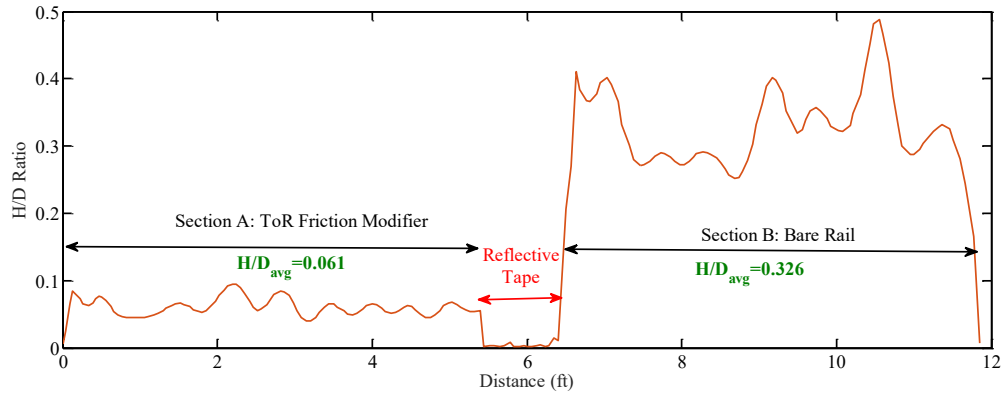


Figure B-2. Surface feature aspect ratio measurements for bare rail and rail with ToR friction modifier (Test 2). The average H/D ratios for Sections A and B are 0.061 and 0.326, respectively.

The H/D values are calculated and plotted in Figure B-3 for Test 3 (Section A with sawdust to simulate leaf residues). As the average values indicate, the H/D ratio is reduced by 79% over the coated segment.

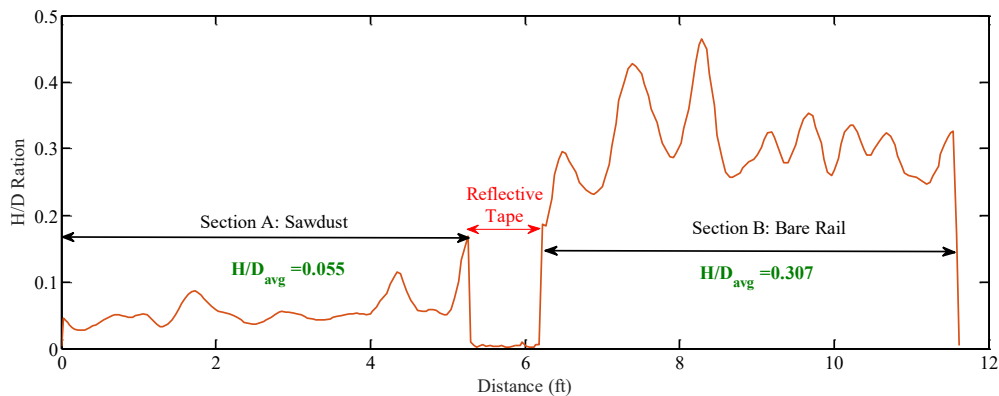


Figure B-3. Surface feature aspect ratio measurements for bare rail and rail with sawdust (Test 3).

Test 4 is performed to evaluate the H/D variation when the rail trolley moves over the rail when it is covered by 40-grit coarse sandpaper. Similar to previous tests, the results shown in Figure B-4 indicate that the coarse surface has a smaller average H/D ratio compared with the bare rail.

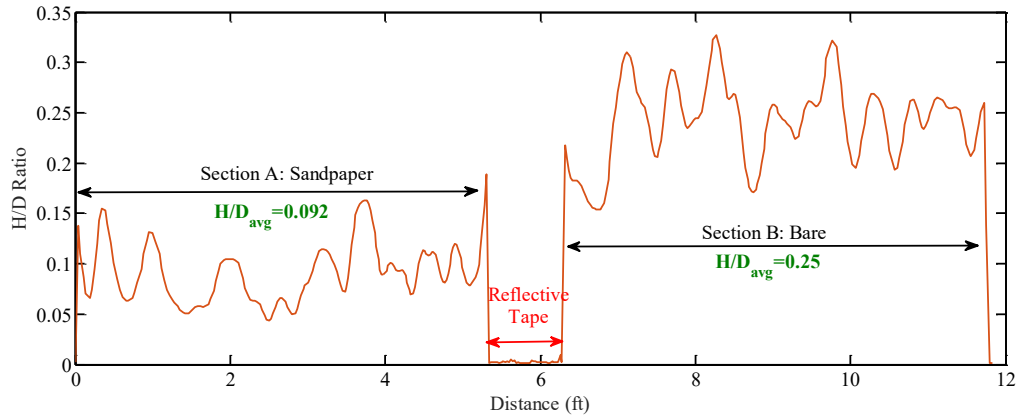


Figure B-4. Surface feature aspect ratio measurements for bare rail and rail covered by coarse sandpapers (Test 4).

Test 5 is a repetition of Test 4, and is intended to evaluate the repeatability of the rail surface assessment technique. Figure B-5 compares the H/D ratio measurements during Tests 4 and 5. The results indicate that the two test runs yield similar H/D ratios. As plotted in Figure B-6, the cart speeds during these two tests were different. H/D ratio measurements made for different rail surface conditions over Section A are compared in Figure B-7. Although local spontaneous variations are observed, different rail surface conditions yield various H/D measures.

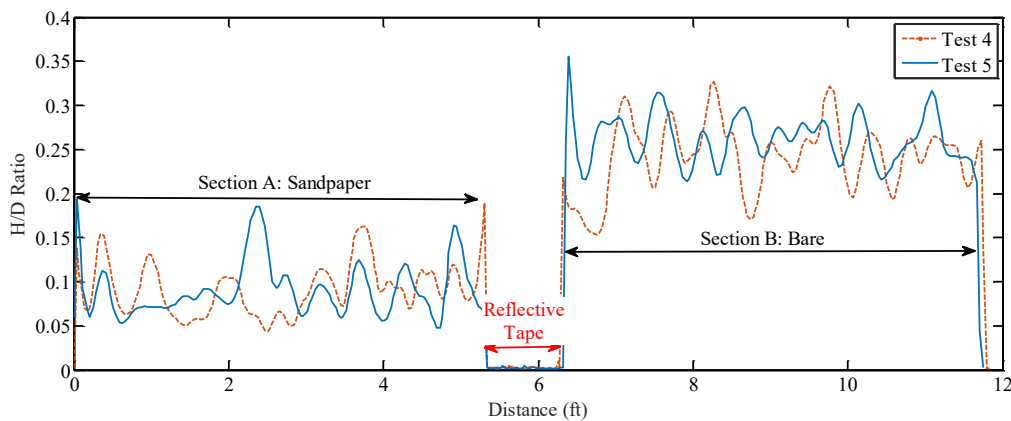


Figure B-5. Surface feature aspect ratio measurements are compared in order to assess the repeatability of the rail surface monitoring system measurements. (Tests 4 and 5).

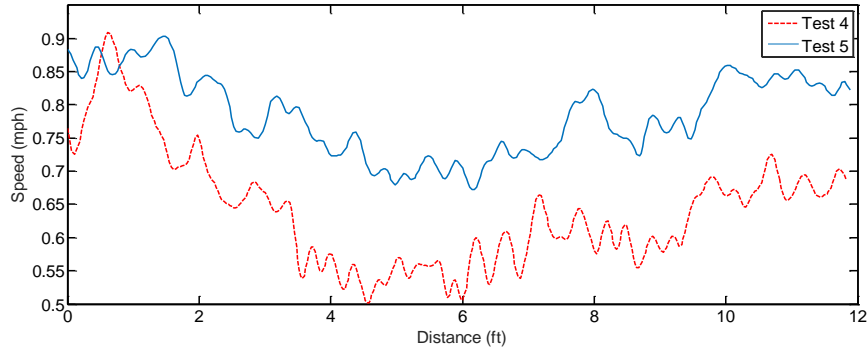


Figure B-6. Comparison of LIDAR speed measurements during Tests 4 and 5.

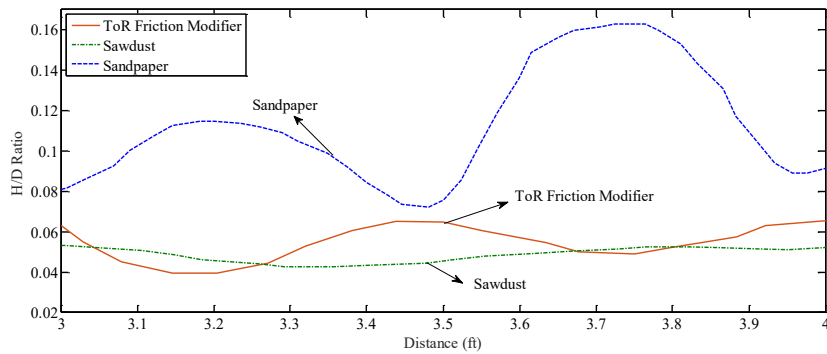


Figure B-7. Comparison of H/D measurements made for the tested coatings: friction modifier, sawdust, and sandpaper.

H/D computations for the tested rail surface conditions are summarized in Table B-1. In addition to the average H/D ratio for each surface, the ratio of the coated (wet) surface to the dry surface is also calculated and listed in the last column, represented by $\frac{(H/D)_w}{(H/D)_d}$.

Table B-1. A summary of the H/D calculations for various rail surface conditions.

Test #	Surface	(H/D)	$\frac{(H/D)_w}{(H/D)_d}$
1	Bare rail	0.26	1
2	ToR friction modifier	0.061	0.23
3	Sawdust	0.055	0.21
4	Coarse sandpaper	0.092	0.35